SLAC-PUB-1954
June 1977

HYBRID BUBBLE CHAMBER SYSTEMS[1]

J. Ballam & R. D. Watt

Stanford Linear Accelerator Center

Stanford University

Stanford, California 94305 USA

(To be published in Annual Reviews of Nuclear Science)

*Work supported by the Energy Research and Development Administration

CONTENTS

1 INTRODUCTION

After nearly two decades of spectacular success the bubble chamber (1), as a stand-alone detector of single events in high-energy particle collisions among hadrons, seems to be on the wane (2). Its place is being taken by sophisticated wire-spark-chamber arrays; by more complicated combinations of a bubble chamber and electronic detectors, usually called "hybrid chambers," or simply "hybrid systems;" and by the huge bubble chambers which are mainly used for neutrino physics at very high energies. Even these very large chambers are partially hybridized—that is, they have external associated electronic detectors which aid in the identification of certain particles which leave the chambers.

There are two main reasons for this change in emphasis: One is the need in strong-interaction physics for high statistics experiments, at least an order of magnitude greater than the heretofore largest bubble chamber exposures (100 events per microbarn of cross section). While these chambers could probably have produced the needed events, the required data analysis (the finding and measuring of the events) simply took too long. The early promises (2) concerning data-analysis capability failed by an order of magnitude (3) and, as a result, a collaboration of institutions, with a joint measuring capability of 2 million events/year, would have required more than ten years to complete the analysis of a 1000 event per microbarn experiment in a 2-meter hydrogen chamber (3) if they measured every event. Indeed, there are ways of cutting this down, such as selecting certain categories of events to measure, but even with such restrictions it would take three or four years of the entire collective resources of three very large institutions to do such an experiment, and during this period of time they would have completed only this one experiment.

The other reason is that the new very high energy accelerators (energy greater than 300 GeV) produce many events which have tracks that have momenta too high to be measurable in a bare bubble chamber. In such cases the measured kinematic quantities, supplied by the bare chamber, are confined to the spatial angles and the momenta of the slower particles. Some assistance has to be provided by external means in order to be able to analyze an event more completely.

In spite of these difficulties, the bare chamber retains qualities which will continue to make it indispensible for a large class of experiments provided the difficulties mentioned above can be overcome. Among these qualities are a very large detection efficiency; the ability to see very close to the origin of an event; almost 100% efficiency for observing the angular distributions of the charged products of an interaction; measurements of proper particle lifetimes between 10^{-11} and 10^{-7} seconds; the ability to determine, by means of ionization and momentum, the masses of particles moving slowly ($\beta \leq 0.8$) in the laboratory; and good efficiency for observing the decays of short-lived unstable particles, both neutral and charged.

The Hybrid System (HS) is the result of an attempt to retain as many as possible of these advantages of the bare chamber while at the same time extending its usefulness to experiments needing an order-of-magnitude increase in statistics, supplying a better method of particle identification, and providing better momentum measurements for the higher energy particles.

This has been accomplished, gradually over the past five years, first by the development of the rapid-cycling chamber which operates reliably at a rate from 20 to 100 times faster than was previously possible; and second by the use of wire chambers placed both upstream and downstream of the bubble chamber,

thus providing particle-by-particle measurement of the incoming beam momentum and angle as well as an accurate measurement of the momentum of the scattered particle. In addition, particle identifiers, such as large Cerenkov counters, can also be placed both in the beam and downstream of the chamber. The HS operate in either a triggered mode, in which the illuminating lights are flashed only when the downstream electronics has selected an event, or in an untriggered mode, in which every expansion is photographed and the downstream information is stored on tape for later use. Such systems are now in use in experiments at the Fermi National Accelerator Laboratory and the Stanford Linear Accelerator Center, and are also being constructed for use at the Rutherford Laboratory and at the new Super Proton Synchrotron at the European Center for Nuclear Research.

In this article we will describe some of the basic characteristics of these hybrid systems, and examine how they have been used in certain experiments in high energy physics.

2 AREAS OF PARTICLE PHYSICS ESPECIALLY SUITED TO HYBRID SYSTEMS

Since the HS can no longer claim to own all of the desirable characteristics of the bare chamber, it is important to delineate those areas of investigation that in some way are best matched to the system. At least one of the particles produced in an interaction in the liquid has to leave the chamber and be detected by the downstream counters. The structure of the bubble chamber usually imposes restrictions on the momenta and angles of these emerging particles. For example, most of the area of the bubble chamber walls is made of thick steel, composed of between 1/2 and 1 nuclear collision length and 5-10 radiation lengths. In addition, most chambers are surrounded by fairly thick-walled vacuum tanks and also, except for regions

up and downstream of the chamber, by steel magnets, thus making it virtually impossible to detect particles leaving the liquid at large angles with respect to the beam. In larger chambers, the best that can be done is to provide beam-exit windows in both the chamber and vacuum tank that are as large and as thin as can be made compatible with mechanical and safety requirements. These windows have been made as thin as 1/100 radiation length of aluminum (2.3 mm) with areas up to 70×15 cm, but most are made of stainless steel roughly 1.5 mm thick. The design of such beam windows is discussed in detail in Section 3.

An illustration of these geometrical restrictions is shown in Figure 1.

One should also design the downstream detectors so that they can accept the maximum number of particles leaving the beam-exit window.

Finally, especially in the case of rapid-cycling chambers, it is important to design a trigger that will keep the number of pictures to be scanned and measured to a level such that the experimental group(s) can finish this process within, say, a year of their original production.

Bearing these restrictions in mind, two general modes of operation are employed, depending on whether the HS is triggered or untriggered. In the triggered case, one generally focusses on a specific interaction for which there exists the following conditions:

(a) A calculable (and preferably large) acceptance.

(b) A yield which is statistically significant.

(c) A natural amenability to the design of a tight trigger so that the number of background pictures is not excessive.

(d) Some aspect of the interaction that uses the bare bubble chamber's natural advantages.

Several classes of interactions fall naturally into these categories. The first to be considered is the class of single, fast-forward, charged particle triggers in which the emerging particle takes up most of the momentum in the laboratory system and has a high probability of leaving through the beam-exit window. The momenta of the rest of the particles produced in the interaction are small and well-measured from the photographs themselves. Furthermore, these slow particles can be studied using all the advantages of the bare chamber. Some examples of this type of experiment are the following.

Nucleon Dissociation

In this process a nucleon is dissociated into a nucleon plus one or more pions, namely:

$$\begin{array}{l} a + N \rightarrow a + N^* \\ \qquad\qquad\quad \lfloor \rightarrow N + n\pi \quad (n \geq 1) \end{array} \qquad 1$$

where $a = \pi^{\pm}$, $K^{\pm}$ or $p\bar{p}$; N = p or n; and the emerging particle a carries a large fraction of the laboratory momentum in the forward direction. Such processes are very well suited to study by the HS. First, the N* system is backward in the overall center-of-mass system and is therefore moving slowly in the laboratory. The mass of the N* is well-measured in the bubble chamber, and its production and especially its decay angular distribution can be studied with very little experimental bias. Since the trigger is a single particle emerging in the forward direction, the acceptance of the system as a function of the four-momentum transfer (t) from the beam particle to the triggering particle is easily calculable, as is the acceptance as a function of the mass recoiling against the triggering particle.

These processes have a fairly sharp dependence on t, and therefore a t acceptance which cuts off at about $t = 1\text{-}2\ (\mathrm{GeV}/c)^2$ (a typical range for most

experimental arrangements); this eliminates a physical region in which the yield would, in any event, be very small. The momentum of the fast-triggering particle is measured in the downstream spectrometer with sufficient accuracy to allow the experimenter to determine whether or not any missing neutral mass consists of only one neutral or more than one neutral particle, and thus improves the mass resolution for the single neutral case to a level comparable to that achieved when no neutral particles were produced in the interaction.

The diffractive reactions have been the most studied because their cross sections remain reasonably large even at high energies, and the background due to exchange processes is small even at energies as low as 15 GeV. For example, the quartet

$$\pi^+ p \rightarrow \pi^+ N^{*+} \qquad 2a$$

$$\pi^- p \rightarrow \pi^- N^{*+} \qquad 2b$$

$$\pi^- n \rightarrow \pi^- N^{*o} \qquad 2c$$

$$\pi^+ n \rightarrow \pi^+ N^{*o} \qquad 2d$$

can be used to study the I-spin dependence of diffractive dissociation for N*'s produced in an energy-independent manner. The cross section for fast-emerging π's is about 5% of the total cross section, so that if one can eliminate elastic events in which the emerging particles are identical to the incoming ones, one can achieve good efficiency and a high ratio of useful to total number of pictures taken.

Exchange Processes

These are described by the general process $a+b \rightarrow c+d$, in which the fast-incoming particle a exchanges some intrinsic property with the target particle b so that the fast-emerging particle c differs from a in electric charge, or spin, or strangeness, or rest mass, etc. Again, the triggering particle should be a

single charged, fast-forward particle so that the trigger criteria described above can be adhered to.

These processes have a much steeper energy dependence than do the diffractive ones, going roughly as p^{-2}. However, the power of a HS allows one to observe processes whose cross sections are as small as 1 μb with good statistics. Thus it will be possible to pursue the study of these interactions to energies as high as 70 GeV, where backgrounds due to competing processes become quite small.

Exchange degenerate processes are good examples:

$$\begin{array}{l} \pi^+ p \rightarrow K^+ Y^* \\ \qquad\qquad \big\vert \longrightarrow Y^* \rightarrow \Lambda + n\pi \\ K^- p \rightarrow \pi^- Y^* \end{array} \qquad 3$$

Here the K^+ or π^- is fast and forward-going. Again, the acceptance is easily calculable as a function of t and recoil mass. The Y* is slow in the laboratory system, and its decay can be well-studied in the bubble chamber itself. The polarization of the Y* can be determined from the polarization of the Λ itself.

Another example is baryon exchange where the incoming particle is a meson and the outgoing one is a baryon, e.g.

$$\pi^{\pm} p \rightarrow p(n\pi) \qquad 4$$

where here the emerging fast particle is a proton.

There are many variations of the examples given here, including the case in which a fast meson is produced in the forward direction and decays into two charged particles, one of which is detected by the downstream chambers. Such a case is

$$\begin{array}{l} \pi p \rightarrow \phi n \\ \qquad\quad \big\vert \rightarrow K^+ K^- \end{array} \qquad 5$$

When one of the K's is detected, the chamber lights are flashed.

Fast-Forward Neutral Particles

Another class of events suitable for a triggered HS are those which have a forward-going neutral particle. Provided the downstream neutral detector is efficient and has good energy resolution, these events do not have to be characterized by a fast- or high-momentum trigger, since the neutral particles are unaffected by the magnetic field of the chamber. Examples of such reactions are:

$$\pi^{\pm}p \rightarrow \pi^{o}N^{*} \qquad N^{*} \rightarrow p + n\pi \qquad 6$$

Reaction 6 is an example of charge exchange. It is an important adjunct to reaction 1 because it sorts out the nondiffractive background. It does have a steeper energy dependence than 1 and therefore is accessible only up to the 50-100 GeV energy ranges.

A further example is

$$K^{\pm}p \rightarrow K^{o}_{L}p + n\pi \qquad 7$$

Since the K^{o}_{L} mean distance for decay is 1.55 meters, many of the forward K^{o}_{L}'s will leave the bubble chamber before decaying and can be made part of a neutral trigger. Similarly,

$$\pi^{\pm}p \rightarrow N + n\pi \qquad 8$$

where the fast-forward N is detected in optical or wire spark chambers, and its energy is measured in a calorimeter. Such experiments examine backward production of ordinary mesons and also search for exotic mesons (which decay into two like charges).

Inelastic Muon Scattering

Since muons have a small nucleon interaction cross section, it is possible to increase the incident beam flux by a factor of ten over what can be tolerated for

hadron beams. The inelastically scattered muons can be separated from the elastics simply by demanding that the scattering angle be essentially nonzero before flashing the chamber lights. The advantage of the HS here is that of observing in the bubble chamber the hadrons associated with the scattered muon.

Since the total cross section for inelastic muon interactions is only a few microbarns, it would be virtually impossible to use a bare bubble chamber to study this process.

Reactions With More Than One Forward-Going Particle

The class of interactions that is most difficult to deal with in an HS system is that in which the forward particle decays into several particles before leaving the chamber. An example is:

$$\begin{array}{l} \pi^{\pm}p \rightarrow Bp \\ \qquad \hookrightarrow B \rightarrow \omega\pi \\ \qquad\qquad \hookrightarrow \pi^{+}\pi^{-}\pi^{o} \end{array} \tag{9}$$

In reaction 9 the acceptance of the downstream system is poor because only a portion of the decay products is detected. Reaction 9 is therefore best studied in large-acceptance wire-chamber spectrometers. However, there are special cases in which the decay angular distribution of the forward meson is well-understood, and the object is to study a complicated N* or Y* state left behind in the bubble chamber. Examples of such reactions are:

$$\begin{array}{l} \pi^{\pm}p \rightarrow \rho N^{*} \\ \qquad\quad \hookrightarrow p + n\pi \\ \qquad \hookrightarrow \pi^{+}\pi^{-} \end{array} \tag{10}$$

$$\begin{array}{l} \pi^{\pm}p \rightarrow K^{*}Y^{*} \\ \qquad\quad \hookrightarrow \Lambda + n\pi \\ \qquad \hookrightarrow K + n\pi \end{array} \tag{11}$$

In both 10 and 11 the forward ρ and K* mesons have been well-studied. Therefore the effect of triggering on one of their decay products can be modeled, and the pseudo-two-body production process can be studied.

Interaction Triggers

This is a very general trigger which ensures that the interaction occurs in the useful volume of liquid in the chamber. The purpose is to eliminate reactions in the beam and vacuum windows, both upstream and downstream of the chamber, and to cut down on the number of photographs taken.

In the untriggered HS mode the focus is on interactions for which

(a) A number of the forward-going particles have momenta too high for measurement in the bare chamber.

(b) It may be important to know the mass of the forward-going particle.

(c) The cross section is fairly large ($\geq$ several hundred microbarns).

Untriggered HS are mainly used to improve the accuracy of momentum measurement and for particle identification. The most successful systems are those set up at the Fermi National Accelerator Laboratory, where the energy of beam particles reaches 400 GeV. The classes of experiments that have been done at FNAL so far are the following.

Elastic Processes

The HS is used to distinguish between elastic and inelastic scattering processes. Use of Cerenkov counters upstream of the chamber allows identification of the mass of particles in the beam, and therefore p, $\bar{p}$, K, and π initiated events can be differentiated in an unseparated beam. The reactions studied were:

$$\pi^- p \rightarrow \pi^- p \qquad 12a$$

$$\pi^- p \rightarrow \pi^- p + n\pi \qquad 12b$$

$$K^- p \rightarrow K^- p \qquad 13a$$

$$K^- p \rightarrow K^- p + n\pi \qquad 13b$$

Low Multiplicity Nucleon Diffraction and Double Diffraction at Very High Energies

Interactions similar to those of reactions of 2a and 2b have been studied for the case in which all the products are charged. In these cases the fast pion momentum is measured in the downstream system, and the momenta of the three remaining particles are measured in the bubble chamber. The slow proton is identified by ionization, and a four-constraint fit is made by balancing transverse momentum. Such experiments, as well as those which study the double diffraction reaction

$$\begin{array}{l} \pi^- p \rightarrow \rho N^* \\ \qquad\quad \big| \; \big\llcorner \rightarrow p\pi^+ \\ \qquad\quad \big\llcorner \rightarrow \pi^+ \pi^- \end{array} \qquad 14$$

have been studied with the FNAL 75-cm HS. In these cases the momenta of several forward-going particles are measured with the downstream system.

Inclusive Processes

These are dealt with in an HS because in order to cover the fullest range of kinematic variables used in the subsequent physics analysis it is necessary to measure the momenta of all particles of given electric charge. The variable most used is called rapidity, which is symbolized by y and defined by

$$y = \frac{1}{2} \ln \frac{E + p_b}{E - p_b} \qquad 15$$

where E is the energy of the particle, and p_b is its momentum along the beam axis.

Specific inclusive reactions which have been studied are:

$$\pi^- p \rightarrow \pi^{\mp} X$$
$$pp \rightarrow \pi^{\pm} X \qquad 16$$

Up to the present it has been assumed that all outgoing particles were pions (except those slow protons tagged by ionization as seen in the chamber). These experiments are quite suited to the HS because at very high energies, most fast particles leave the chamber through the beam-exit window and are seen in the downstream spark chambers. The ones remaining in the chamber are usually slow enough so that their momenta are directly measurable. Furthermore, since these results are mainly statistical and somewhat qualitative, a high degree of precision is not required. The incoming particle is again identified by the beam Cerenkov counters.

A further consequence of the increased acceptance at high energies is the ability to observe the inclusive interaction

$$\pi p \rightarrow \rho^o X \qquad 17$$
$$\rho^o \rightarrow \pi^+ \pi^-$$

again made possible by virtue of good downstream momentum measurements.

Muon Identification in Neutrino Experiments

A very successful use has been made of the HS in identifying muons emerging from neutrino interactions in the liquid of the very large volume chamber installed at FNAL. Since the muons penetrate the thick chamber and vacuum walls without interacting, they can be detected via wire chambers placed external to the bubble chamber.

Reactions of the type

$$\nu p \rightarrow \mu X$$
$$\nu p \rightarrow \mu\mu X \qquad 18$$

can be studied in various chamber materials (hydrogen, neon-hydrogen mixtures and eventually deuterium).

Future extensions of triggered experiments, which will depend upon developments in fast on-line data processing, include multiparticle, neutral kaon, and missing mass triggers; whereas extensions of untriggered experiments depend on more sophisticated particle identification, especially the ability to distinguish among the masses of multiple forward-going fast particles.

3 CONSTRUCTING AND OPERATING FAST-CYCLING CHAMBERS

Because of the unique nature of its accelerator, SLAC has been a leader in the development of fast-cycling chambers. The accelerator can pulse as often as 360 times a second, and this makes the constructure of rapid-cycling chambers a very desirable endeavor. In this chapter we will discuss the SLAC chambers (4, 5) and also those in operation and being considered for construction at other laboratories.

Definition of a Rapid-Cycling Bubble Chamber (RCBC)

We have chosen to limit our discussion to those chambers which pulse 10 times per second or more steady state, and those which can pulse 10 or more times during the beam-spill period of proton synchrotrons. Within the group so defined are the SLAC 38-cm chamber, the SLAC 1-meter chamber, the Rutherford Rapid-Cycling Vertex Detector (C. Fisher & R. Newport, private communication), and the proposed CERN 1-meter chamber (6).

Basic Requirements to be Met in the Design of an RCBC

SPACIAL RESOLUTION WITHIN THE CHAMBER The prime purpose of an HS is the accurate location of the vertex in an event and the detection of all of the charged and short-lived neutral particles produced. It is very important that the liquid motion within the chamber be small so that minimum track displacement

occurs between the time of beam injection and the flash of the camera lights. The best way to minimize liquid motion during expansion is to use the largest possible piston to produce a plane pressure wave in the liquid. The 1-meter chamber at SLAC is a good example of this principle because it has a piston that needs to move only 4.6 mm to expand a chamber which is about 43 cm deep.

BUBBLE SIZE AND DENSITY ALONG A TRACK In the bright-field illuminated chambers, especially those using Scotchlite (7,8), we have found that tracks having a mean bubble diameter of around 450 microns in chamber space and an average of 10 to 12 bubbles per centimeter are preferred by most experimenters. The bubble count per centimeter can be controlled by both the liquid temperature and pressure at the time of beam injection, but the size of the bubbles, although dependent on liquid temperature, is more easily controlled by the time delay between the beam injection and light flash. It is perhaps fortunate that not only does a delay of 2.5 to 3 ms give the bubbles time to grow to the proper diameter, but it also gives the computer time to make the necessary calculations to decide whether or not to flash the lights.

SIGNAL-TO-NOISE RATIO OF TRACKS ON FILM The film may be scanned by automatic scanning machines which are very limited in their ability to adapt to changes in signal-to-noise ratio, and this puts stringent requirements on the uniformity of illumination and the bubble diameter. Figure 2 shows a densitometer scan of typical SLAC 1-meter RCBC tracks. It is possible under good conditions to maintain tracks of this quality for days at a time. In order to do this, the temperature must be maintained very accurately, and the expansion system must repeat its operation very precisely for millions of times. Both of these systems will be described in detail later.

RELIABILITY AND REPRODUCIBILITY OF THE CHAMBER Perhaps the greatest difference between a large slow chamber and an RCBC is the difference in the reliability requirements of parts. As an illustration, the 72-inch chamber at Lawrence Radiation Laboratory (9) (LRL) pulsed around 15,000 times a day, and it destroyed its expansion valve about every 60,000 pulses. In contrast, the SLAC 1-meter RCBC pulses as often as 900,000 times a day, and it destroys its expansion valve about every 10 million pulses. A great deal of effort has gone into developing that increase in reliability.

HEAT LOADS It is very important that a fast-cycling chamber be made so that the heat load into the liquid is as small as possible. A sliding piston with rings not only leaks liquid from the chamber to the region behind the piston, thereby reducing expansion efficiency, but it also produces a large amount of heat as a result of sliding friction. Eckman (10) introduced the use of a single convolution bellows on the LRL 25-inch chamber, and most fast chambers now have such a bellows in one form or another. It is interesting to note that although one can get much more flexibility with multiconvolution bellows, it is possible that most of the motion is provided in the first convolution, and this of course would soon cause its failure.

An additional source of heat into the liquid results from eddy-current heating in the piston as it moves through a nonuniform magnetic field. Eddy-current heating is proportional to $N(VB_x)^2$ where B_x is the gradient of the magnetic field in the direction of the piston motion, V is the velocity of the piston during the stroke, and N is the number of pulses per second. Both N and V are determined by the design pulse rate and chamber depth. The field gradient can be reduced by shaping the iron pole pieces to a certain extent, but this is far from a satisfactory solution. The only other alternatives are the use of a piston made of

nonconducting material, plastic or glass, as the Rutherford Laboratory group has done with the RCVD, or the incorporation of cooling loops within the piston in a manner similar to that used with the SLAC 1-meter piston.

EXTRANEOUS BUBBLES When pulsing at rates in excess of 10 pps, it is very important that bubbling from trapped volumes, leaking valves (4), glass-to-metal seals and hot spots be kept as small as possible. The success of any fast-cycling chamber will be determined by how well these problems are solved.

It is possible to inject as many as 100 charged particles into the chamber and form bubbles whose volume will total 1.5 cc at the time when they are largest. If the chamber is operating well, this volume of gas will present no problem to either the expansion system or the refrigeration system. However, if extraneous bubbles from a poorly designed chamber collect in the top, it is easy to have 50 to 100 cc of gas continuously present, and this quite seriously affects both the piston stroke and the refrigeration requirements. The stroke, as calculated from the liquid bulk modules, should be much less than 1%. However, few small chambers are so free of local gas pockets and bubbles distributed throughout the liquid that they achieve sensitivity with a change in volume of less than 3/4 of a percent during the stroke.

Description of Some RCBC's

THE SLAC 1-METER RCBC This chamber (5) was first operated in 1967 and has been gradually improved from its design pulse rate of 1 per second to its present 10-12 pulses per second. Since its origin it has expanded a total of 224 million pulses and has taken 10.5 million pictures. The principal features of the chamber are described in Table 1, and Figure 3 shows an elevation view of the chamber. A detailed description of the various systems follows.

Illumination The piston of this chamber is covered with high quality Scotchlite (8) made by the 3M Company. Great care was taken in the selection of the glass beads so that they would be very uniform in diameter (about 30 μ) and thus all have about the same retrodirective characteristics. In addition, they have been spread on their support matrix so that their density is quite uniform. The Scotchlite comes in 30-cm wide strips, and since the chamber piston is 102 cm in diameter, it requires four sections of Scotchlite to cover the surface. It is not feasible to have the Scotchlite overlap at the seams in an effort to provide continuous coverage, because this would cause bubbling from the volume trapped under the overlap. A compromise is made wherein the seams are left as narrow as possible without overlap, and the sections put on so that the seams are at right angles to the path of the beam as it traverses the chamber. This is shown in Figure 4.

Scotchlite is a composite made of beads held in an adhesive matrix and covered by a thin layer of mylar for protection. The mylar is a very good insulator, and this attribute has, on occasion, been a source of trouble. During the piston motion, there is a small movement in the liquid hydrogen, and this motion causes an electrostatic charge to build up on the surface of the mylar. If the chamber is not extremely clean and free of dust, lint and other such debris, these contaminants will eventually end up deposited on the surface of the Scotchlite. The deposited material tends to clump together and eventually becomes large enough to be a source of small bubbles. The bubbles not only contribute to the dynamic heat load imbalance but also impair the retrodirectivity of the Scotchlite, causing a loss in picture quality. Very careful installation of the Scotchlite allows up to 50 million pulses of operation and several cooldown cycles before replacement is necessary.

Bellows The stainless-steel omega-shaped bellows which allows the piston to move is an extremely critical part of a fast-cycling bubble chamber. The cross-sectional view shown in Figure 5 shows the method of construction used at SLAC. The bellows is essentially a tube bent into a circle of over 1 meter in diameter, after which a segment of the inner portion is cut out. The inner edges of the circular tube are then welded to 2 flanges which are then in turn welded, one to the piston and the other to the chamber body.

In the bellows design it is important to keep the bellows quite stiff so that there will be little tendency to excite oscillations in the mass of the bellows which may be harmonically related to the motion of the piston. During the early stages of the SLAC 1-meter chamber development, a hydroformed bellows was installed whose cross section is shown in Figure 6. When the chamber was pulsed, this bellows failed very quickly (less than three million pulses) at the point where the metal rolls over the rounded nose of the flange. Tests ultimately proved that the "flopping mode," in which the whole mass of the bellows moves up and down, had a period quite close to that of the chamber pulse period, and this caused the bellows center to overshoot when the moving flange returned to the reset position as the chamber stroke was completed. If heavy liquids such as neon are used in a chamber, particular attention should be paid to these resonances, because the internal liquid mass can greatly affect the bellows' natural frequency. Even though the bellows contributes no significant heat to the liquid, it is necessary to have a cooling loop in the top internal section to condense any gas bubbles that may be formed and trapped there.

With proper attention to these problems, bellows can be made to last indefinitely. The 1-meter chamber has 200,000,000 pulses on its present bellows.

Pluming In order to keep the expansion stroke as small as possible, it is important that the chamber be completely full of liquid—no large gas bubbles trapped anywhere. This must be true both before the start of expansion and during the pressure drop caused by the piston motion. Any small pre-expansion bubbles can be taken care of by proper cooling of the periphery of the chamber, especially the top region. The bubbles that grew during the pressure drop and which are a result of hot spots, small cavities or rough surface regions with sharp points, are a continuing problem in fast chambers and must be kept to an absolute minimum.

It is probably safe to say that the major source of extraneous bubbles in SLAC's chambers is the seal between the chamber glass and the chamber body. During the evolution of the fast-cycling program at SLAC, it was necessary to develop a new type of seal before the 1-meter RCBC could exceed 6 pulses per second. Figure 7 shows the construction of this seal. It is made of pure indium that has been pooled over the indium-wetted surface of the stainless-steel rings that make up the inflatable gasket. After the indium has cooled, it is machined to a wedge shape that crushes into intimate contact with the glass when helium under pressure is introduced into the inflatable gasket.

The traditional glass-to-chamber seal (5) previously used was similar to that shown in Figure 8. The indium was pressed into round grooves and then later flattened when helium was introduced into the inflatable bellows region under pressure. This method of installation allowed small gas pockets to be trapped, both in the groove and under the indium, as it flattened down on the steel surface. When the chamber was later filled, many of these gas pockets were continuous from the bottom of the round grooves out to the chamber liquid and thus caused pluming during the pulse. The new wedge gasket cannot have

gas pockets between the indium and the steel, and is unlikely to have them between the glass and the indium.

Chamber refrigeration When pulsing at high repetition rates, one finds that the time constants involved in changing the temperature of a local region by external means are very long compared to the time between two pulses. On the other hand, if a warm region develops within the chamber, it will probably cause a thermal runaway within four or five pulses. Since it is thus not possible to detect a thermal problem and correct it rapidly enough, great emphasis must be placed on preventing thermal instabilities from occurring at all.

One source of thermal instability is the development of gas pockets within the chamber at the top of the bellows and the chamber body. If the accumulation of gas is slow, it is possible to condense the bubbles and not cause any great perturbation in the local region. If it is fast and the refrigeration system is given the information to cool rapidly, then a situation can occur in which the chamber over-pressure is reduced to the point where it is too low to compress bubbles in the main body of the liquid, and a loss of control happens very quickly. If in the normal course of operation a heat exchanger is allowed to shut down for a period of several minutes because of lack of refrigeration demand for that loop, the pipes that supply the loop will warm up by radiation loss, etc. When next the loop is required to conduct liquid, the very first gas that comes through will be hot and the heat exchanger will have a hot spot in it which in turn heats the chamber liquid, causing a bubble and subsequent loss of control.

We have found that heat exchangers should be operated with some flow at all times, and the temperature of the liquid in the heat exchanger should be kept only very slightly below that of the chamber liquid. This small temperature difference between refrigerant and chamber liquid means that the heat exchanger

area needs to be large. The ideal situation would be one where the whole chamber body, especially the top, was a part of the heat-exchange system. One method is to suspend the chamber totally in a bath of liquid. The SLAC 1-meter chamber approximates total immersion by having an internal upper heat exchanger welded to the chamber wall. In addition, the whole chamber casting is refrigerated externally, and the piston is hollow and contains refrigeration loops.

One additional benefit that accrues from the small temperature difference between the refrigerant and the chamber liquid is the relative absence of small volumes of cold chamber liquid near the heat exchangers. If present, these cold or hot volumes of liquid would cause "optical turbulence" because of the difference in the index of refraction between the main body of the liquid and the local perturbation. This results in some cases as apparent short-range deflections of the tracks.

Expansion system Figure 9 is a schematic representation of the drive system used in the SLAC 1-meter chamber. Examining this figure from left to right, one finds the chamber hydrogen, which can be treated as a massless spring. (When neon is the liquid, it is better treated as a distributed-mass spring.) Next is the chamber piston, whose weight is about 1200 lbs, followed by the rod which extends from the chamber out through the vacuum tank to the 25.4-cm oil-drive piston. The drive rod, of course, is also treated as a spring since it compresses about 0.5 mm under the chamber pressure load. The oil system follows, with an expansion valve which releases the oil into the bouncer or energy-storage region that consists of an aluminum piston backed up against a gas volume. When the piston system has moved to the right (decompressed direction) as far as the bouncer gas will allow it to move, most of the potential energy that had

been stored in the chamber liquid is now transferred to the gas in bouncer. At this time the direction reverses and the piston system moves to the left (compressed direction) and "almost" travels back to its original starting point. However, it has lost some energy in sliding friction, oil friction, etc., and it resets about 80% of the way without help. At the proper time the recompression valve is opened and a small burst of oil is added to make up for the losses. Figure 10 shows a typical trace of the motion of the warm end of the drive rod; the cold-end motion is inferred from the pressure change during the cycle. The phase lag between the ends can be seen, as well as the natural frequency of the drive-rod spring-mass system.

Beam window design The beam entrance window must be kept as thin as possible to minimize beam interactions within its material. On the other hand, it must be strong enough to withstand many millions of pulses without failure. From the standpoint of low mass and reasonable strength, aluminum is a good material to use. If, however, the main chamber body is made of stainless steel, then the aluminum window must be bolted in place with a gasket to provide the seal. For slow chambers this is a satisfactory solution, but RCBC's will not tolerate the additional pluming that such a seal would introduce, and one is forced to look for other solutions. Figure 11 illustrates the methods used at SLAC on the 1-meter chamber. A section of stainless steel (2.5-cm thick) is milled so that it has a cutout of the same height and width as the beam window requires. The heavy portion (window frame) surrounding the thin portion will ultimately be welded into the chamber body in such a way as to produce a smooth "plume free" weld.

The flat milled piece is then bent into a cylinder whose radius is the same as the chamber radius. After it is properly bent it is then placed in a hydroform

jig, and the thin section is forced to assume the shape illustrated. Since the window is then welded into the chamber, particular attention must be paid to the transition from the thick window frame portion to the thin window section. Since the thin section moves radially in response to the pressure change during the pulse, any discontinuities will soon cause a crack and subsequent failure of the window. Therefore the milling cutters should not introduce any scratches or grooves that might cause high local stresses. If the window has been made with stainless steel, such a failure would give adequate warning because stainless is quite ductile, and the surrounding vacuum would thus deteriorate slowly over many pulses.

THE SLAC 38-cm RCBC This chamber (4, 11), finished in 1973, was the first electromagnetically driven bubble chamber. It receives its expansion force from a very large coil wrapped on a fiberglass form and suspended in a dc magnetic field, much like a large audio speaker voice coil.

The chamber has achieved a pulse rate of 40 times a second while taking pictures of acceptable quality. It has been pulsed a total of 90 million times and has taken over one million pictures. The principal features of the chamber are listed in Table 2, and the chamber itself is shown in Figure 12.

The bellows in this chamber perform three major functions. Figure 13 shows a cross-sectional view of the bellows, which is seen to differ from the usual omega-shaped bellows in the extended central section. This was done so the beam particles could enter and exit through a section of thin material. In effect it provides a beam window with a full 360-degree coverage. The whole chamber is immersed in a liquid hydrogen bath, and the thin bellows provides a large area for heat exchange between the chamber and the surrounding liquid. However, the major part of the refrigeration is done through the top plate of the

chamber. The piston motion, about 1.27 mm, is made possible by the curved upper and lower sections of the bellows.

Perhaps the most unusual feature of this chamber is the method by which the drive force is obtained. Figure 14 shows the spring-mass system involved and the drive coil through which the pulsed current travels. The radial dc magnetic field through which the pulsed coil moves is about 14 kG, and the pulsed current is 400 to 600 A. Figure 15 shows the control circuits for the pulsed current. SRC's 1 and 2 discharge the energy stored in the capacitor through the moving coil. The electrical time constants are designed so that the coil current has gone through its peak and returned to zero at about the same time the piston reaches the most expanded part of its motion (see Figure 16). The charge on the energy storage capacitor is now of the opposite sign and about 75% of the original value. When the piston starts to move back down in the direction of recompression, SRC's 3 and 4 are fired and cause a braking force to reduce the large piston overshoot that would otherwise occur. Proper phasing of the various SRC's can produce a pulse shape very close to the optimum, which would be expressed by $X = A(1 - \cos \omega t)$.

The problem of spurious bubbling or pluming from the glass-to-chamber seal was handled in the same manner as that for the SLAC 1-meter chamber. However, one of the major obstacles to fast pulsing in this chamber was pluming from the fill valve between the chamber liquid and the reservoir outside the chamber. This problem was solved through the use of the special valve shown in Figure 17. An important feature of this valve is the conical seat, slightly flexible, which is pressed on by the tapered center prod. A force of about 40 pounds on the prod will make a seal which is tight when tested by a mass spectrograph and which tolerates many operations without developing an appreciable leak-through rate.

THE RUTHERFORD RCVD This chamber (12) first ran in July 1976 and promises to be a very useful device. It achieved good sensitivity at pulse rates as high as 20 per second, and it is planned to operate at 60 pps. Figure 18 shows the chamber in cross section. The chamber body is aluminum and the sidewalls are very thin so that the beam, which makes its entrance there, will cause few interactions in the walls. The cooling is done from the top by a pool of hydrogen liquid whose pressure and temperature are controlled by a condensing coil through which runs liquid hydrogen from the refrigerator. The chamber is filled through an aluminum valve in the top, of a design similar to that shown in Figure 17.

The expansion system is electromagnetic, and the force is derived from a large coil moving in a fixed magnetic field. The drive coil is at the bottom at room temperature and is separated from the cold chamber by an evacuated distance piece made of epoxy glass. The glass moves with respect to the chamber body and is sealed with adhesive to an annular ring which connects to the expansion bellows. In the final version this chamber will be operated in an extremely high magnetic field which would cause large-eddy current heating in moving metal parts. To avoid this heat load, the Rutherford group developed a unique bellows made of epoxy fiberglass and molded over a form of the proper shape. As can be seen in Figure 18, the bellows does not close upon itself in the same way an omega bellows does, and this, of course, simplifies the construction process. It also precludes the trapping of bubbles within the bellows, a problem inherent in the omega form. A second bellows is used at the bottom of the distance piece to allow its free motion.

The optics system outside the chamber consists of a large diagonal mirror to direct the light to the cameras through a hole in the side of the distance piece.

The inner upper part of the chamber body is polished and acts as a mirror to return the light from the light source.

The pulse mode, designed to make use of accelerator flat-top operation, will be one with bursts of about 20 pulses followed by a period of quiet. This mode has the advantage of allowing extraneous bubbles that are formed during the burst to condense in the next off period.

THE CERN RCBC At the present time the CERN RCBC proposal is the only known chamber of its size which is designed to pulse 30-40 times a second. The possibility of accomplishing such a high pulse rate is enhanced by the mode of operation that will be used. Rather than a steady rate of 30 pps, it will be on for only 2 seconds and off for 6 seconds. The dead period will allow any residual bubbles to be condensed before the next pulse burst arrives.

Although at this time the final design of the chamber and its expansion system is not complete, it is very likely that the usual CERN mechanism for expansion will be employed. A hydraulic drive system using a proportional-flow-control valve will force the chamber piston to conform to a prescribed displacement curve. The system frequency response will be high enough to do some pulse shaping within the pulse as it is demanded by the feedback control system. A system such as this is versatile and will allow them to shape their pulse as they wish. A large overshoot in pressure in combination with low operating temperature (see bubble-growth description in Section 6) will be needed to achieve the pulse rate they need. Table 3 gives the important specifications for this chamber.

4 DESCRIPTION OF HYBRID SYSTEMS

General

As an introduction to a relatively sophisticated triggered HS we consider the one associated with the SLAC one-meter chamber. This is shown in Figure 19. It consists of four main parts: the beam position, momentum and mass measuring system, the bubble chamber, the outgoing particle measuring system, and the fast trigger. In addition, not shown in Figure 19, there is the on-line data-logging system. The fast trigger consists of a coincidence between the beam counter (S_1) and one of the hodoscope counters (H), together with a pulse $\leq$ a small value in Cerenkov counter C. If this coincidence occurs, all of the information gathered by the beam multiwire proportional chambers (MWPC), the beam Cerenkovs (C_B), the downstream MWPC's and the large Cerenkov counter (C) is dumped into the buffer. Since MWPC's are used, all of the above occurs within about 100 nanoseconds. The system then has up to 3 milliseconds (the time it takes the bubbles in the chamber to grow large enough to be photographed) to determine whether or not to flash the chamber lights and take a photograph.

This time to sort out unwanted events is extremely important in establishing a "tight" trigger, is unique to the triggered HS, and is one of the main reasons for its success. Without it the number of photographs taken would be prohibitively large. The first plane of upstream MWPC's determine the deflection of the beam particle due a bending magnet (not shown) and thus its momentum, and the two beam MWPC's define the entry angle of the beam particle into the bubble chamber. The beam Cerenkov, used in a threshold mode, defines the mass of the beam particles. Several beam Cerenkovs in series may also be used. The three planes of downstream MWPC's are placed in the magnetic field common to the bubble chamber and determine the momenta of the outgoing tracks. Each of

the planes, α,β,γ, consists of three sections in x, y and u. All have 2-mm wire spacing, with u placed at 30^{o} with respect to y.

If one of the outgoing tracks goes through C, its mass can be determined by pulse height or by the absence of a signal, and the hodoscope can be used later to make a proper match up with a signal from one of the mirrors of C. In a typical experiment, such as $\pi^{+}p \rightarrow K^{\pm}X$, it was desired that the lights be triggered by a K^{+} of momentum greater than some p_{min}. The pressure in C was set so that at p_{beam} the K pulse was one-half that of a π meson of momentum p_{beam}. After a fast trigger, $S_1 C_b H \bar{C}$, an algorithm using the information from the rest of the system was used to calculate the momentum and angle of the outgoing track(s). Then a check was made to see if the pulse from C corresponded to that for a K particle having the measured momentum, and also to see if the hodoscope counter corresponded to a particle having gone through the correct mirror in C. (The algorithm will be described in more detail in a later section.) Thus, if the entering particle were truly a beam particle, if the interaction took place inside the fiducial volume of the bubble chamber (and not in external windows or other material), and if one of the outgoing particles was a K meson of the desired momentum, then the lights were flashed. The design goal of the system was to achieve an overall on-line efficiency of $\geq 50\%$.

In the untriggered case the emphasis is on storing highly accurate information which is to be used later in off-line analysis. Figure 20 shows a typical setup designed for use with the FNAL 78-cm HS (13). The spectrometer is composed of MWPC's at locations H-G and, as in the previous case, makes use of the bubble chamber magnetic field. The upstream portion utilizes MWPC's

with 2-mm wire spacing. The wire chamber at each of the detector locations is again made up of three sections, each of which is rotated 120^{o} with respect to its neighbor. Planes D, F, and G have a fourth section for greater momentum precision. The upstream system includes a Cerenkov counter (14), and the downstream system includes a muon counter (not shown in the figure), followed by scintillators and a shower detector made up of plane H, immediately preceded by 1.27 mm of lead.

The system is triggered by a coincidence between scintillator counters SCI and II, and all other signals are strobed into memory. Since MWPC's are used, the time to strobe the data was less than 125 nsec, and therefore each beam particle entering the chamber during its sensitive time could be individually tagged and associated in time and space with tracks in the bubble chamber. This system did not have particle identification for outgoing tracks, so that its main function was to tag the beam and provide an accurate momentum measurement for the outgoing tracks. Particle tagging will be introduced in the near future (see Section 6).

Upstream Counters and Wire Chambers

These are usually quite conventional in composition. The object is to define the mass, angle of entry into the bubble chamber, and momentum of the beam particles: the emphasis is therefore on a high degree of spatial accuracy. This is usually achieved with MWPC's such as those shown in Figures 19 and 20, placed in such a way as to have a long lever arm between the first MWPC and the momentum-defining bending magnet. In general 2-mm wire spacing gives sufficient spatial resolution to provide fractional percent momentum resolution for beams whose momenta is as high as several hundred GeV/c. The beam angles are determined by two sets of MWPC's with no magnetic field between

them. Beam Cerenkov counters are usually employed for mass determination. Since the beams enter these counters at a zero-degree or very small angle with respect to the mirror axis, they are highly efficient, and it is thus possible to know the mass composition also to the level of a fraction of a percent (as will be discussed in Section 5).

Counters Located in Vacuum Tank

There are special circumstances in which counters placed near the outside wall of the bubble chamber, and inside its vacuum tank, can be used to mark the occurrence of an interaction with a large acceptance relative to that available to a system such as shown in Figure 1. These have usually been scintillators, with light pipes coming through the outside wall of the vacuum and out to a region of small magnetic field. Such a system can also be used to mark the time-of-flight of a neutral beam. The chamber lights can be triggered on a rough time measurement, and a more exact determination can be made later by measuring the actual path length of the track in the bubble chamber that produced the pulse in the scintillator. Such a system of scintillators installed in the SLAC one-meter chamber has been used in a $K^{o}p$ experiment (15). Because of the wall thickness of the bubble chambers, these counters cannot be used to get information on the precise location of a track after it leaves the illuminated volume.

An exception to this rule is that of the SLAC 38-cm fast-cycling chamber, which was constructed so that the expansion bellows also served as the cylindrical side wall and was only 1.2 mm thick. Proportional wire chambers (16) were placed in the vacuum space, both upstream and downstream. The beam used was mainly K_L^o mesons, and the upstream chambers were used as an anticoincidence, while the downstream wire chambers were used as part of a positive

coincidence circuit which triggered the bubble chamber lights when two or more forward charged particles left the bubble chamber.

The Downstream System

The most complicated part of the HS is the array of counters and spark chambers downstream of the bubble chamber. These must provide information on the momenta, angles and masses of outgoing particles, as well as multiplicity and, on occasion, veto capability, either on- or off-line. For charged particles there are two classes of systems, depending on whether the analyzing magnet is the fringe field of the bubble chamber or a separate magnet forming part of a downstream spectrometer. The former case is cheaper but more importantly has a much greater acceptance, which is the reason that most HS use this method. The separate magnet has inherently a greater momentum accuracy, which it achieves at the expense of acceptance. However, this measurement of momentum can be done independently of any knowledge of the vertex point of the interaction and is especially useful if an accurate measurement of the mass recoiling against the outgoing particle is desired. An example of such a system is shown in Figure 21, in which the momentum of the outgoing particle was known to a fraction of a percent.

This system was used to trigger on a missing mass greater than the mass of a proton, and it eliminated some 75% of the elastic pion-proton scatterings which otherwise would have swamped the experiment. This spectrometer, when used in off-line analysis of events with very high energy forward-going charged particles, is almost indispensible to the analysis of one-constraint (1C) events, namely, in separating events with one neutral particle from those in which there are more than one.

Another form of downstream trigger is that for neutral particles. An example (17) is shown in Figure 22. The trigger system consisted of an array of 19 wide-gap optical spark chambers, preceded by lead plates and an anti-coincidence counter S, and followed by a calorimeter consisting of 15 Fe/scintillator sandwiches. The bubble chamber lights (and the optical spark chambers as well) were triggered whenever there was no pulse in S_1 (neutral particle and not a gamma ray) followed by a pulse height from the calorimeter corresponding to an energy deposited equal to or greater than half the energy of the incident π^- particle. A similar technique has been used with the SLAC fast-cycling 38-cm chamber (18) and with the 78-cm chamber located at the Argonne National Laboratory and designed by a group from the University of Wisconsin (19).

Another elaborate downstream spectrometer has been used with the SLAC 38-cm fast-cycling chamber in the scheme shown in Figure 23. The spectrometer (20) information was fed into a computer whenever the T scintillation counter banks recorded two or more fast particles, the E counters did not fire (no slow accidental), and the A counters indicated that one or more particles had left the magnet. A picture was taken at the same time if two or more wires in the bubble chamber PWC's fired. Off-line the spectrometer calculated the mass of the pair in events in which two charged particles went through the spectrometer and determined if this was a K_S^o mass. This was correlated with the bubble chamber frame number, and that particular picture was subsequently scanned to see if the decay point of the K_S^o was inside the chamber's fiducial volume. The chamber was then used to see if another particle (usually a slow proton) was associated with the interaction that produced the K_S^o.

Another downstream system which was used in an untriggered mode with the FNAL 78-cm chamber (21) is shown in Figure 24. The main elements are the four dual, wide-gap, optical spark chambers 1, 2, 3 and 4. The gaps are 20 cm long, the active transverse dimension are 76×180 cm, and the two chambers are separated by 1 m. The spark chamber cameras could be pulsed 5 times per second. The spark chambers were triggered if an incoming beam track either produced two or more forward minimum-ionizing secondary tracks as detected in a set of three dE/dx counters, or was deflected from a normal beam trajectory as detected by two sets of aligned counters. The dE/dx counters have high efficiency for high multiplicity events, and the deflection counters are best for low multiplicity events. Here again, the bubble chamber magnet is used for momentum analysis of outgoing particles.

A downstream trigger for muons using the SLAC one-meter HS is shown in Figure 25. Muons with a scattering angle roughly between 1^{o} and 6^{o}, having an energy greater than 1.4 GeV, and penetrating one meter of steel caused a coincidence between the scintillator trigger-counter hodoscopes which provided a fast trigger for the spark chambers. The information from the hodoscope was then fed into a computer, which first checked that the hodoscope hit pattern could have been caused by a track coming from the bubble chamber fiducial volume, and if so, caused the bubble chamber lights to flash. The wire chamber information was used off-line to improve the momentum measurement of the scattered muon after it was identified as a track which went through the requisite amount of iron. This trigger was used with incoming muon fluxes up to 100 per expansion.

The HS used in neutrino experiments with the FNAL 4.6-meter chamber is called an External Muon Identifier or EMI (22), and the arrangement is shown

in Figure 26. It consists of three vertical layers of proportional wire chambers each wrapped around the back third of the chamber (downstream of the coils) and behind a zinc absorber layer. Each chamber is 1.27×1.27 meters square. The wires are spaced by 5 mm, and there are three coordinate sets x, y and u. The readout is by delay line so that while a single track is found with the usual wire spacing resolution, two tracks have to be spaced by 5 cm to be resolved. However, this is a good match to the system, because of the combination of large distances and multiple scattering, and the electronics are relatively inexpensive.

Because there is only a single plane of counters, they do not by themselves determine a direction. The scheme is to record all resolved tracks in the MWPC's and then later to pick only the unambiguous cases where a single non-interacting particle is observed in the chamber and then predicted to go through a particular set of wires in the EMI. Those that satisfy the criteria are then classified as having a very high probability of being muons. Since the chamber is very large, the probability is large that the hadrons produced in the neutrino interactions will themselves interact, so this method of separation of muons has been quite successful.

Data-Gathering Systems

All HS have associated data-gathering systems. In the untriggered mode their main function is data logging and monitoring. In this sense they are similar to the systems used in counter experiments. The information from wire chambers or scintillator hodoscopes is put into the computer on a signal from some coincidence circuit, and at some later time calculations are made and the results displayed. Their most important function is to generate position information accurately enough to do momentum measurements and to match the spark chamber tracks with those measured in the bubble chamber. In addition, they perform the

standard monitoring functions. It is of course very important to have a sample of the data from the downstream electronics analyzed a short time after pictures are taken so as to correlate tracks in test pictures of the bubble chamber with the spark chamber information while the experiment is in progress.

A more complicated use of the data-logging system is used in the triggered mode. An algorithm is needed to decide whether or not to trigger the lights. Since the time for decision is small (several milliseconds), this is usually written in machine language. As an example of such an algorithm we will consider the one written for the experiment using the SLAC HS in order to study the reactions $\pi^+ p \rightarrow K^+ Y^*$ and $K^- p \rightarrow \pi^- Y^*$, with the subsequent decay $Y^* \rightarrow \Lambda + n\pi$, at an energy of 11.6 GeV/c. The trigger for the first reaction was a K^+ meson of momentum greater than 4.5 GeV/c. Referring to Figure 19, the algorithm had to:

(a) Find all possible tracks that went through all three MWPC stations.

(b) Find all incoming beam tracks.

(c) Calculate the intersection point between each MWPC track and the beam track to find which outgoing tracks came from the fiducial volume of the BC.

(d) Calculate the momentum of all good candidates in step (c).

(e) See which of the tracks of step (d) project back to the proper hodoscope counter.

(f) Check to see whether the pulse height in the Cerenkov counter (24) corresponds to that for a K meson of the correct momentum. The

Cerenkov counter has a three-meter path length, so that K mesons of momentum between 8 and 11 GeV/c can be distinguished from pions and protons by pulse height.

When conditions (a)-(f) are satisfied, the chamber lights are flashed. The time for the execution goes roughly as the third power of the number of tracks.

Because of the limited time available for computation which is imposed by the thermodynamics of the bubble chamber (2-3 msec), it is instructive to examine in some detail an example of what current technology permits one to do during this time. The system in use with the apparatus of Figure 19 is shown in Figure 27.

HARDWARE The central processor is a Data General Nova 849, which is a 16-bit four-register machine with a memory cycle-time of 800 nanoseconds and a 1.25 megaword/second direct memory access channel. (Devices with controllers external to the CPU chassis are limited to a 500 kiloword/second transfer rate.) It is equipped with hardware floating point and multiply/divide instructions, and a memory mapping and protection unit using 1024-word pages. The total amount of memory is 48 kilowords.

The system has a typewriter master console and a high-speed paper tape reader, used primarily for diagnostics. Two 9-track, 800 byte/inch, 75 inches/second vacuum-column tape drives are used for data recording. A 786 kiloword fixed-head disk is used for nonresident system storage, program swap space, user files, and temporary data sets such as histogram displays. The main operating console is a graphics display storage scope, which is equipped with a hardware hard-copy interface to an electrostatic printer/plotter which also functions as the system printer. Two CAMAC crates provide a connection to the experimental apparatus. Proportional wire chamber data, photomultiplier

pulse heights, scalers, etc, are read in through appropriate modules. The CAMAC crates also provide an interface to a set of 16 program-control-and-monitor switches and display lights (primarily for diagnostic purposes), and also to a 2400 baud link to SLAC's central computing facility.

SOFTWARE The 840 system operates under the control of MRDOS (mapped real-time disk-operating system), a multitasking system supporting separate foreground and background partitions which communicate through a common array in memory. Twelve kilowords of memory are allocated for the resident system, 14 kilowords for the foreground program, 18 kilowords for the background program, and 4 kilowords for the communications array.

Foreground program The foreground program handles all the "time-critical" tasks connected with data reading and recording, and generating a software trigger for the bubble chamber camera. It is initiated by an interrupt coming slightly before the beam spill. Upon receipt of a hardware trigger (based on counter information), PWC data, scalers, pulse heights, etc, are read in via CAMAC in 100 microseconds or so. An experiment-dependent algorithm is then executed in roughly one millisecond to decide whether to take a picture of the triggering event. Provision is made to read in a second hardware trigger in the same 1.6 microsecond beam spill to reduce software dead-time inefficiencies.

If the trigger algorithm generates a positive response to either of the two possible hardware triggers per beam spill, an appropriate signal is sent to the bubble chamber camera, together with various human-readable data for recording on the film. The foreground program then reads in other data not needed for the picture-taking decision, and writes out a fixed-length record on magnetic tape. Various histogram tallies in the communications array are updated, and then the foreground program relinquishes control to the background until the next beam spill.

Background program The background program can run whenever the foreground is idle (which is most of the time). When the background is entered, a "menu" is displayed listing the various routines which may be run. Among the functions available are the following:

(a) Change parameters and logical switches in the foreground.

(b) Display a picture of the current event on the display scope.

(c) Dump the communications array on the scope or printer in octal or decimal format, and update the dump periodically, if it is displayed on the scope.

(d) Start, stop, or clear one or more foreground histogram tallies.

(e) Display one or more histograms on the scope or printer.

(f) Add, delete, or list a histogram definition from the foreground.

Trigger algorithm The object is to derive the interaction vertex and momentum of a (fast) outgoing track. Angles involved are required to be small, and the magnetic field is assumed to be uniform in Y and Z, i.e. $B = B(X)$. The trajectory of a track with momentum p and initial angle θ passing through the system from (X_A, Y_A) to (X_B, Y_B) can be parametrized:

$$\Delta Y_{BA} = Y_B - Y_A = \theta \cdot (X_B - X_A) + I_{AB}/p$$

with

$$I_{AB} = 3 \times 10^{-4} \int_{X_A}^{X_B} dX \int_{X_A}^{X_B} B(X')\, dX' \qquad 19$$

We now utilize the fact that a typical noninteracting beam track calibrates the system, i.e. provides a reference momentum and relates the lateral offsets of one PWC plane with respect to another.

Assuming an interaction point at X_V, we can then derive several equations by considering the upstream and downstream parts of the system with respect to

X_V. For the beam:

$$\Delta Y_{VA} = \theta_0 \cdot \Delta X_{VA} + I_{AV}/p \tag{20}$$

and for the outgoing secondary track

$$\Delta Y_{BV} = \theta_1 \cdot \Delta X_{BV} + I_{VB}/p' \tag{21}$$

Defining $\delta Y = \Delta Y - \Delta Y^{\text{typical beam}} = \Delta Y - \Delta Y^b$, we find

$$\delta Y_{BV} = \left(\theta_1 - \theta_0^b\right) \cdot \Delta X_{BV} + (1/p' - 1/p)\, I_{VB} \tag{22}$$

and

$$\delta Y_{VA} = \left(\theta_0 - \theta_0^b\right) \cdot \Delta X_{VA} \tag{23}$$

(Similar equations exist in Z without the momentum-dependent terms.)

Considering another point (X_C, Y_C) downstream of the interaction vertex (e.g. A, B, C could be PWC's 2, γ and α) we also have

$$\delta Y_{BC} = \left(\theta_1 - \theta_0^b\right) \cdot \Delta X_{BC} + (1/p' - 1/p) \cdot I_{CB} \tag{24}$$

and we are now equipped to derive the vertex and momentum of the outgoing track.

In two experiments at SLAC, matters were simplified by choosing the beam to be parallel. Thus $\theta_0 = \theta_0^b$ always, and we arrive at the following expressions for X_V and p' which are convenient for computation:

$$\Delta X_{BV} = \frac{\Delta X_{BC} \cdot \delta Z_{BV}}{\delta Z_{BC}} = \frac{\Delta X_{BC} \cdot \delta Z_{BA}}{\delta Z_{BC}} \tag{25}$$

and

$$(1/p' - 1/p) = \frac{(\delta Y_{BA} \cdot \Delta X_{BC} - \delta Y_{BC} \cdot \Delta X_{BV})}{F(X_V)} \tag{26}$$

where

$$F(X_V) = I_{VC} \cdot \Delta X_{BV} - I_{VB} \cdot \Delta X_{CV} \tag{27}$$

The main limitation on the programming of the algorithm is the requirement that the time spent in making a decision to take a picture should not exceed 3 msec. The program is therefore coded in NOVA assembler language using 16-bit integer arithmetic, with the intermediate results of the calculations being restricted in magnitude to avoid overflows. Lengthy instructions, such as multiply and divide, are avoided wherever possible. In order to complete the calculations in the allowed time, limits are placed on multiplicities, etc, in the PWC's, and certain numerical approximations are made. For example, the quantity ΔX_{BC} (= 125 cm) in Equation 25 is replaced by the value 64 which serves the dual purpose of limiting the size of the result and avoiding a multiplication.

The following steps are executed in the algorithm used in the SLAC experiments:

(1) Check that PWC 2 saw at least one, but no more than two, beam particles. With no information to link Y and Z in the beam planes, more than two hits in each plane leads to spurious triggers as well as consuming too much time.

(2) Multiplicity cuts are made on the number of hits in the downstream PWC's α, β and γ.

(3) Matched points are found in PWC's α, β, γ and saved for later use. More than five matches in two PWC's causes the trigger to be rejected immediately.

(4) It is now possible to decide which pair of downstream PWC's are to be used for the first try at the calculation. Clearly it is desirable to select the two planes with the largest separation to give greatest possible accuracy. The method using two PWC's was

eventually preferred to making a fit using information from all three downstream planes simply because of the higher efficiency thereby obtained.

(5) The beam tracks found in PWC 2 are projected into the downstream PWC's being used, and the predictions are compared with the matched points already found to remove any noninteracting beam tracks. For example, due to the spacing of the planes, predictions of Z_α, Z_γ can be made according to

$$Z_\gamma = Z_2 + \Delta Z^b_{\gamma 2} + \delta Z_{21}$$

$$Z_\alpha = Z_2 + \Delta Z^b_{\gamma 2} + 3/4\ \delta Z_{21}$$

for a nonparallel beam. In the case of a parallel beam, the predictions are simplified even further by the absence of the δZ_{21} terms. Constants like $\Delta Z^b_{\gamma 2}$ are obtained by taking data triggering on incident beam tracks only.

(6) The vertex calculation can now be attempted, as shown in Figure 28. The horizontal line defines the path of a noninteracting beam track, i.e. $\delta Z_{\gamma 2} = 0$. X_V^{max}, X_V^{min} are the limits of the fiducial volume.

To avoid wasting time on unnecessary divisions (Equation 25), we do the following:

(a) Using $\delta Z_{\gamma 2}$ and a table of values, we check that $\delta Z_{\gamma\alpha}$ is within the fiducial volume, taking into account the possibility of multiple scattering.

(b) If this is so and the angular deviation of the secondary from the beam track is sufficiently large, then the vertex is calculated. If the dip is too small the vertex is imposed.

(7) Once a vertex has been assigned, the momentum calculation is possible. Certain obvious checks (such as that $\delta Y_{\gamma\alpha}$ is small enough for the track to be within the momentum range of interest) are made, and then the substitution in Equation 26 is made. The value of the field function $F(X_V)$ (Equation 27) is obtained from a table constructed separately from a map of the magnetic field.

(8) Finally, using the calculated momentum, the track is projected into the PWC so far unused, and predictions are made for Y, U and Z. Confirmation is required from at least one of these before the trigger is accepted.

The steps described in Equations 23-26 are contained within a loop such that if at any point the calculation is unsuccessful it is possible to continue with, e.g. the next Z_α. It is to be noted, however, that considerable time can be gained by ordering the computation correctly. The wire numbers are arranged in ascending order, which can often prove useful in eliminating impossible combinations.

Should the two PWC calculations be unsuccessful, it is often possible to try another pair of PWC's, in which case the steps in Equations 23-26 are repeated.

5 PERFORMANCE OF HYBRID SYSTEMS

In this section we will examine how well various operating HS have performed. For all systems this includes the accuracy of momentum and missing mass determination, as well as an evaluation of the losses due to limitations on acceptance imposed by the downstream system. In addition, on-line systems must be evaluated in terms of the efficiency and validity of their trigger systems.

Since track-matching and momentum measurements are intimately connected, we will treat them together and begin with a general description of off-line track-matching procedure.

Off-Line Track Matching

Usually the track measured on the bubble chamber film, together with its measurement errors, is projected into the space occupied by the wire chambers (either up or downstream). Then the probability is calculated that the projected BC track and the observed sparks in the wire chambers do indeed match within their errors. This probability distribution is plotted in order to decide under what conditions an event is acceptable. The position of the vertex of the event in the hydrogen is well-known in all three coordinates, and this fact plays a major role in the procedure for rejection of spurious tracks formed in the spark chambers.

Usually, the space between the BC and WSC systems is filled only with the fringe magnetic field of the bubble chamber magnet. Since this is not uniform it must be measured to $\pm 1/2\%$ at each point so as not to contribute a significant error in the measured momentum.

In the following treatment (25) we evaluate the probability of a match at the first wire chamber plane downstream (or upstream) of the bubble chamber. Other treatments (26, 27) use the vertex position in the chamber. We assume that all variables are transformed to the bubble chamber space, and we define a five-vector called

$$V = \begin{pmatrix} z \\ \theta \\ y \\ \phi \\ p \end{pmatrix}$$

where z and y are the coordinates measured perpendicular to an x axis lying in the general direction of the beam, θ is the dip angle, ϕ is the azimuth angle, and p is the momentum of the particle to be matched. All variables are evaluated at an x somewhere along the bubble chamber track, usually at the vertex or at the end of the track. This track projected to the first spark chamber plane yields a four-vector

$$V_b = \begin{pmatrix} z^b \\ \theta^b \\ y^b \\ \phi^b \end{pmatrix}$$

The error matrix associated with V_b is obtained by propagating the error at the vertex using a matrix $R = (dV_b/dV)$.

Since there is a magnetic field between x and x_b, R is a 4×5 matrix which can be taken to be the same as that used in first-order beam transport theory, namely, the product of R(bend)·R(drift). To a good approximation, this beam transport consists of a bending magnet which turns the track through $\alpha = \phi^b - \phi$ and has an effective length L followed by a drift of length S. Then

$$R(\text{drift}) = \begin{pmatrix} 1 & s & 0 & 0 & 0 \\ 0 & 1 & 0 & 0 & 0 \\ 0 & 0 & 1 & 0 & 0 \\ 0 & 0 & 0 & 1 & 0 \end{pmatrix}$$

$$R(\text{bend}) = \begin{pmatrix} 0 & L & 0 & 0 & 0 \\ 0 & 1 & 0 & 0 & 0 \\ 0 & 0 & 1 & L\cos\alpha/2 & \dfrac{-L\sin\alpha/2}{p} \\ 0 & 0 & 0 & 1 & \dfrac{-L\tan\alpha/2}{p} \end{pmatrix}$$

Here σ_b, the 4×4 error matrix on V_b, is $\sigma_b = R\sigma R^T$. Again σ is evaluated from the bubble chamber fitting program.

The above does not yet include multiple scattering in the region between the end of the measured track and the coordinate x_b. This includes Coulomb scattering in the hydrogen downstream of the measured track, beam windows in the bubble chamber and its vacuum tank, and in any counters or other material between the bubble chamber and the first spark chamber plane.

To treat Coulomb scattering (28), each scatterer, i, is characterized by two independent variables in each of two perpendicular planes, namely, α_i and β_i, the virtual displacement and scattering angle at its center. In the mean we have:

$$\begin{aligned} \langle \alpha_i^2 \rangle &= \theta_s^2 L_i^3/24 \\ \langle \beta_i^2 \rangle &= \theta_s^2 L_i/2 \\ \langle \alpha_i \beta_i \rangle &= 0 \end{aligned} \qquad 27$$

when L_i is the length of the scatterer i and

$$\frac{\theta_s^2}{2} = \left(\frac{15 \text{ MeV}}{\rho\beta}\right)^2 \frac{1}{X_0} \qquad 28$$

then

$$\sigma_i = \begin{pmatrix} \langle \alpha^2 \rangle & 0 & 0 & 0 \\ 0 & \langle \beta^2 \rangle & 0 & 0 \\ 0 & 0 & \langle \alpha^2 \rangle & 0 \\ 0 & 0 & 0 & \langle \beta^2 \rangle \end{pmatrix}$$

Call ℓ_i the drift distance between the center of the scatterer i and the plane of the first SC, and define the drift matrices as

$$D(\ell_i) = \begin{pmatrix} 1 & \ell_i & 0 & 0 \\ 0 & 1 & 0 & 0 \\ 0 & 0 & 1 & \ell_i \\ 0 & 0 & 0 & 1 \end{pmatrix}$$

Then the total Coulomb scattering error at the first downstream SC plane is the sum

$$\sigma_c = \sum_{i=1}^{N} D(\ell_i)\ \sigma_i D^T(\ell_i) \qquad 29$$

where N is the total number of scatterers.

The spark chamber four-vector is

$$V_s = \begin{pmatrix} z^s \\ \theta^s \\ y^s \\ \phi^s \end{pmatrix}$$

and its error matrix, σ_s, usually does not include any Coulomb scattering error.

The goodness of match between bubble chamber and wire chamber is now given by

$$\chi^2 = (V_b - V_s)^T\ (\sigma_b + \sigma_c + \sigma_s)^{-1}\ (V_b - V_s) \qquad 30$$

The results of using this procedure in an actual experiment, namely, the study of 14 GeV/c $\pi^+ p$ interactions in the SLAC 1-meter hybrid system (see Figure 21), are shown in Figures 29 through 33, which describe in detail how well the components of the five-vectors match up, and in Figure 34, which shows the χ^2 distribution for Equation 30. These show that the bubble chamber and wire chamber measurements agree for outgoing tracks to ±1.5 mm and for angles to ±1.5 milliradians in ϕ and ±2.5 milliradians in θ.

For off-line purposes, the upstream and downstream wire chamber values were used. According to G. C. Chadwick (26), a final, fitted error of ±0.3 milliradians in ϕ and ±0.5 milliradians in θ was achieved.

Missing Mass and Momentum Accuracy

OFF-LINE At FNAL energies, the error contribution of Coulomb scattering is relatively smaller, and more accurate results can be obtained. Bugg (29) reports results from matching beam tracks in the 78-cm FNAL chamber with the same tracks as determined by an upstream PWC spectrometer. A similar set of curves to those displayed for the 14 GeV/c case is shown in Figures 35 and 36.

Since in these measurements the incident angle is known very well from the wire chamber measurements, the σ's in Figures 35a and 35b are the angle errors introduced by the bubble chamber measurements, and these must be used when calculating the momentum of secondary tracks produced in an interaction. Bugg (29) has provided the information in Table 4, which summarizes the accuracies in space and momenta that have been achieved with the FNAL HS.

ON-LINE The on-line momentum accuracy is important if (1) the trigger depends on the mass of the outgoing particles as determined by pulse height from a downstream Cerenkov counter, (2) the trigger depends on the mass recoiling against the outgoing particle, (3) the trigger depends on the transverse momentum $p_\perp$ of the outgoing particle or on its total four-momentum transfer squared, t. The on-line accuracy depends, among other things, on whether there is a full-fledged spectrometer downstream of the bubble chamber, as in Figure 21, or whether only the fringe field of the bubble chamber magnet is used as the analyzer, as in Figures 19 and 23.

The "on-line" momentum measurement of the triggering track (i.e. the calculation made before bubbles have reached full size) has been used to determine the "missing mass" recoiling against the detected particle in one case and to identify the particle mass in conjunction with the Cerenkov counter in another. For the missing mass calculation, we use

$$MM^2 = M_p^2 + 2M_p(E_{beam} - E_{trig}) + t \qquad 31$$

when t is the four-momentum transfer from beam to trigger particle, and M_p is the proton mass. The beam energy is well defined, and t is restricted to rather small values by the inherent aperture limitation, so that the error on MM^2 is dominated by the error on E_{trig}. Hence we discuss only the momentum error.

In all cases the momentum error scales as the square of the trigger track momentum, or

$$\frac{\Delta p}{p} = Ap$$

The most straight-forward momentum determination uses only the downstream spectrometer measurements. In a diffractive πp scattering experiment (see Figure 21) a 29 kilogauss-meter dipole magnet was used, surrounded by four wire chamber stations. The two stations between the bubble chamber and the dipole were separated by 2.77 m, while behind the dipole the separation was 5.91 m. The bending angle could then be determined to 0.56 milliradian (using 1 mm uncertainty at each wire plane), which resulted in a momentum error coefficient A = 0.065% per GeV/c. This implied an error in the missing mass (using Equation 31) of $\sim$ 100 MeV at single π threshold. In contrast, the missing mass error for MM = 3 GeV was only 10 MeV.

In the later system, a large Cerenkov counter replaced the magnetic spectrometer, so only the bending power of the bubble chamber fringe field was available to use with this method (see Figure 19). Its accuracy was, however, quite adequate for particle identification, since approximately 15.3 kG-m of bending power was available between the PWC planes α, β and γ. Each of these had three sets of wires z, y and a diagonal set, u. The coordinate x is measured along the beam direction.

The momentum measurement comes from the displacement of the spark at y_β from a straight line joining the sparks at y_α and y_γ:

$$s = y_\beta - y_\alpha - .3464\ (y_\gamma - y_\alpha) \qquad 32$$

when the numerical factor is the ratio of the α-β and α-γ separations. For a 10 GeV/c track, $s \approx 5$ mm, or only 2.5 wire spacings. However, a study of tracks found in the downstream system shows that an effective "setting error" of a single plane is ±0.7 mm (we note that if two adjacent wires fired we used the average location). From Equation 32 we find

$$\Delta s = 0.87 \text{ mm}$$

$$\frac{\Delta p}{p} = \frac{\Delta s}{s} = \frac{.87 \text{ mm}}{5 \text{ mm}} \times \frac{p}{10 \text{ (GeV/c)}} \qquad 33$$

$$A = 1.7\%/\text{GeV/c}$$

The resolution coefficient A is 26 times worse than when the separate magnetic spectrometer was used. This makes the missing mass measurement at single particle threshold unusable: however, at MM = 3 GeV, the resolution would be ±260 MeV.

In the experiment to trigger on the reaction $\pi^+ p \rightarrow K^+ X^+$ at 11.6 GeV/c, we used the momentum measurement only to exclude triggering particles below

4.5 GeV/c. At that momentum, we find $\Delta p/p \simeq 7.5\%$, $\Delta p = 345$ MeV/c, which was quite adequate for that purpose.

The above method of momentum measurement was not used in this particular experiment because the 1.5 μsec beam pulse width of SLAC requires high detection efficiency in the planes used. The alternate procedure was to search for y, z and u spark triplets in any 2 pairs of planes, project the z orbit (i.e. in the "unbent" plane parallel to the magnetic field) back into the bubble chamber from both downstream and upstream PWC's. The intersection of these orbits then locates the event vertex, x_v. The y plane orbits were then similarly projected, and the discrepancy of these projections at x_v measures the outgoing particle momentum.

The result of using this algorithm is a considerable improvement in on-line momentum accuracy as well as improving the detection efficiency. The accuracy is downgraded by multiple scattering in the hydrogen and bubble chamber entry and exit windows, but much more bending power is used. The error calculation is complicated (30) and resolution depends upon the location x_v of the event vertex within the bubble chamber volume, and on the azimuth of the outgoing track with respect to the field direction. We found

$$A = A(x_v)/\cos\theta$$

This dependence occurs because, if the dip angle is small, the vertex x_v cannot be well located. However, if the production angle is small, the calculation becomes insensitive to x_v. Therefore in practice, when small dip was observed, the value of x_v was taken to be at the center of the chamber.

The calculated values of $A(x_v)$, including the effect of multiple scattering, are shown in Figure 37 as a function of x_v corrected to BC track length L. There we see that for events at the beginning of the fiducial volume we can achieve

2.5% momentum resolution for a 10 GeV/c track ($\Delta MM \approx 250$ MeV at single particle threshold), but for events far downstream the precision becomes comparable to that for the first method.

Missing Mass Errors

ON-LINE For some experiments it is convenient to include a missing mass cutoff as part of the trigger. The accuracy of this trigger depends on the on-line determination of the production angle and momentum of the fast triggering particle against which the MM is recoiling.

For the system shown in Figure 21 the error on missing mass is ~ 150 MeV, small enough to eliminate most elastic events. If a downstream spectrometer is not used, but rather the fringe field of the bubble chamber magnet, such as in Figures 19 and 25, the error in MM becomes larger and in fact has not been used as part of an on-line trigger scheme in any actual experiment up to the date of this writing.

OFF-LINE Here, missing mass resolution is, of course, much improved again for the main reason that the vertex is known. There are two cases, one in which the missing mass is calculated for a fitted event, e.g. one in which only one neutral particle is present, and the central values of the measured momenta and angles are displaced in order to make the best fit; and two, where there are no constraints and include those with more than one missing neutral. The two calculations can be made for the same sample of events in order to see how the fitted events improve the resolution. For the experiment of Figure 21 we compare the two cases $\pi^+ p \rightarrow \pi^+ N^{*+}$ (fitted events) and $\pi^+ p \rightarrow \pi^+ + MM$ (in this case any $n\pi^+$ or $p\pi^o$ combination is treated as unfitted). Figure 38 shows the error in MM against the MM for the fitted cases, and Figure 39 shows the same for the unfitted cases. One sees that in the fitted cases a mass resolution of

<20 MeV is obtained for $n\pi^+$ masses <2 GeV, while the unfitted cases range from 90 MeV at low masses to 3 MeV at 4 GeV. Thus a separation of the single neutral from multiple neutral events can be made with only a 5% residual contamination.

Acceptances

GEOMETRICAL This is determined in most cases (very high energy μ mesons may be excepted) by the fact that the walls of the bubble chamber have to withstand pressures up to 10 atmospheres. This results in walls that are several interaction lengths and many radiation lengths thick. In addition, the bubble chamber magnet coils and iron also contribute a limitation on the geometrical acceptance for triggering particles. (See Figure 1.)

In order to maximize this acceptance, a thin exit window is installed in the downstream end of the chamber. The relative size and thickness of these windows is discussed in Section 3. In addition, the cryogenic chambers are surrounded by a vacuum chamber in which a matching exit window also has to be installed.

TOTAL ACCEPTANCE This is determined by the product of the geometrical acceptance, the effect of the magnetic field, and the effect of the production and decay kinematics. Complicated cases have to be evaluated by the use of a Monte Carlo method. Here we shall discuss some simple cases in order to illustrate the limitations and possibilities.

First we consider the case of a fast-forward single particle in a reaction $a+b \rightarrow c+x$ and define t as the four-momentum transfer between a and c, and M_x as the mass of particle x. The masses of a, b and c are assumed known. One can now calculate for a given chamber the acceptance as a function of t and M_x for this forward particle c in a downstream detector whose position and

dimensions are known. This has been done for a setup such as that shown in Figure 21. As can be seen from Figure 40, and as was mentioned earlier in this section, the downstream spectrometer, while providing high momentum and mass resolution, does that at a sacrifice of acceptance. The same bubble chamber, but with the arrangement shown in Figure 19, has the t and M_x acceptance also shown in Figure 40.

In the case where particle c decays immediately into two or more particles, the acceptance depends on the decay angular distribution. Again each individual case must be studied, but as an illustration we have calculated the acceptance of the system shown in Figure 19 for the following cases:

$$\pi^+ p \rightarrow A_2 p \quad \hookrightarrow K^+ K^o$$

$$\pi^+ p \rightarrow f^o p \quad \hookrightarrow K^+ K^o \qquad (35)$$

with the results shown in Figures 41 and 42.

In general the limitations of the exit window size made the hybrid system a poor choice for the study of forward-going heavy mesons that decay into three or more particles, but an excellent choice for the study of recoil baryon resonances and backward-produced mesons. In cases where the forward meson decays into two particles, a choice has to be made on a case-by-case basis.

Performance of Algorithms for Triggering the Lights

The algorithms for doing the experiment $\pi^+ p \rightarrow K^+ X$, described in Section 2 with the apparatus of Figure 19, have been in operation in a routine manner. The times to do the calculations described in Section 4 are shown in Figure 43. As a result the flash was set to $2\frac{1}{2}$ milliseconds after the interaction occurred.

Approximately 40% of all pictures taken had an event in the fiducial volume. The overall efficiency was checked by taking data with low flux (2-3 particles per pulse) and using the fast counters to trigger the lights, namely, triggering on any interactions in the chamber, recording however all other spark chamber and Čerenkov information. These events were then processed off-line as though they were algorithm-triggered events. From those studies the overall efficiency was found to be 80% for low flux. At high flux (8 particles/pulse) the efficiency drops to 65%. With these data it is possible to calculate how many expansions and how many pictures it would take to do a 500 eV/μb experiment with a flux of 8 particles/pulse and a 3/4 meter effective length of hydrogen when the triggering cross section is 500 μb.

This would be:

$$\left(\frac{127\times 10^{6}\times 1.33}{8}\right)\left(\frac{500}{27,000}\right)\left(\frac{1}{0.6}\right)\left(\frac{1}{0.65}\right) = 10^{6} \text{ pictures}$$

To do the same experiment in an untriggered mode would require 30 million pictures (because of a shorter usable length in hydrogen) in the same chamber, or perhaps 15 million in a two-meter chamber. This ratio of 15 to 1 changes the experiment from an "impossible" to a "possible" state.

Physics Results from Selected Experiments

The most extensive work with an untriggered system was done in the 78-cm chamber at FNAL with the two arrangements previously described and shown in Figures 20 and 24. Much of this work has been reviewed by Whitmore (31). The measurement of the individual particle momenta in the downstream system forms the basis for a study of the inclusive spectra at very high energies and allows comparison with lower energies. The results are shown in Figure 44.

The first thing to notice is the remarkable similarity of the spectra as one changes energy. Apart from diffractive effects, such as the bump at large X for $\pi^{\mp} p \rightarrow \pi^{\mp} X$, what matters most is the c.m. energy of the system which seems to be responsible for the small differences.

A second interesting result comes from the four-constraint channels which work mainly when the forward particle is the same as the incident and the slow proton is identified by ionization.

$$\pi^- p \rightarrow \pi^- p \pi^+ \pi^- \qquad 36a$$

$$\pi^- p \rightarrow \pi^- p \, 2\pi^+ 2\pi^- \qquad 36b$$

$$pp \rightarrow pp \pi^+ \pi^- \qquad 36c$$

$$pp \rightarrow pp \, 2\pi^+ 2\pi^- \qquad 36d$$

Reactions 36c and 36d are from counter experiments at the Intersecting Storage Rings in CERN.

A comparison of reactions 36a with 36c and 36b with 36d is made in Figure 45 and shows that after a rise from threshold both decrease very slowly with incident energy showing that they are processes mainly involving diffractive dissociation of the target nucleon.

Clearly future work with the system depends a great deal on particle identification. The EMI installed behind the FNAL 4.6-m chamber (see Figure 26) has been an important part of an experiment (32) done by a Wisconsin, LBL, FNAL, Hawaii group in which either the decay of a new particle or the semi-leptonic decay of a charmed particle was observed for the first time in neutrino interactions. It is also being used in most neutrino experiments in hydrogen, the results of which are now being analyzed.

A series of reports and papers (33) on nucleon diffraction dissociation, done by a SLAC, California Institute of Technology, LBL group, has shown that, with

the high statistics available from the HS (180 eV/μb), detailed interference effects may be studied. In particular the interference between the nondiffractive $\Delta^{++}(1238)$ resonance and the diffractive component at the same mass has shown the need for nucleon exchange in diffractive dissociation.

The first look at the hadrons associated with inelastic muon scattering was also provided by an HS system (34) which showed that even in the region where scaling begins to set in in e^-p inelastic scattering, that the hadron component still looks very much the same as in photoproduction.

At the present time the first very high statistics experiments are being run in the SLAC HS to look at the exchange degenerate reactions (Equation 3) described earlier. About 20% of a 500 eV/μb exposure has been completed, with the rest scheduled for completion in spring 1977.

Several experiments were performed with the SLAC 38-cm chamber. The first (18), using a trigger for a forward neutron, looked for exotic exchange in the reaction

$$\pi^+ p^+ \rightarrow n\pi^+ \pi^+ \qquad 38$$

by analyzing the backward $\pi^+\pi^+$ system for the presence of resonances. In a relatively short exposure on a new piece of apparatus an upper limit of 2 μb was set by a group from Indiana, Purdue and Vanderbilt.

Another group (20) using the same chamber examined the reaction

$$K_L^o p \rightarrow K^{*o}(892)p \qquad 39$$

using the arrangement of Figure 23. The results give the differences in total and differential cross sections between $K^o p \rightarrow K^{o*}(892)p$ and $\bar{K}^o p \rightarrow \bar{K}^{o*}(892)p$ for momenta between 3 and 12 GeV/c.

A high statistics experiment to study the reaction

$$\pi^- p \rightarrow n X^o$$

at 12 GeV/c incident momentum was carried out by a UCLA group using the arrangement of Figure 22 and required 6×10^7 chamber expansions. Some 240,000 pictures were taken, and the sensitivity of this experiment to backward ρ^o production, after all corrections for efficiency, etc, was 187 ± 7 eV/μb. First comparison of the backward differential cross sections for ρ^o and f mesons show them to have the same slope.

6 FUTURE PLANS FOR HYBRID SYSTEMS

The future of hybrid systems depends on how well one can overcome the present limitations: low intrinsic data-gathering power, primitive particle identification at high momenta, and the biases associated with the downstream trigger system.

One way to improve the data rate is to make the bubble chamber pulse faster. As pointed out in Section 3, small volume chambers have cycled successfully at 36 per second while running in a regular experiment. Other experiments (11) have shown that the thermodynamic properties of fluid hydrogen allow cycle rates up to 90 per second. However, these chambers have been so small so that more interactions take place in the surrounding wall than in the useful liquid volume, and they were thus used only for very specialized experiments. It is however practicable to think of a 2-meter chamber operating at 30 per second if one considers the following:

(1) Keep the chamber as shallow as possible. A high pulse rate requires a short expansion pulse in order to provide enough time between expansions to recompress the bubbles that were formed. The short pulse generates higher harmonics which can give rise to variations in sensitivity throughout the liquid volume. To

minimize this effect, it is necessary to keep the chamber depth as small as possible. In the SLAC one-meter chamber the pulse width is 16 times the time taken by the pressure wave to go across the chamber and back again. A factor of at least 10 should be put into the design parameters.

(2) Keep the bubble size as small as possible. Figure 46a shows a calculation (35) of the time it takes to grow and recompress a bubble of diameter 450 microns in the SLAC one-meter chamber, with operating conditions of 4 atmospheres of vapor pressure (26^{o}K) and 7.16 atmospheres of overpressure. Measured times tend to be 20-30% longer (36). Changing the operating conditions by dropping the temperature one degree K or raising the over-pressure does not decrease the time significantly. However, as can be seen in Figure 46b, if one goes to a bubble diameter of 300 microns, the bubble-kill time is decreased enough to allow 30 per second operation.

(3) Provide proper illumination. It is probably best to use a metal piston in order to get good heat conduction, and the most practical optics is to use some retrodirective material like Scotchlite to cover it with. Some effort should be put into getting a real point source (difficult) or a virtual one (using half-silvered mirrors). Such a source has been designed by J. Ferrie (37) at SLAC and is a great improvement over the usual ring sources used.

A most novel charged particle identifier that has been proposed for use with an HS is ISIS (Identification of Secondaries by Ionization Sampling) developed by an Oxford group (39). This is a large enclosure filled with a mixture of 80% argon

and 20% CO_2 at atmospheric pressure with 300 wires each separated by 1 cm. A large electric field is established between the two side walls of the enclosure and the wires. A charged particle traveling along the three-meter length will create ions along its path that will be attracted to the wires and therefore the ionization of the particle will be sampled 300 times, allowing an accurate determination of the energy loss. This, together with a knowledge of the momentum of the particle, provides a determination of its mass. One interesting aspect of ISIS is that many particles can go through it at once and can be distinguished by the different drift times of the ions from their point of creation to the collecting wires. This is a device that is not particularly useful for counter spectrometers because of its relatively slow (10^{-4} sec) recovery time, but is eminently suitable for use in an HS system. It can be made quite large so that it will not cut into the natural acceptance of the system.

Several new approaches are available to HS systems as electron or photon shower detectors with fairly good spatial resolution. One is the liquid Argon ionization chamber (39). This consists of a cellular structure of lead walls, filled with liquid argon. The shower particles are detected by the pulse from the ionization in the liquid argon. The advantage is that a very large wall of this material can be placed downstream, 20 radiation lengths or so thick and with a 1 cm $\times$ 1 cm spatial resolution. Thus, unambiguous identification of π^o mesons and single electrons is possible. Such a scheme provides neutral and multineutral triggers for the HS, opening up a little known aspect of strong interactions to detailed exploration.

At very high energies, where most particles go forward, the full-fledged downstream spectrometer, using a separate magnet in addition to the fringe field of the bubble chamber, can be used without seriously cutting into the

acceptance of the system. This is most important for missing mass on-line triggers and for good off-line momentum analysis.

A system employing most of these new features (6) is being built for use at CERN, the European Center for Nuclear Research in Geneva and will be installed in the experimental area surrounding the new 400 GeV accelerator there. The general outline of the system is shown in Figure 47. The bubble chamber specifications were given in Section 3. The rest of the system consists of multiwire spark chambers, W_0 and W_1, and drift chambers, D_1, D_2, D_3, a dipole magnet, M_2, and another set of drift chambers, D_4, D_5 and D_6. This much of the system, which consists of two momentum measuring sections, one using the chamber field and the other a downstream spectrometer, will be built first. A second stage is planned which will include two multicell Cerenkov counters and a three-cell ISIS system some 5.5 meters long. A third stage will include two stages of gamma detection labeled FGD and IGD, F for forward and I for intermediate. Note that this HS combine extends capabilities along directions mentioned previously, namely, higher repetition rate, better particle identification and superior momentum definition. Figure 48 shows the momentum resolution they hope to achieve. The particle identification as a function of momentum is shown in Figure 49.

A similar downstream system is being built for use in the NAL HS (40). This will consist of an ISIS, a 5-meter-long Cerenkov counter with eight mirrors, and a detector for forward gamma rays and electrons.

Another HS is now undergoing initial tests at Rutherford. The bubble chamber was described in Section 3, and the HS is depicted schematically in Figure 50. The four cylindrical spark chambers have been designed to provide a high multiplicity trigger, which is possible because the walls of this chamber

are thin enough (3 mm of aluminum) to serve as beam-exit windows. The wire chambers will also be used to ensure that the event took place in the fiducial volume, a very important consideration with small chambers.

A further development, which may be a great help in providing a more unbiased trigger, is the use of solid-state-light-sensitive modules which can be placed in a mosaic whose elements can be made as small as 13 by 13 microns and whose information content can be scanned electronically. With such a device a low-level illumination may be applied to the bubble chamber after the bubbles have grown to almost full size (typically 1.5-2 msec with Scotchlite illumination). This light level can be made too low to sensitize photographic emulsion. There then remains another 1.5-2 msec of readout and calculation time before having to make a decision to flash full-intensity lights and take the photograph. The first application of such a system might be a multiplicity trigger which would be almost totally unbiased insofar as momentum and angle of outgoing tracks is concerned. This would be a marked improvement over previous systems. Encouraging preliminary trials of such devices have been made by F. Villa and D. Freytag of SLAC.

In summary, the HS represents a considerable advance in the use of bubble chambers in high energy physics, especially with charged particle beams. Its use has been extended to the very highest energies, using fixed target accelerators, and it promises to be a very useful tool for many years to come.

Acknowledgments

We wish to thank the following people for providing us with internal notes and information not easily found in the literature: I. Pless, V. Kistiakowsky, L. Montanet, C. Fisher, R. Newport, L. Stevenson, J. T. Carroll, G. Chadwick, R. C. Field, J. Brown, G. Hall, H. Ticho, D. Parker, R. J. Walker, W. Bugg, D. Freytag; and W. T. Kirk for his critical reading of the manuscript.

Literature Cited

1. Alvarez, L. W. 1969. Science 165:1071
Lasinski, T., Barbaro-Galtieri, A., Kelly, R. L., Rittenberg, A., Rosenfeld, A. H., Trippe, T. G., Barash-Schmidt, N., Bricman, C., Chaloupka, V., Söding, P., Roos, M. 1973. Rev. Mod. Phys. 45:S1
2. Watts, T. L., ed. 1970. Proc. Int. Conf. PEPR, 2nd, Cambridge, Mass., 1970, MIT report 2098-60, p. 235.
3. Davey, P. G., Hawes, B. M. 1974. Oxford Conf. Computer Scanning, Nucl. Phys. Lab., Univ. of Oxford, 1974, pp. 15, 17.
4. Watt, R. D. 1973. In Proc. Int. Conf. Instrum. for High Energy Physics, CNEN Frascati, 1973, ed. S. Stipcich, p. 44.
5. Ballam, J., Blumberg, R., Mark, J., Skarpaas, K., St. Lorant, S. J. 1966. In Proc. Int. Conf. Instrum. for High Energy Physics, SLAC, Stanford, California, 1966, ed. D. M. Ritson, pp. 107-121.
6. CERN, Geneva, Switzerland 1976. CERN/SPSC/76-43, Revision 2, May 1976.
7. Powell, W. M., Oswald, L., Griffin, G., Swartz, F. 1963. Rev. Sci. Instrum. 34:1426-29
8. 3M Co., Minneapolis, Minn., registered trade name.
9. Bradner, H. 1960. Ann. Rev. Nucl. Sci. 10:109-160
10. Barrera, F., Byrns, R. A., Eckman, G. J., Hernandez, H. P., Norgren, D. U., Shand, A. J., Watt, R. D. 1964. Adv. Cryogenic Eng. 10:251-58
11. Rogers, A. 1970. In Proc. Int. Conf. Bubble Chamber Tech., ANL, Lagrange, Ill., 1970, ed. M. Derrick, pp. 346-373.

12. Newport, R. W., David, D., Diplock, B. R., Edwards, B.W.H., Turner, W., Wheatley, J. D. 1973. In Proc. Int. Conf. Instrum. for High Energy Physics, CNEN Frascati, 1973, ed. S. Stipcich, pp. 50-59.

13. Fong, D., Heller, M., Shapiro, A. M., Widgoff, M., Bruyant, F., Bogert, D., Johnson, M., Burnstein, R., Fu, C., Petersen, D., Robertson, M., Rubin, H., Sard, R., Snyder, A., Tortora, J., Alyea, D., Chien, C. Y., Lucas, P., Pevsner, A., Zdanis, R., Brau, J., Gunhaus, J., Hafen, E. S. , Hulsizer, R. I., Karshon, U., Kistiakowsky, V., Levy, A., Napier, A., Pless, I. A., Silverman, J., Trepagnier, P. C., Wolfson, J., Yamamoto, R. K., Cohn, H., Ou, T. C., Plano, R., Watts, T., Brucker, E., Koller, E., Stamer, P., Taylor, S., Bugg, W., Condo, G., Handler, T., Hart, E., Kraybill. H., Jung, D. L., Ludlam, T., Taft, H. D. 1976. Nucl. Phys. B 102:386-404

14. Lach, J., Pruss, S. 1971. FNAL Rep. TN-298, Fermi Nat. Accelerator Lab., Batavia, Ill.

15. Smart, W. M., Moriyasu, K., Leith, D.W.G.S., Johnson, W. B., Friday, R. G. 1973. Rev. Sci. Instrum. 44:1584

16. Coombes, R., Fryberger, D., Hitlin, D., Piccioni, R., Porat, D., Dorfan, D. 1972. Nucl. Instrum. Methods 98:317-328

17. Arenton, M. W., Bacino, W. J., Hauptman, J. M. 1976. Paper no. 794 submitted to XVIII Int. Conf. High Energy Physics, Tblisi, 1976.

18. Alam, M. S., Brabson, B. B., Galloway, K., Mercer, R., Baggett, N. N., Fowler, E. C., Huebschman, M. L., Kreymer, A. E., Rogers, A. H., Baglin, C., Hanlon, J., Kamat, R., Panvini, R., Petraske, E., Stone, S., Waters, J., Webster, M. 1974. Phys. Lett. B 53:207-211

19. Gunderson, B., Benvenuti, A., Brush, A., Erwin, A., Mistretta, C., Thompson, M. A., Walker, W. D. 1970. In Proc. Int. Conf. Bubble Chamber Tech., ANL, Lagrange, Ill., 1970, ed. M. Derrick, pp. 582-590.

20. Dorfan, J. M. 1976. Ph.D. thesis. Univ. California, Irvine.

21. Smith, G. A. 1973. A.I.P. Conf. Proc. DPF, American Institute of Physics, New York, 1973.

22. Cence, R. J., Harris, F. A., Parker, S. I., Peters, M. W., Peterson, V. Z., Stenger, V. J., Lynch, G., Marriner, J., Solmitz, F., Stevenson, M. L. 1976. LBL-4816, Lawrence Berkeley Lab., Berkeley, Calif.

23. Bashian, A., Finocchiaro, G., Good, M. L., Grannis, P. D., Guisan, O., Kirz, J., Lee, Y. Y., Pittman, R., Fischer, G. C., Reeder, D. D. 1971. Phys. Rev. D 4:2667-2679

24. Bowden, G. B., Field, R. C., Lewis, R., Hoard, C., Skarpaas, K., Baker, P. 1976. Nucl. Instrum. Methods 138:77

25. Carroll, J. T., Della Negra, M. 1972. SLAC BC Note No. 16, Stanford Linear Accelerator Center, Stanford, Calif.

26. Chadwick, G. 1974. SLAC BC Note No. 48, Stanford Linear Accelerator Center, Stanford, Calif.

27. Bugg, W., Condo, G., Hart, E., Pevsner, A., Sard, R., Snyder, A., Hulsizer, R., Kistiakowsky, V., Trepagnier, P., Cohn, H., McCulloch, R., Mills, M., Dauwe, D. 1973. Bull. APS 18:564, Program Survey. Watts, T., Ou, T., Fong, D., Lucus, H., Pless, I., Trepagnier, P., Wolfson, J., McCulloch, R., Bugg, W., Ludlam, T. 1973. Bull. APS 18:564, Program PWGP.

28. Della Negra, M. 1972. SLAC BC Note No. 15, Stanford Linear Accelerator Center, Stanford, Calif.

29. Bugg, W. M. 1974. FNAL HS Note 30, Fermi Nat. Accelerator Lab., Batavia, Ill. and private communication.

30. Chadwick, G. 1974. SLAC BC Note No. 71, Stanford Linear Accelerator Center, Stanford, Calif.

31. Whitmore, J. 1976. Phys. Rep. C 27:187

32. vonKrogh, J., Fry, W., Camerini, U., Cline, D., Loveless, R. J., Mapp, J., March, R. H., Reeder, D. D., Barbaro-Galtieri, A., Bosetti, P., Lynch, G., Marriner, J., Solmitz, F., Stevenson, M. L., Haidt, D., Harigel, G., Wachsmuth, H., Cence, R., Harris, F., Parker, S., Peters, M., Peterson, V., Stenger, V. (1976). Phys. Rev. Lett. 36:710

33. Ochs, W., Davidson, V., Dzierba, A., Firestone, A., Ford, W., Gomez, R., Nagy, F., Peck, C., Rosenfeld, C., Ballam, J., Carroll, J., Chadwick, G., Linglin, D., Marcelja, F., Moffeit, K., Ely, R., Grether, D., Oddone, P. 1975. Nucl. Phys. B 86:253

Ochs, W., Davidson, V., Dzierba, A., Firestone, A., Ford, W., Gomez, R., Nagy, F., Peck, C., Rosenfeld, C., Ballam, J., Carroll, J., Chadwick, G., Linglin, D., Moffeit, K., Ely, R., Grether, D., Oddone, P. 1976. Nucl. Phys. B 102:405

34. Ballam, J., Bloom, E. D., Carroll, J. T., Chadwick, G. B., Cottrell, R. Leslie, Della Negra, M., DeStaebler, H. C., Gershwin, L. K., Keller, L. P., Mestayer, M. D., Moffeit, K. C., Prescott, C., Stein, S. 1974. Phys. Rev. D 10:765

35. Alexsandrov, Ya. A. 1963. Prib. Tekh. Eksp. 2

36. Harigel, G., Horlitz, G., Wolff, S. 1967. DESY Rep. No. 67/14, Deutsches Elektronen-Synchrotron, Hamburg, West Germany.

37. Ferrie, J., private communication.

38. Allison, W.W.M., Bunch, J. N., Cobb, J. H. 1976. Nucl. Instrum. Methods 133:315

39. Hitlin, D., Martin, J. F., Morehouse, C. C., Abrams, G. S., Briggs, D., Carithers, W., Cooper, S., Devoe, R., Friedberg, C. E., Marsh, D., Shannon, S., Vella, E., Whitaker, J. S. 1976. Nucl. Instrum. Methods 137:225

40. Kistiakowsky, V. 1976. Private communication and NALREP, Fermi Nat. Accelerator Lab., Batavia, Ill.

Footnotes

1. Work supported by the Energy Research and Development Administration.
2. Many of the productive chambers of medium size have been discontinued: the SLAC/LBL 82-inch chamber in 1973; the BNL 80-inch chamber in 1974; the CERN 80-cm chamber in about 1971. The CERN two-meter chamber will likely shut down in 1978.
3. This calculation assumes a two-meter chamber with a useful length of 1.5 meters and 10 tracks per picture. For such a chamber, an automatic measuring machine could measure about 250,000 events per year.

Table 1 Features of SLAC 1-meter RCBC

Visible volume	360 liters
Chamber depth	43 cm
Diameter	1 meter
Glass thickness	19.5 cm
Expansion system	Bellows-sealed piston/hydraulically controlled at 10-12 pulses per second
Beam window	Entrance 1.5 mm stainless Exit 1.5 mm stainless
Magnetic field	26 kG
Magnet weight	285 tons
Refrigeration system	1 kW refrigerator
Illumination system	Bright field (Scotchlite)
Chamber camera control system	Proportional wire chambers, Cerenkov counter, scintillators

Table 2 The SLAC 38-cm Rapid-Cycling Bubble Chamber (11)

Shape	Cylindrical
Beam plane dimensions	38 cm diameter
Depth	14 cm
Approximate visible volume	15 liters
Orientation	Window horizontal
Maximum pulse rate	40 pps (achieved)
Illumination	Scotchlite bright field
Entrance beam window	Single convolution omega bellows, 0.8 mm
Exit beam window	stainless steel
Magnetic field	12 kG (superconducting coil)
Expansion	Electromagnetic

Table 3 Main Characteristics of the Proposed CERN Chamber

Diameter	80 cm
Exit angles for the chamber body	
in the bending plane	$\pm 30^{o}$
in the dip plane	$\pm 13.5^{o}$
Operating fluids	Hydrogen and deuterium
Depth	40 cm
Cycling rate with hydrogen	30 Hz for up to 2 sec each 8 sec
Material in the beam exit windows	< 4% of a collision length
over an angle of $\pm 12^{o}$	< 11.5% of a radiation length
Beam entry window size	± 5 cm horizontally
	± 12 cm vertically
Material in beam entry windows	< 4% of a collision length
	< 11% of a radiation length
Precision with respect to the	50 μm in the bending plane
chamber fiducials	150 μm in the dip plane
Optical resolution	better than 300 μm
Precision of correlation with	once calibrated, to be stable
downstream system	within 100 μm in the bending plane
	and 200 μm in the dip plane

Table 4 Resolution Parameters of the FNAL PWC Hybrid System

I. Angular accuracy

Upstream system	Downstream PWC system	Bubble chamber (track length = 70 cm)
$\sigma\phi = 0.002$ milliradians	$\sigma\phi = 0.12$ milliradians	$\sigma\phi = 0.45$ milliradians
$\sigma\lambda = 0.002$ milliradians	$\sigma\lambda = 0.14$ milliradians	$\sigma\lambda = 1.32$ milliradians

II. Position accuracy at center of bubble chamber

PWC	Bubble chamber
$\sigma_y = 0.4$ mm	$\sigma_y = 0.12$ mm
$\sigma_z = 0.4$ mm	$\sigma_z = 0.34$ mm

III. Momentum

A. Average beam momentum

$p_{beam} = 146.75$ GeV/c Error = 0.4 GeV/c

B. Single-track accuracy on beam tracks (using upstream PWC only)

$\Delta p = 2.1$ GeV/c

$\frac{\Delta p}{p} = 0.011\ p/(\text{GeV/c})$

C. Secondary tracks in downstream PWC system

$\frac{\Delta p}{p} = 0.053\ p/(\text{GeV/c})$ (vtx close to entrance window)

$\frac{\Delta p}{p} = 0.074\ p/(\text{GeV/c})$ (vtx at center of chamber)

(All errors are standard deviations)

Figure Legends

Figure 1 The SLAC one-meter bubble chamber, showing the limitations imposed on the exit aperture by the magnet steel and coils.

Figure 2 A densitometer scan of tracks from the SLAC one-meter bubble chamber. The bubble diameter is 400 microns. The scanning slit was 0.26 mm by 10 mm (parallel to track). The signal-to-noise ratio is 6:1.

Figure 3 An elevation drawing of the SLAC one-meter bubble chamber. The outer shell is the 280-ton magnet. From right to left are shown: the iron shield for the camera, the main glass window, the chamber body with its internal heat exchanger at the top, the hollow expansion piston on which Scotchlite is glued and inside of which are refrigeration loops, the piston drive rod which extends through the vacuum tank out to the room temperature hydraulic expansion system.

Figure 4 Photograph of the SLAC one-meter bubble chamber taken while the chamber was operating at 10 pulses per second. Note the absence of bubbling along the Scotchlite seams.

Figure 5 A cross section of the bellow used on the SLAC one-meter bubble chamber. The effective bellows diameter is 120 cm.

Figure 6 The hydroformed bellows first used with the SLAC one-meter bubble chamber. This bellows was later replaced by the type shown in Figure 5.

Figure 7 The special glass-to-metal seal used in SLAC bubble chambers.

Figure 8 An inflatable-gasket glass-to-metal seal of the type conventionally used in bubble chambers. Note the voids around the indium seal.

Figure 9 The spring-mass equivalent of the expansion system for the SLAC one-meter bubble chamber.

Figure 10 Displacement vs time for the piston system used in the SLAC one-meter bubble chamber.

Figure 11 Cross section of the beam window used in the SLAC one-meter bubble chamber.

Figure 12 A cross-sectional view of the SLAC 38-cm bubble chamber. The bellows has an extended flattened central region in order to provide a thin window for particles through a full 360 degrees. The chamber is immersed in liquid hydrogen for cooling purposes. However, most of the cooling occurs through the top plate. The piston motion (0.125 cm) comes from the curved portion of the bellows.

Figure 13 The bellows assembly for the SLAC 38-cm RCBC.

Figure 14 The spring mass equivalent of the expansion system for the SLAC 38-cm RCBC.

Figure 15 Control circuit for pulsing the SLAC 38-cm RCBC.

Figure 16 Current and stroke vs time for the SLAC 38-cm RCBC.

Figure 17 The chamber-liquid seal-off valve used with the SLAC 38-cm RCBC.

Figure 18 An elevation view of the Rutherford Laboratory rapid-cycling vertex detector (RCVD).

Figure 19 An isometric view of the present SLAC hybrid system.

Figure 20 Schematic diagram of the FNAL hybrid system. The muon detector is not shown. The trajectories of a two-particle event are sketched in.

Figure 21 Top and side views of the first SLAC HS using a downstream spectrometer.

Figure 38 The error in missing mass vs missing mass for three-body events which had a three-constraint fit.

Figure 39 The error in missing mass vs missing mass for three-body events for which no fit was attempted.

Figure 40 The t-acceptance of the SLAC HS for a fixed mass. Note how much this is reduced by the use of a downstream spectrometer.

Figure 41 The t-acceptance and angular acceptance in the SLAC HS for a forward-produced f meson decaying into K^+K^-.

Figure 42 The t-acceptance and angular acceptance in the SLAC HS for a forward-produced A_2 meson decaying into K^oK^-. It is quite evident that three-body decays would have a serious bias in angular acceptance.

Figure 43 Distribution of the time taken to calculate the momentum of the scattered track and the vertex position of the event in the SLAC HS. The cutoff is made at 2.5 milliseconds.

Figure 44 Inclusive distributions in the Feynman variable $x = p^*_\ell / p^*_{\ell\,(max)}$ from data obtained with the FNAL HS compared with lower energy data.

Figure 45 Cross sections for the reactions (a) $pp \rightarrow pp\pi'\pi$ and $\pi p \rightarrow p\pi'\pi$, and (b) $pp \rightarrow pp2\pi^+\pi^-$ and $\pi^-p \rightarrow \pi^-p2\pi^+2\pi^-$ as a function of incident beam momentum. For the ISR points the mass of the $p\pi^+\pi^-$ system is chosen to be less than 2.5 GeV.

Figure 46 Bubble growth and decay time compared with the pressure trace for a maximum bubble size of (a) 450 microns and (b) 300 microns.

Figure 47 Side and top views of the proposed European HS. The Cerenkov counters, ISIS system and gamma detector will be built at a later time.

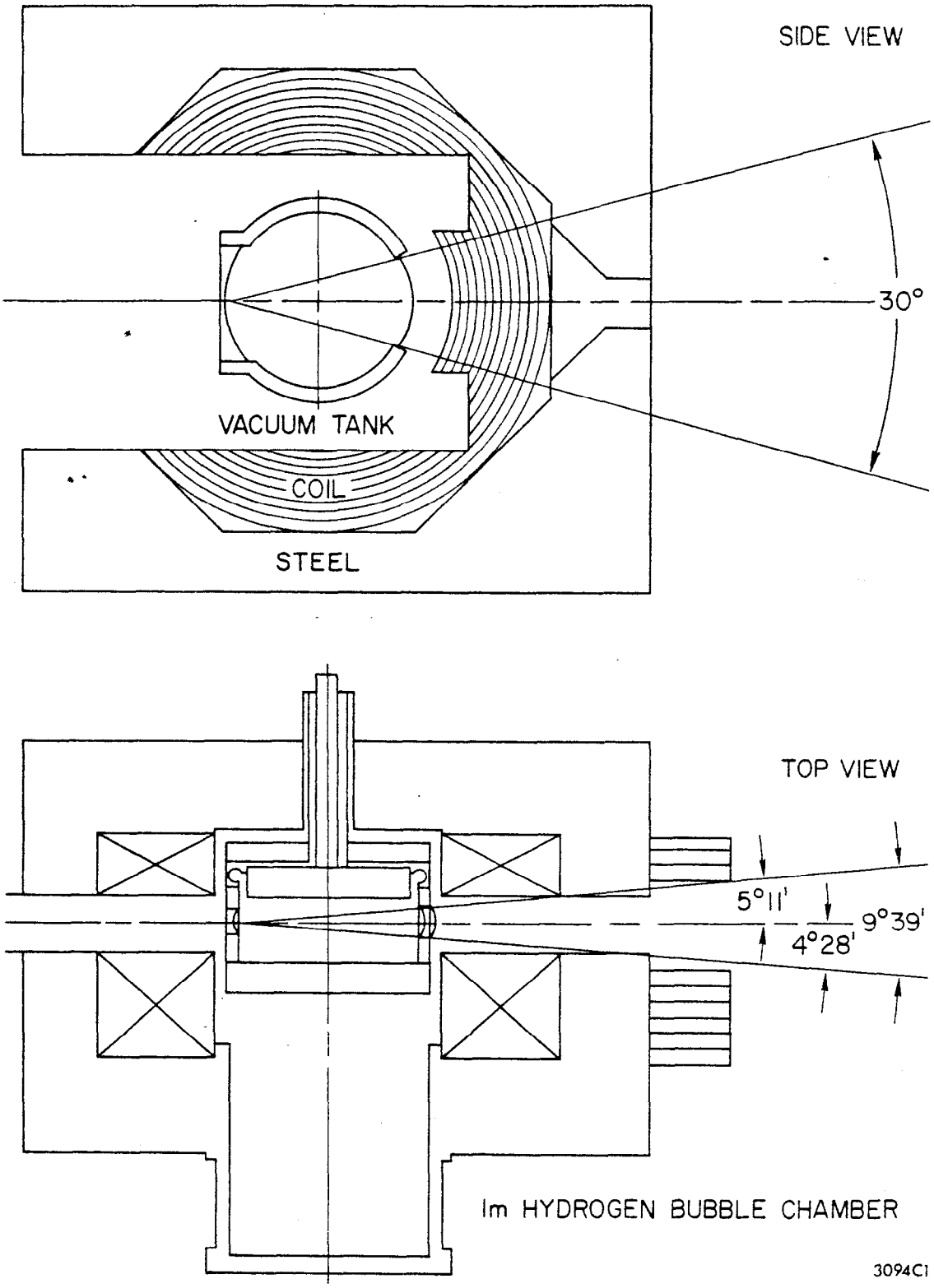
SIDE VIEW
30°
VACUUM TANK
COIL
STEEL
TOP VIEW
5°11'
9°39'
4°28'
Im HYDROGEN BUBBLE CHAMBER
3094C1

Fig. 1

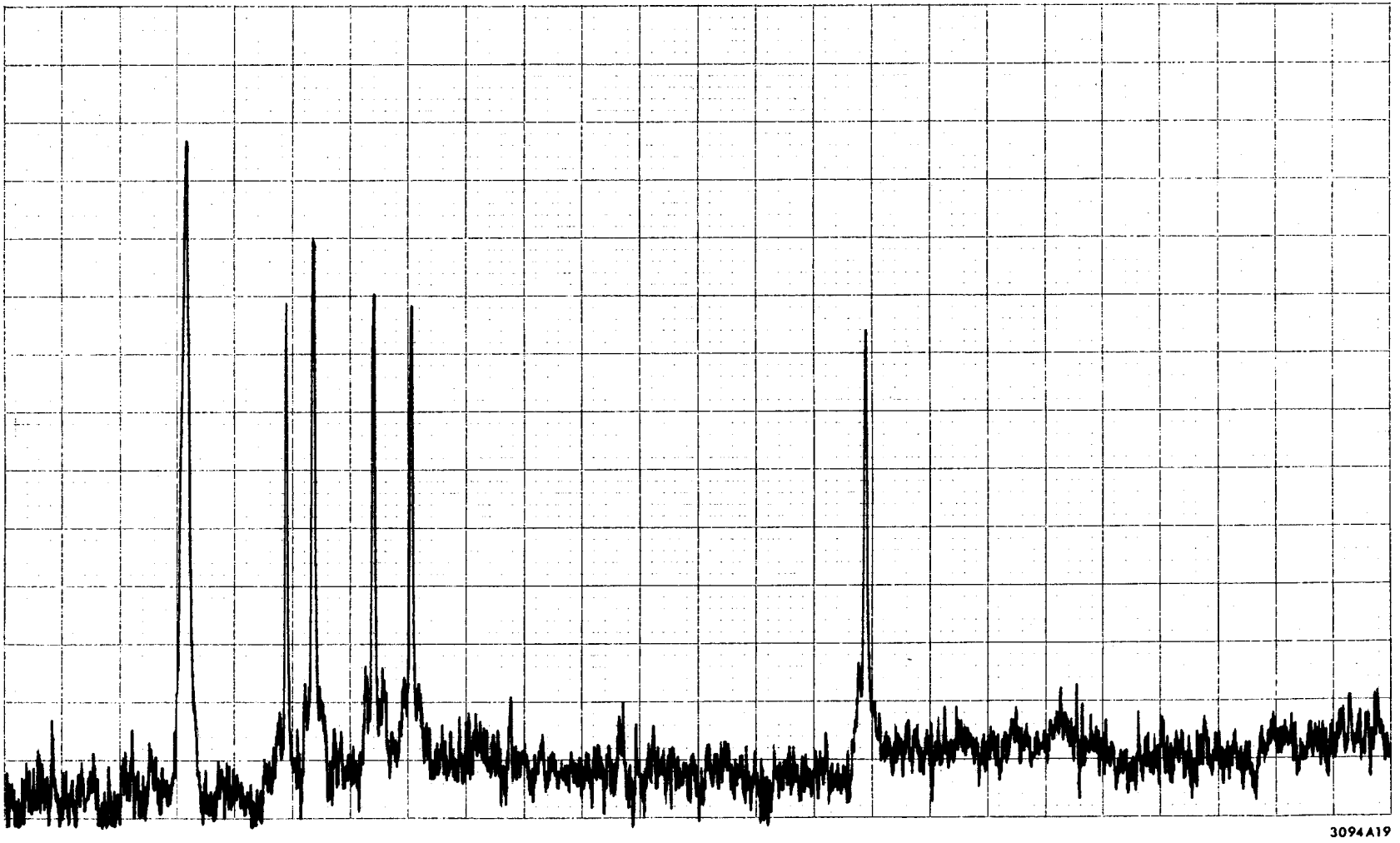

Fig. 2

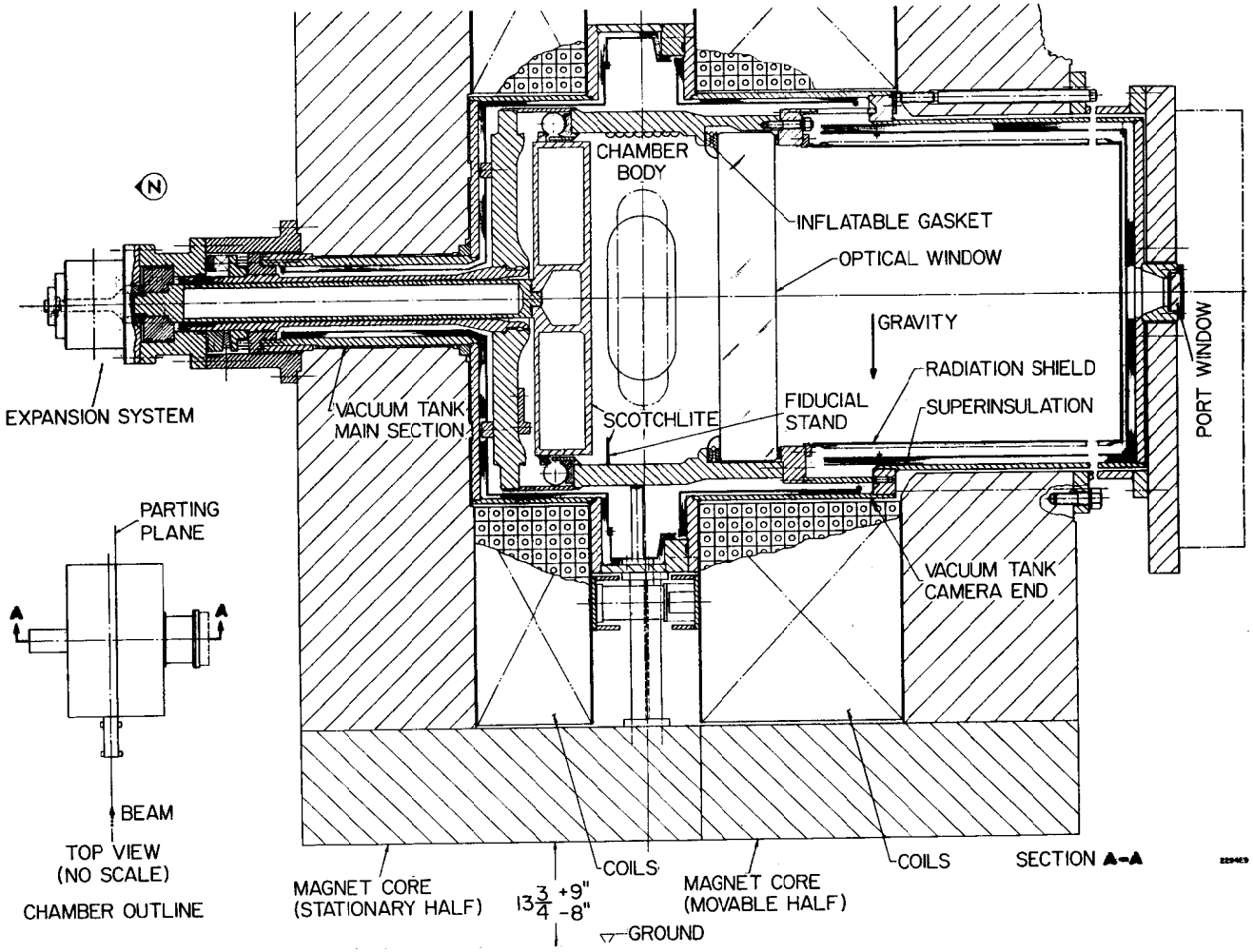
CHAMBER BODY
INFLATABLE GASKET
OPTICAL WINDOW
GRAVITY
RADIATION SHIELD
SUPERINSULATION
PORT WINDOW
EXPANSION SYSTEM
VACUUM TANK MAIN SECTION
SCOTCHLITE
FIDUCIAL STAND
VACUUM TANK CAMERA END
PARTING PLANE
BEAM
TOP VIEW (NO SCALE)
CHAMBER OUTLINE
MAGNET CORE (STATIONARY HALF)
13 3/4 +9" -8"
GROUND
COILS
MAGNET CORE (MOVABLE HALF)
COILS
SECTION A-A

Fig. 3

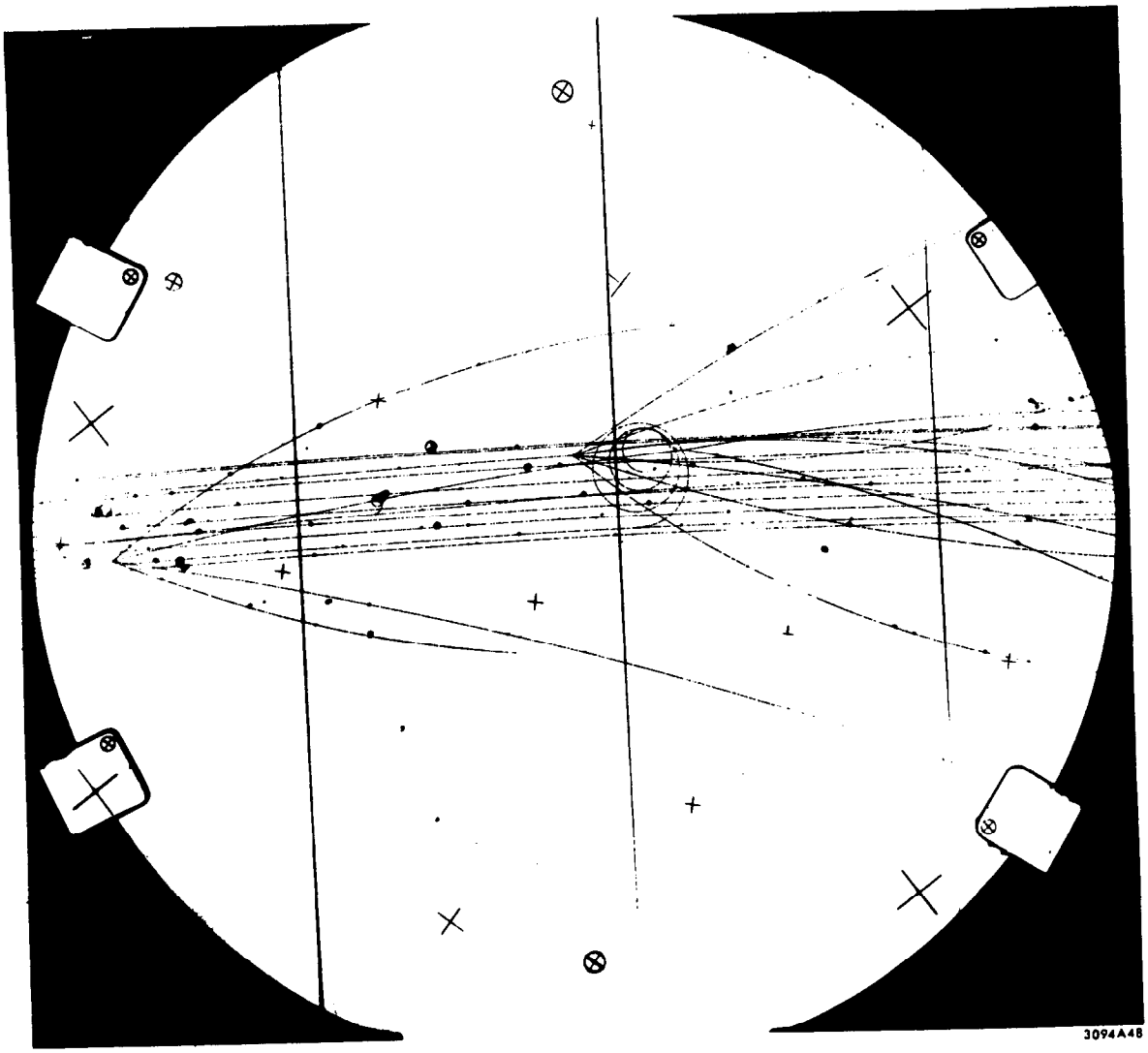

Fig. 4

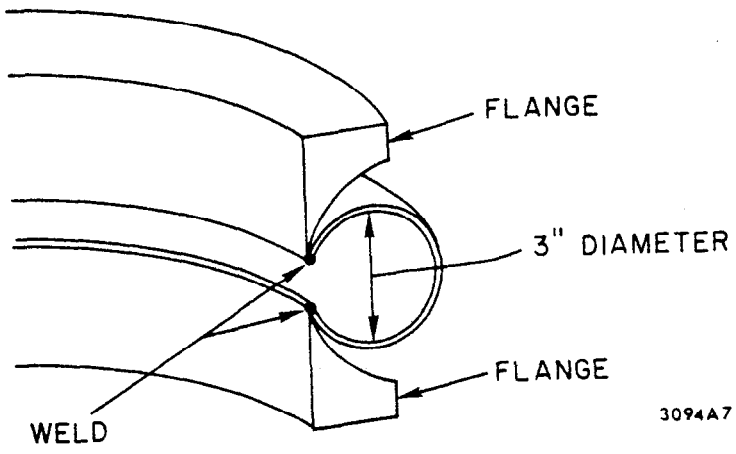

Fig. 5

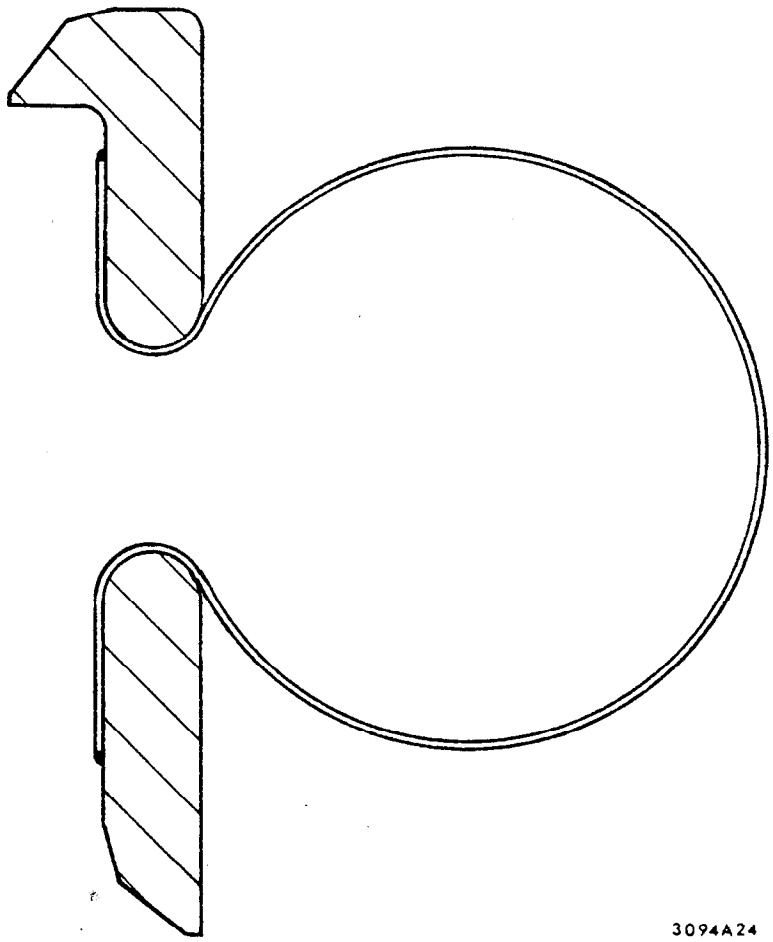

Fig. 6

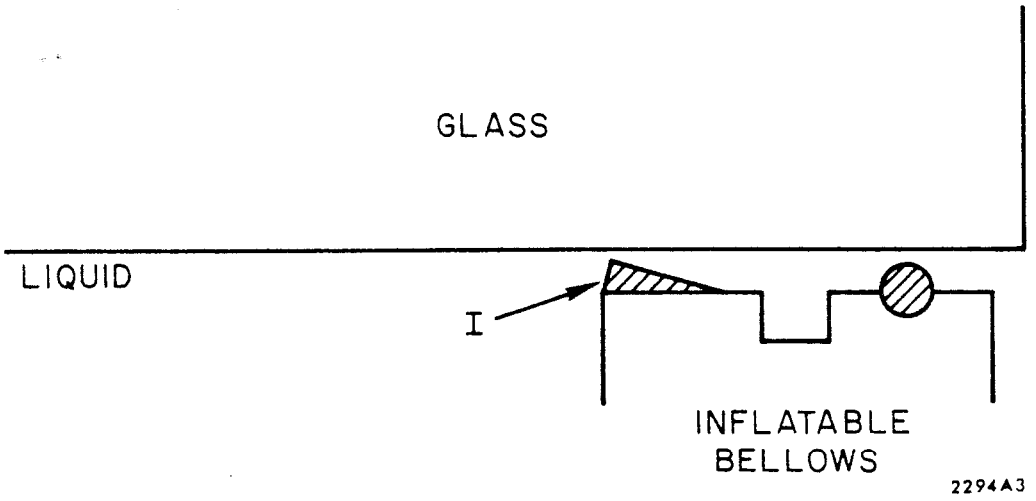

Fig. 7

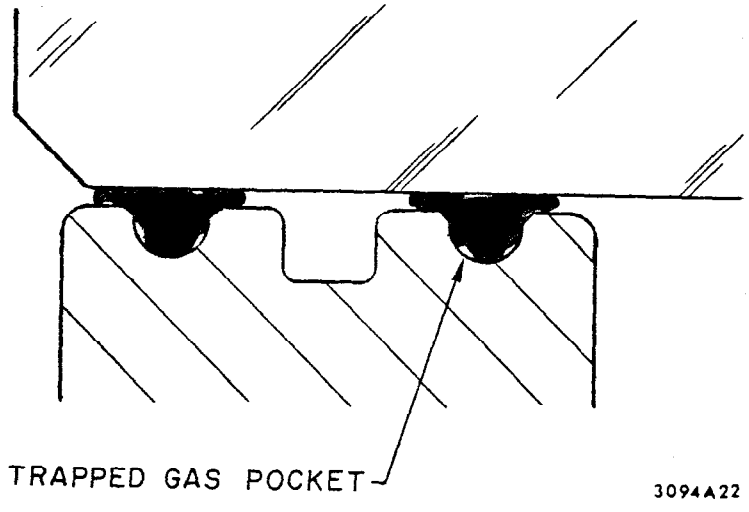

Fig. 8

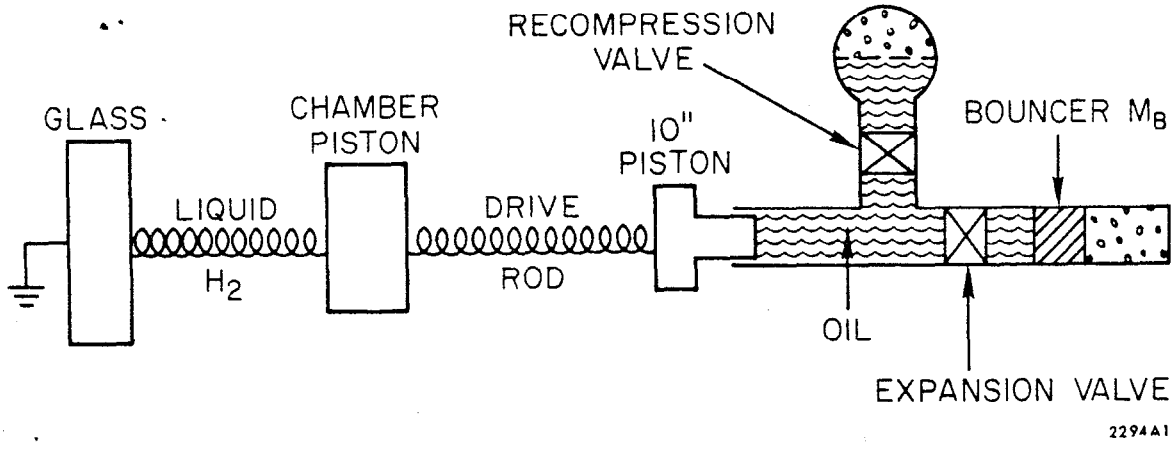
RECOMPRESSION
VALVE
GLASS
CHAMBER
PISTON
10"
PISTON
BOUNCER M_B
LIQUID
H_2
DRIVE
ROD
OIL
EXPANSION VALVE
2294A1

Fig. 9

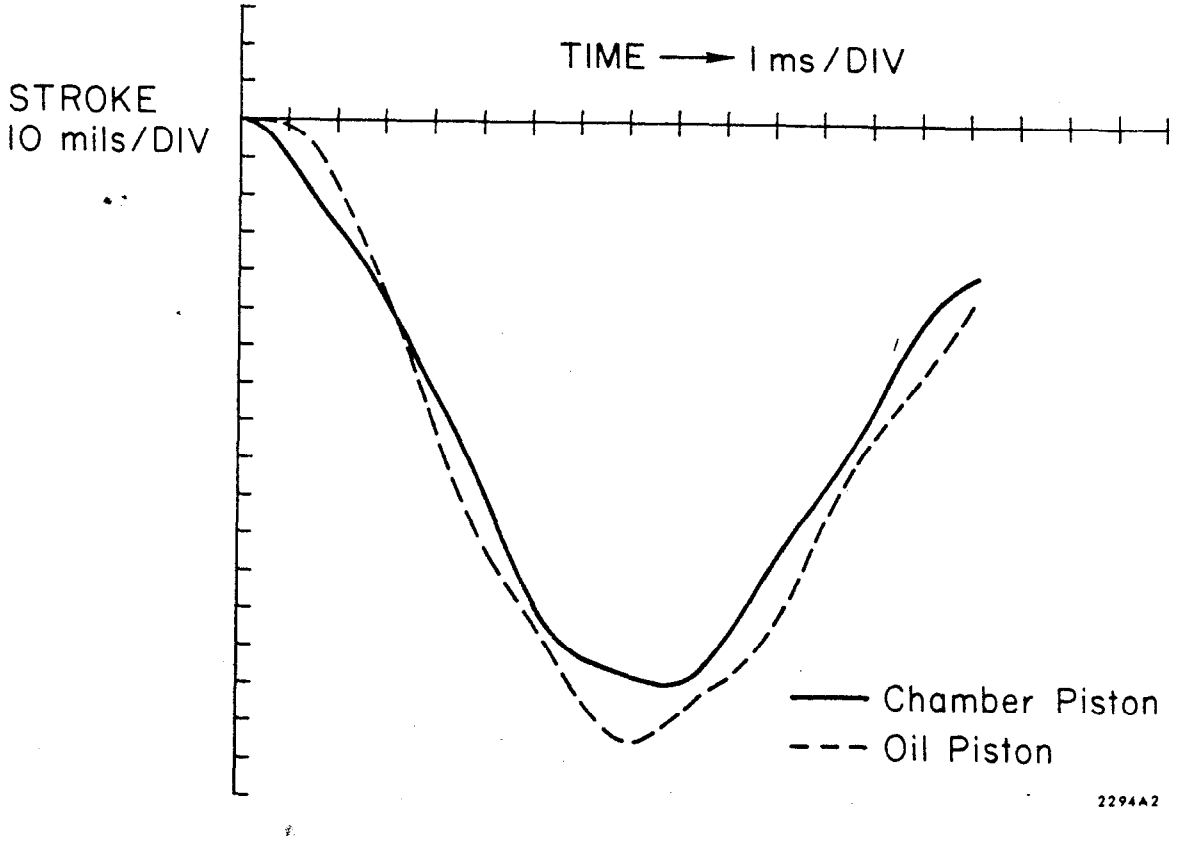
TIME → 1 ms / DIV
STROKE
10 mils/DIV
Chamber Piston
Oil Piston
2294A2

Fig. 10

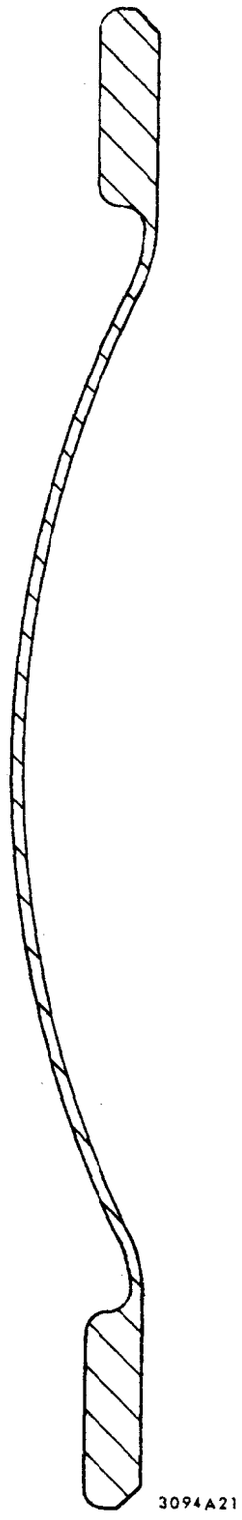

Fig. 11

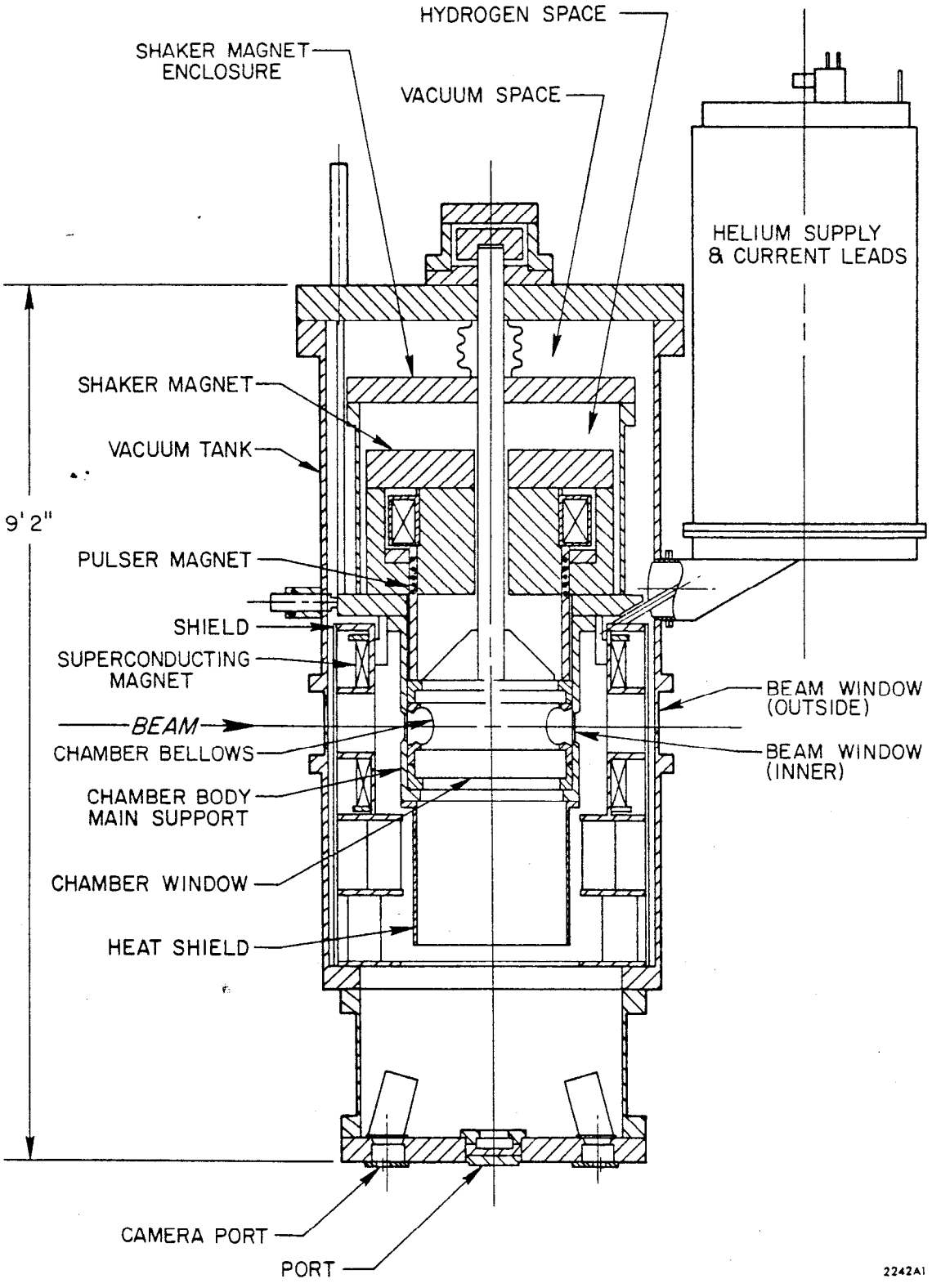
HYDROGEN SPACE
SHAKER MAGNET ENCLOSURE
VACUUM SPACE
HELIUM SUPPLY & CURRENT LEADS
SHAKER MAGNET
VACUUM TANK
9'2"
PULSER MAGNET
SHIELD
SUPERCONDUCTING MAGNET
BEAM WINDOW (OUTSIDE)
BEAM
CHAMBER BELLOWS
BEAM WINDOW (INNER)
CHAMBER BODY MAIN SUPPORT
CHAMBER WINDOW
HEAT SHIELD
CAMERA PORT
PORT
2242A1

Fig. 12

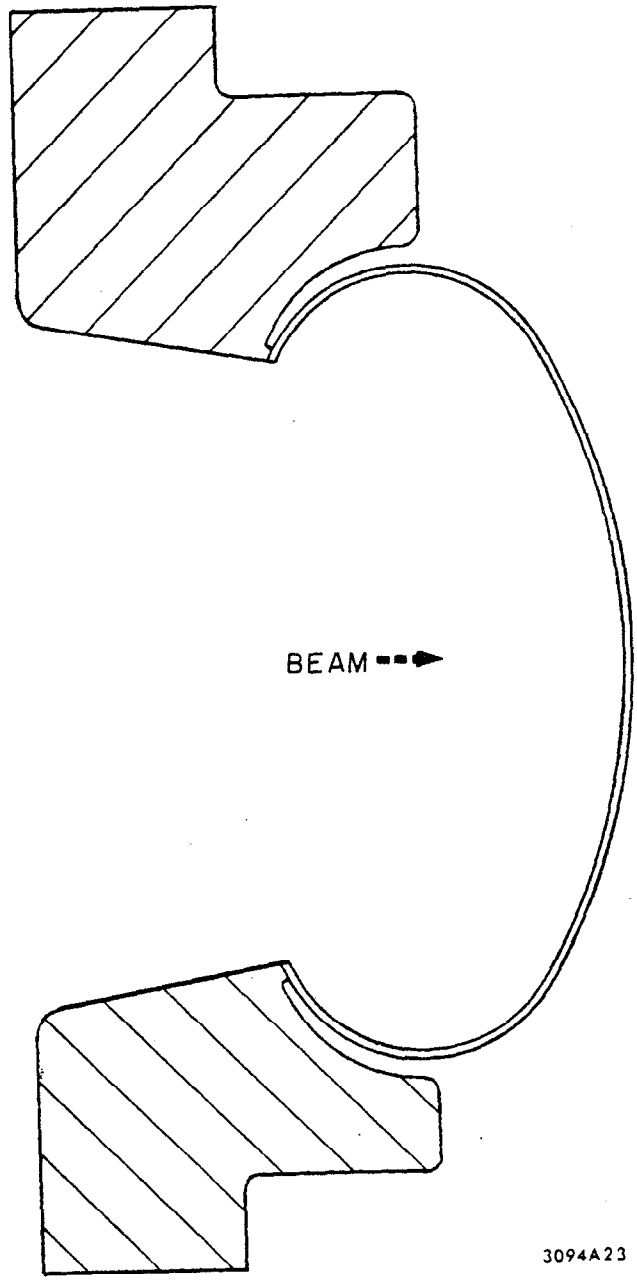

Fig 13

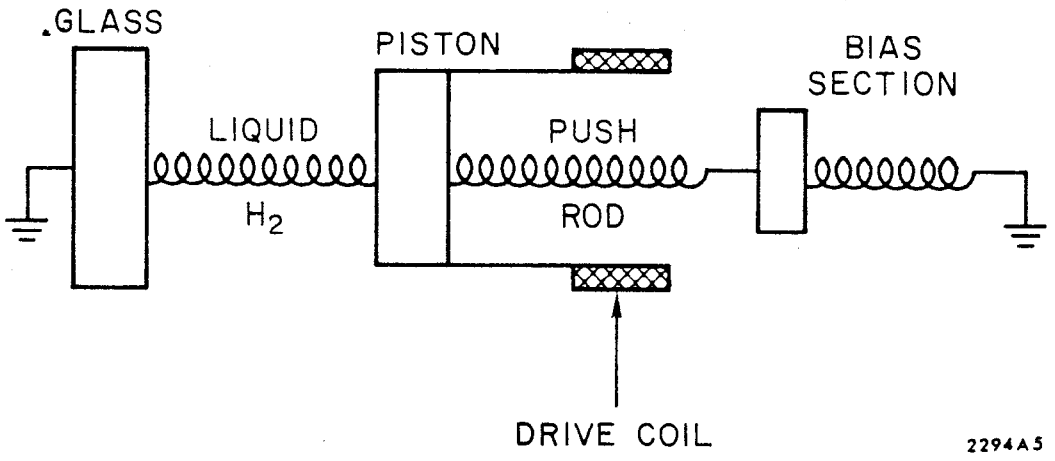
GLASS
PISTON
BIAS
SECTION
LIQUID
H_2
PUSH
ROD
DRIVE COIL
2294A5

Fig. 14

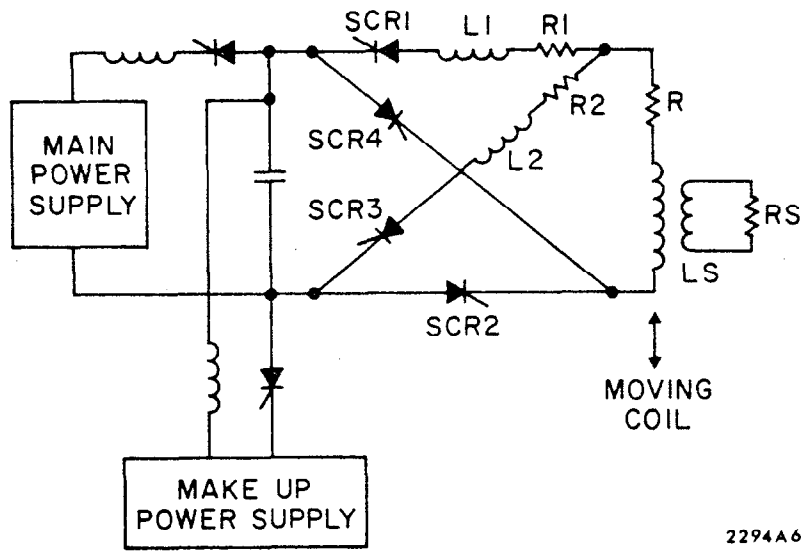
SCR1
L1
R1
R2
R
SCR4
L2
MAIN
POWER
SUPPLY
SCR3
RS
LS
SCR2
MOVING
COIL
MAKE UP
POWER SUPPLY
2294A6

Fig. 15

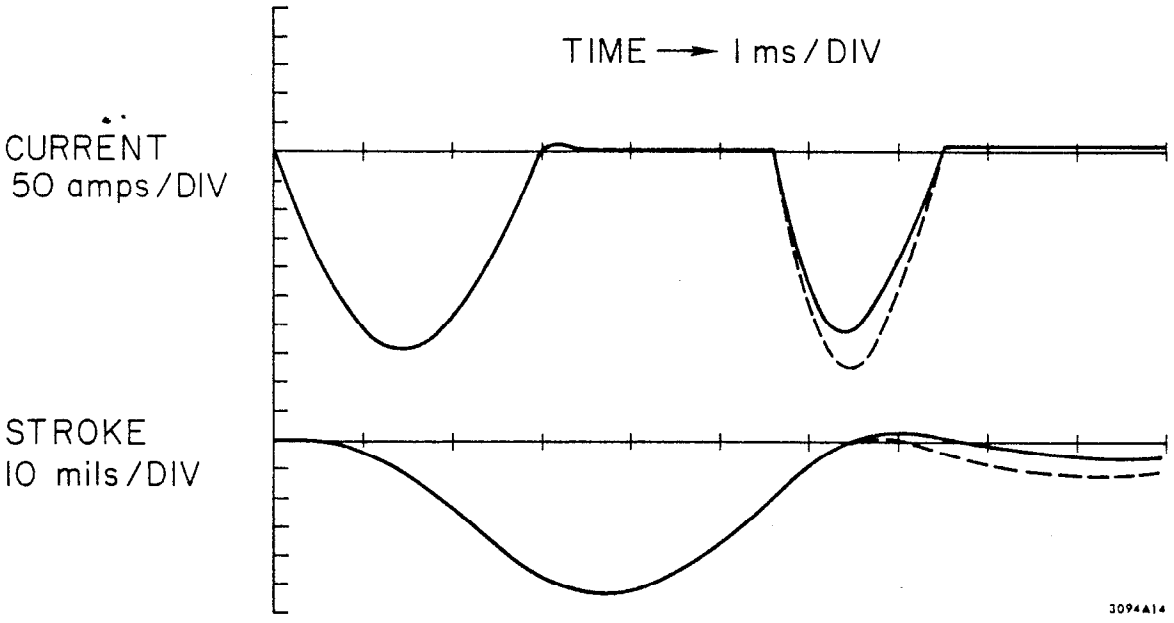

Fig 16

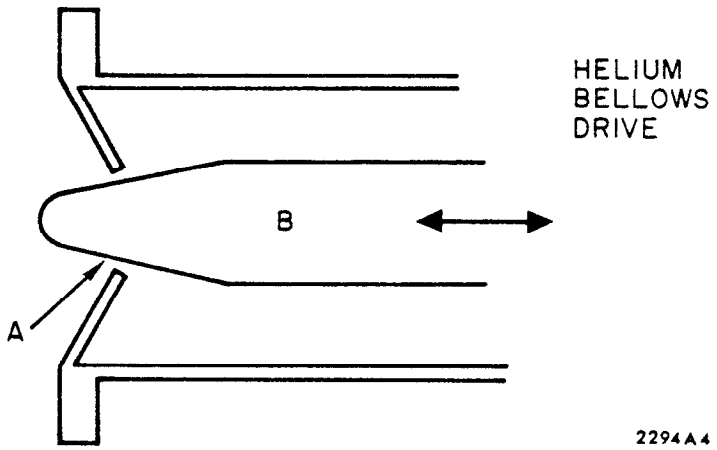

Fig. 17

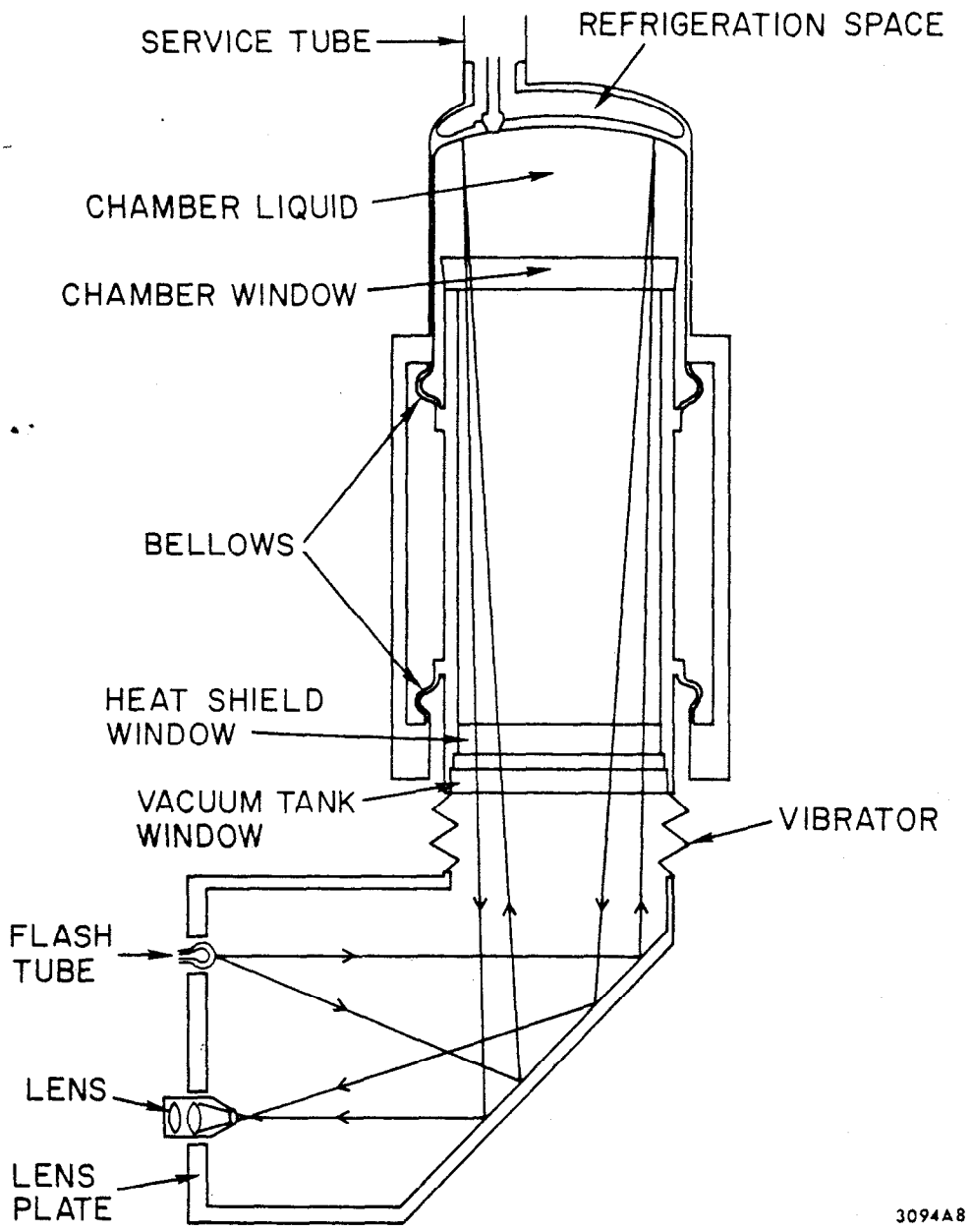
SERVICE TUBE
REFRIGERATION SPACE
CHAMBER LIQUID
CHAMBER WINDOW
BELLOWS
HEAT SHIELD WINDOW
VACUUM TANK WINDOW
VIBRATOR
FLASH TUBE
LENS
LENS PLATE
3094A8

Fig. 18

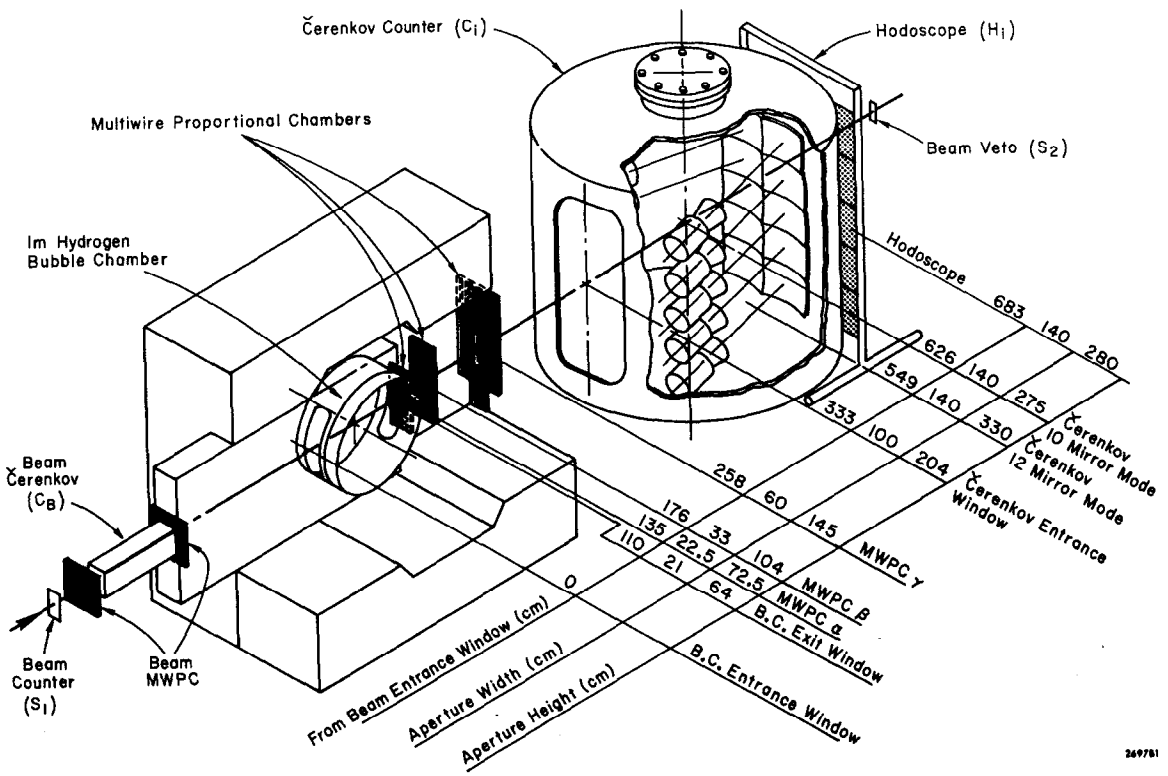
Čerenkov Counter (C_1)
Hodoscope (H_1)
Multiwire Proportional Chambers
Beam Veto (S_2)
1m Hydrogen Bubble Chamber
Hodoscope
683 140 280
626 140 275
549 140 330
333 100 204
258 60 145
176 33 104
135 22.5 72.5
110 21 64
0
Čerenkov 10 Mirror Mode
Čerenkov 12 Mirror Mode
Čerenkov Entrance Window
MWPC γ
MWPC β
MWPC α
B.C. Exit Window
B.C. Entrance Window
Beam Čerenkov (C_B)
Beam Counter (S_1)
Beam MWPC
From Beam Entrance Window (cm)
Aperture Width (cm)
Aperture Height (cm)
249781

Fig. 19

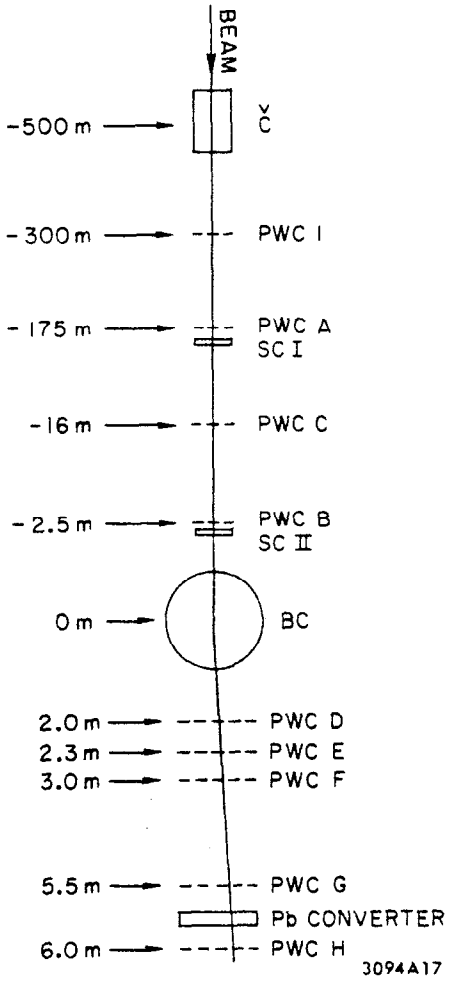
BEAM
-500 m
VC
-300 m
PWC I
-175 m
PWC A
SC I
-16 m
PWC C
-2.5 m
PWC B
SC II
0 m
BC
2.0 m
PWC D
2.3 m
PWC E
3.0 m
PWC F
5.5 m
PWC G
Pb CONVERTER
6.0 m
PWC H
3094A17

Fig. 20

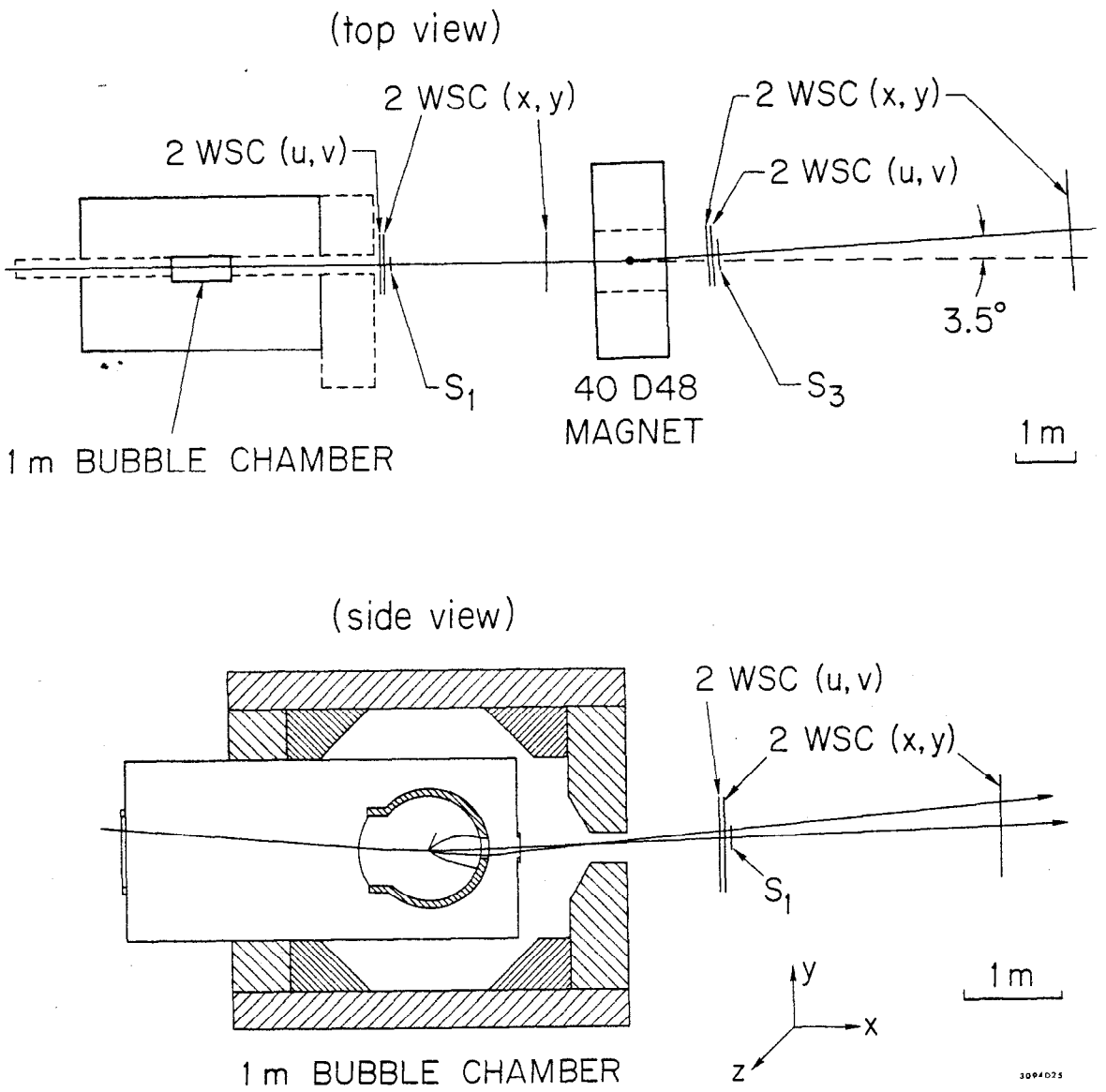
(top view)
2 WSC (x, y)
2 WSC (x, y)
2 WSC (u, v)
2 WSC (u, v)
3.5°
S1
S3
40 D48
MAGNET
1 m
1 m BUBBLE CHAMBER
(side view)
2 WSC (u, v)
2 WSC (x, y)
S1
y
x
z
1 m
1 m BUBBLE CHAMBER

Fig. 21

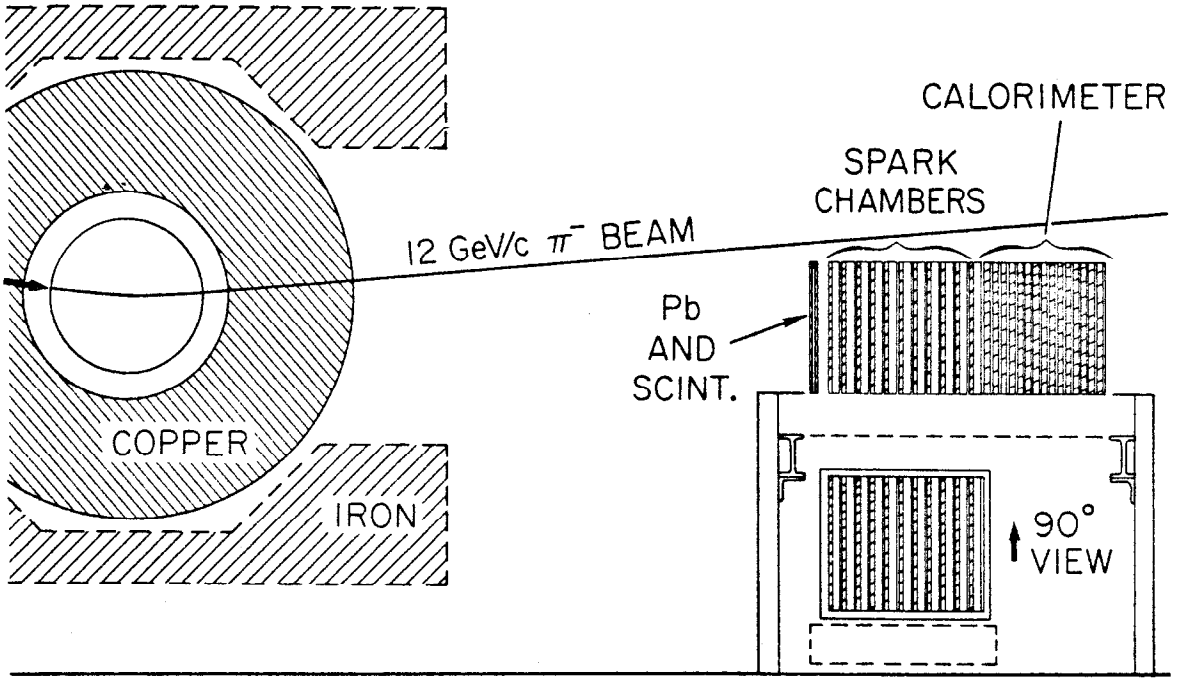

UCLA NEUTRON DOWNSTREAM TRIGGER 3094A4

Fig. 22

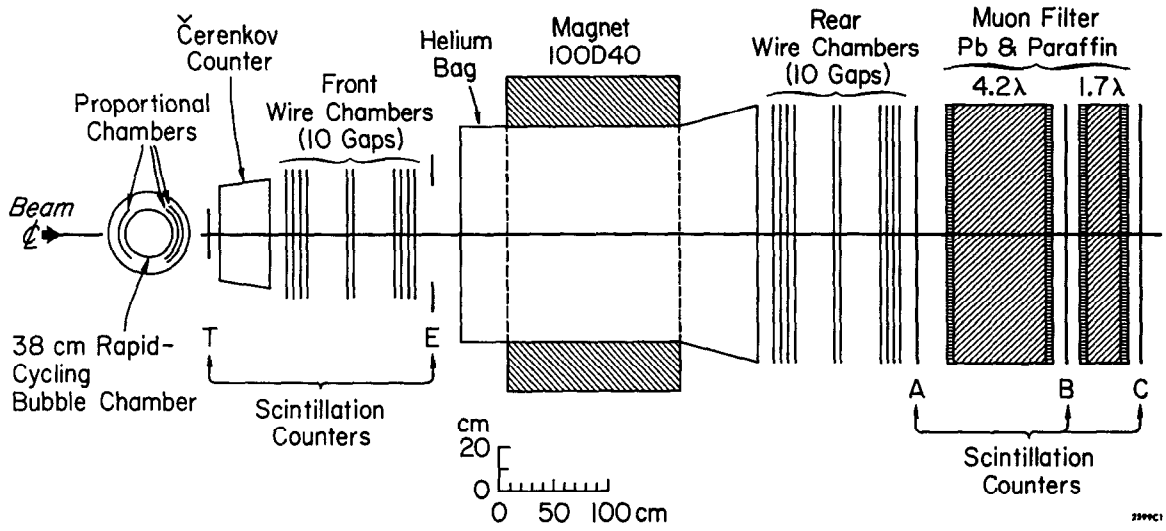

K° DOWNSTREAM TRIGGER

Fig. 23

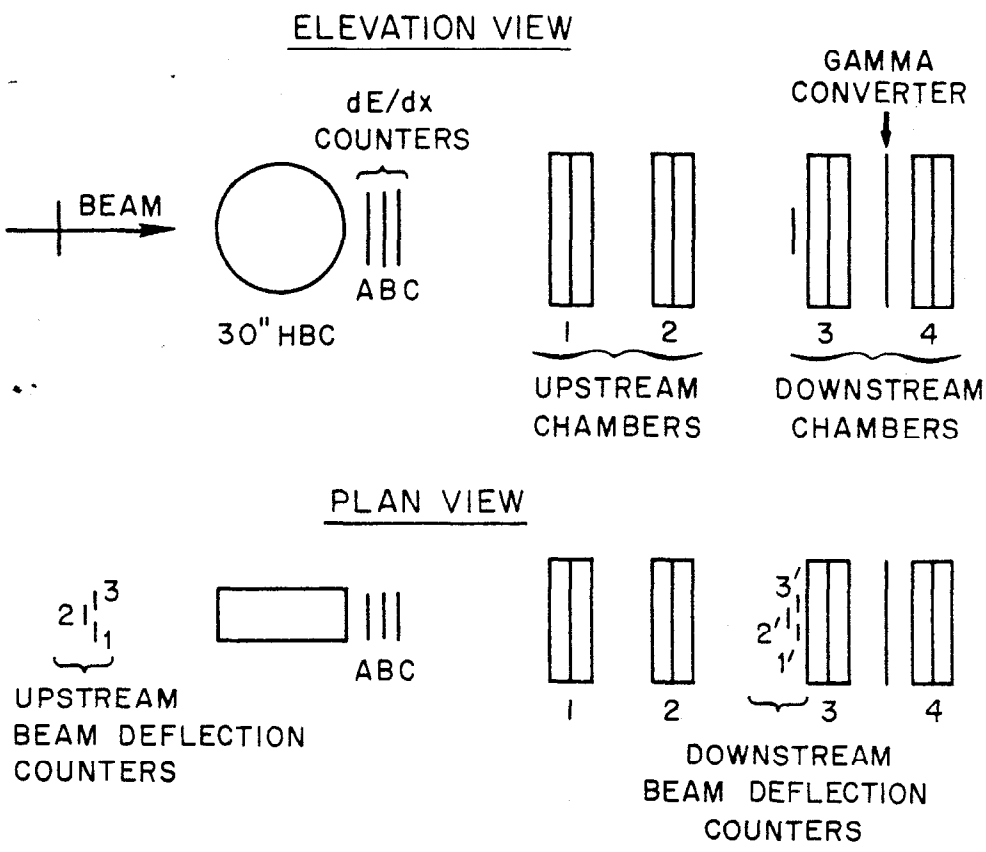

TRIGGER: $(1+2+3)\cdot A(2)\cdot B(2)\cdot C(2)$

$$\text{OR}\left\{\begin{matrix}1\\2\\3\end{matrix}\right\}\cdot A(1)\cdot B(1)\cdot C(1)\left\{\begin{matrix}\overline{1'}\\\overline{2'}\\\overline{3'}\end{matrix}\right\}$$

DOWNSTREAM OPTICAL SPARK CHAMBERS TRIGGER

3094A3

Fig. 24

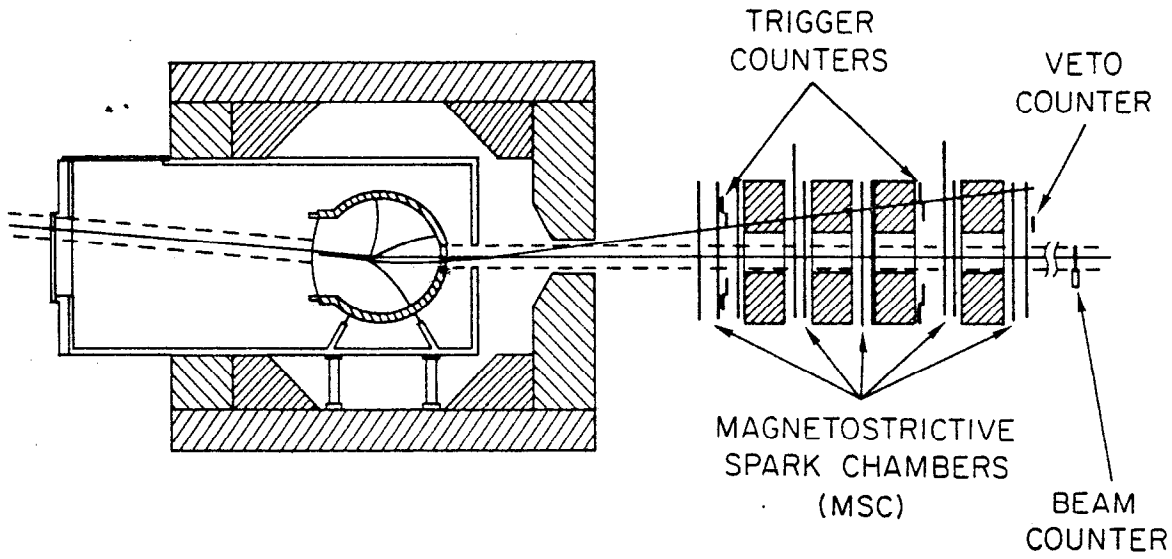

SLAC Im H.S. MUON DOWNSTREAM TRIGGER 3094A5

Fig. 25

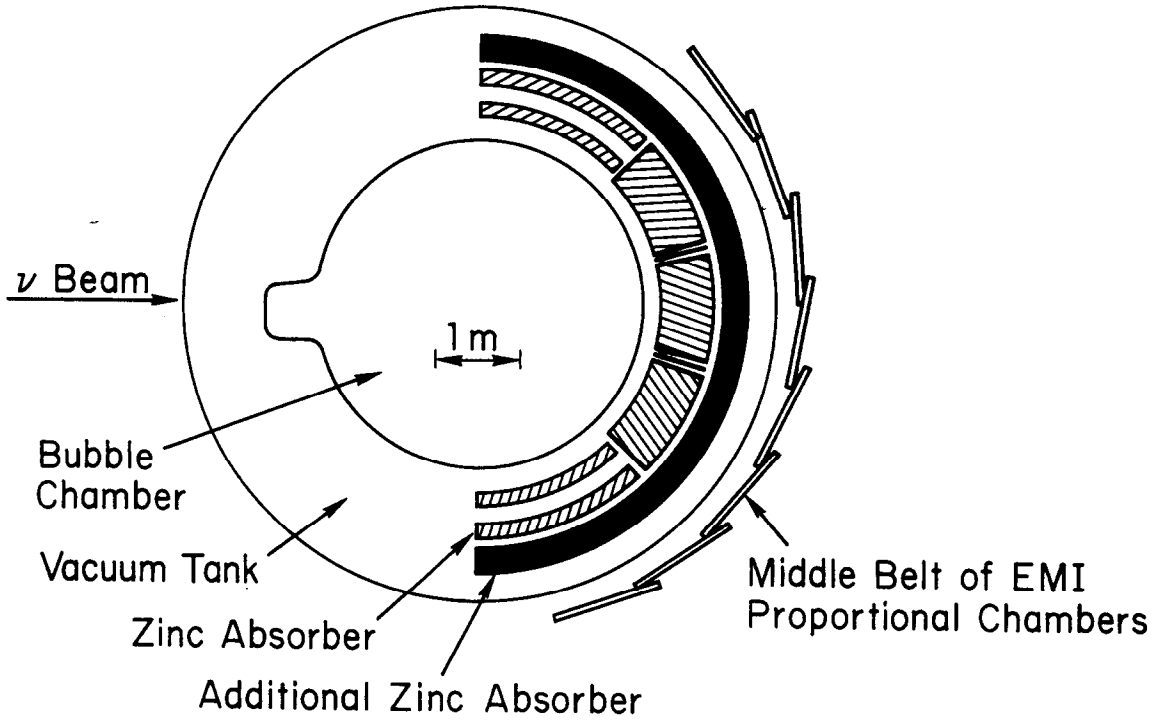
ν Beam
1 m
Bubble Chamber
Vacuum Tank
Zinc Absorber
Additional Zinc Absorber
Middle Belt of EMI Proportional Chambers

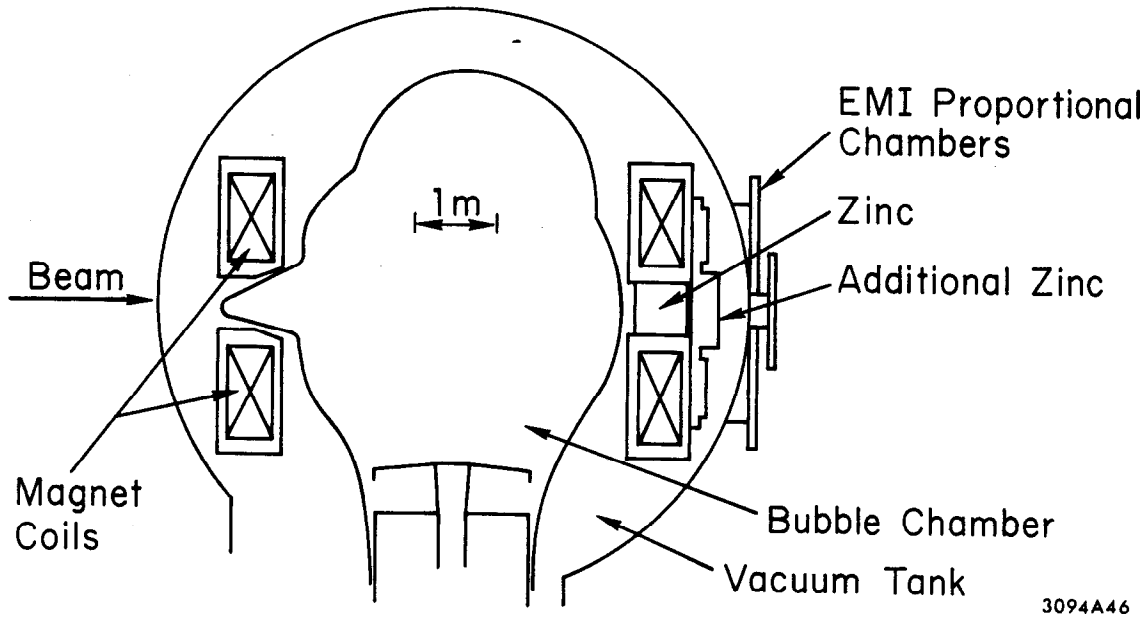
EMI Proportional Chambers
Zinc
Additional Zinc
1 m
Beam
Magnet Coils
Bubble Chamber
Vacuum Tank
3094A46

Fig. 26

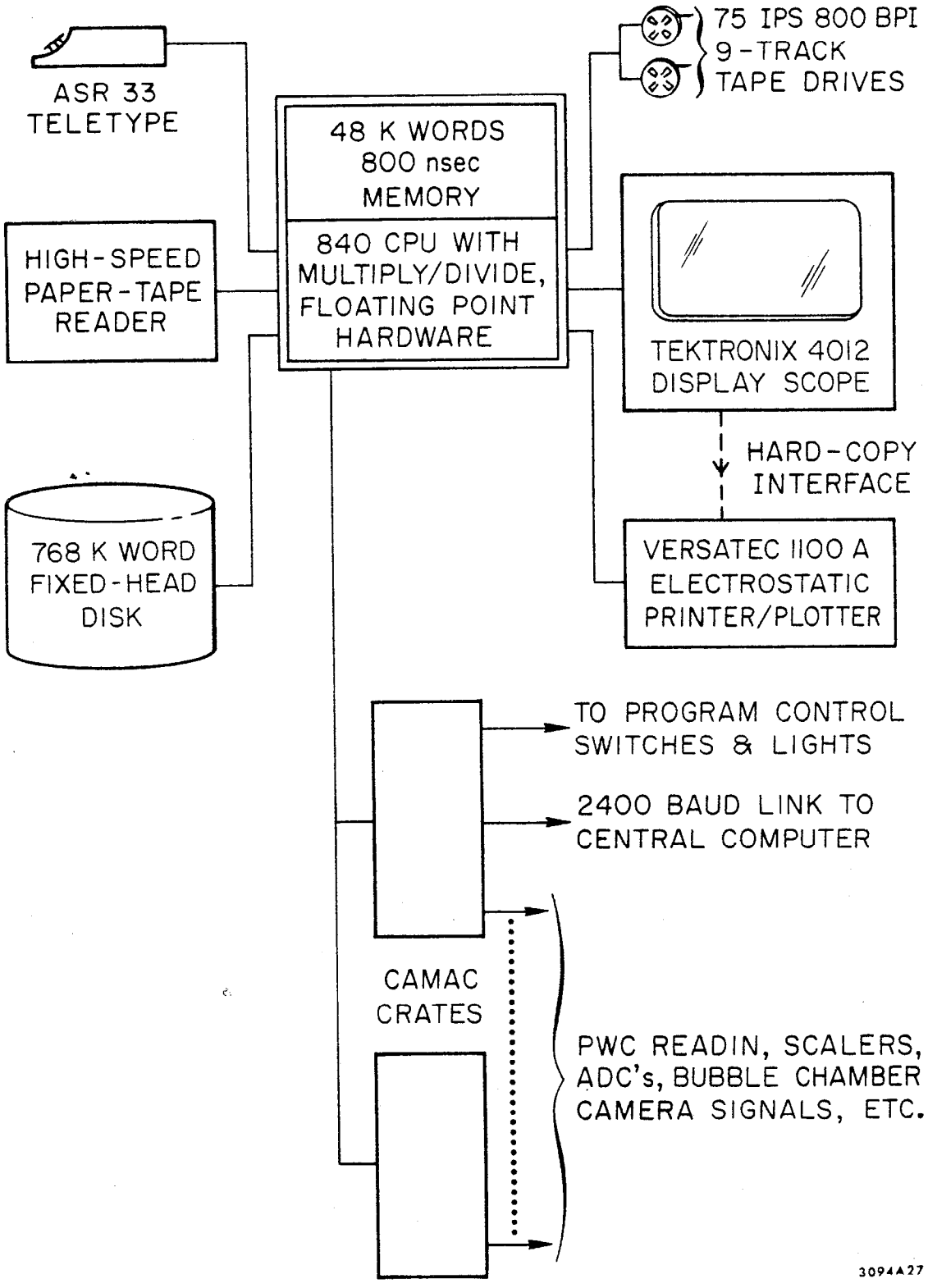
ASR 33
TELETYPE
48 K WORDS
800 nsec
MEMORY
840 CPU WITH
MULTIPLY/DIVIDE,
FLOATING POINT
HARDWARE
75 IPS 800 BPI
9-TRACK
TAPE DRIVES
HIGH-SPEED
PAPER-TAPE
READER
TEKTRONIX 4012
DISPLAY SCOPE
HARD-COPY
INTERFACE
768 K WORD
FIXED-HEAD
DISK
VERSATEC 1100 A
ELECTROSTATIC
PRINTER/PLOTTER
TO PROGRAM CONTROL
SWITCHES & LIGHTS
2400 BAUD LINK TO
CENTRAL COMPUTER
CAMAC
CRATES
PWC READIN, SCALERS,
ADC's, BUBBLE CHAMBER
CAMERA SIGNALS, ETC.
3094A27

Fig. 27

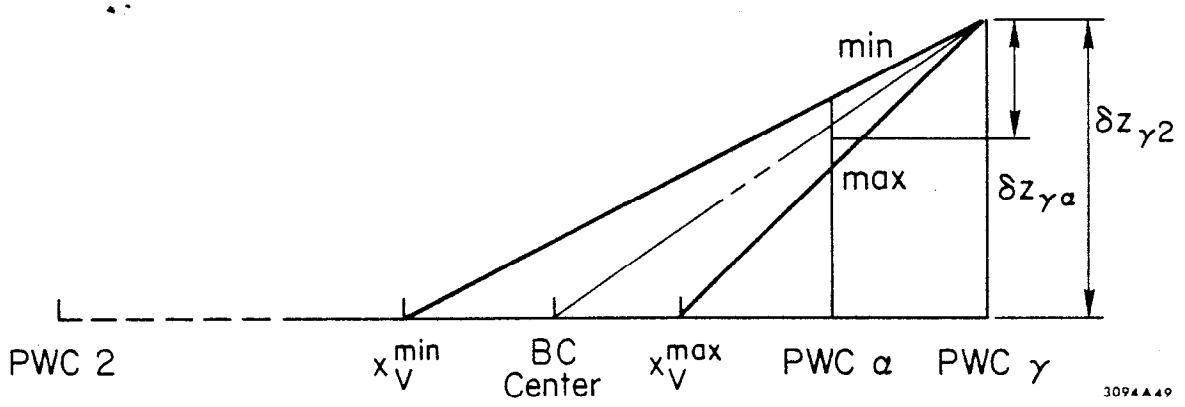
min
max
$\delta z_{\gamma 2}$
$\delta z_{\gamma \alpha}$
PWC 2
x_V^{min}
BC
Center
x_V^{max}
PWC α
PWC γ
3094A49

Fig. 28

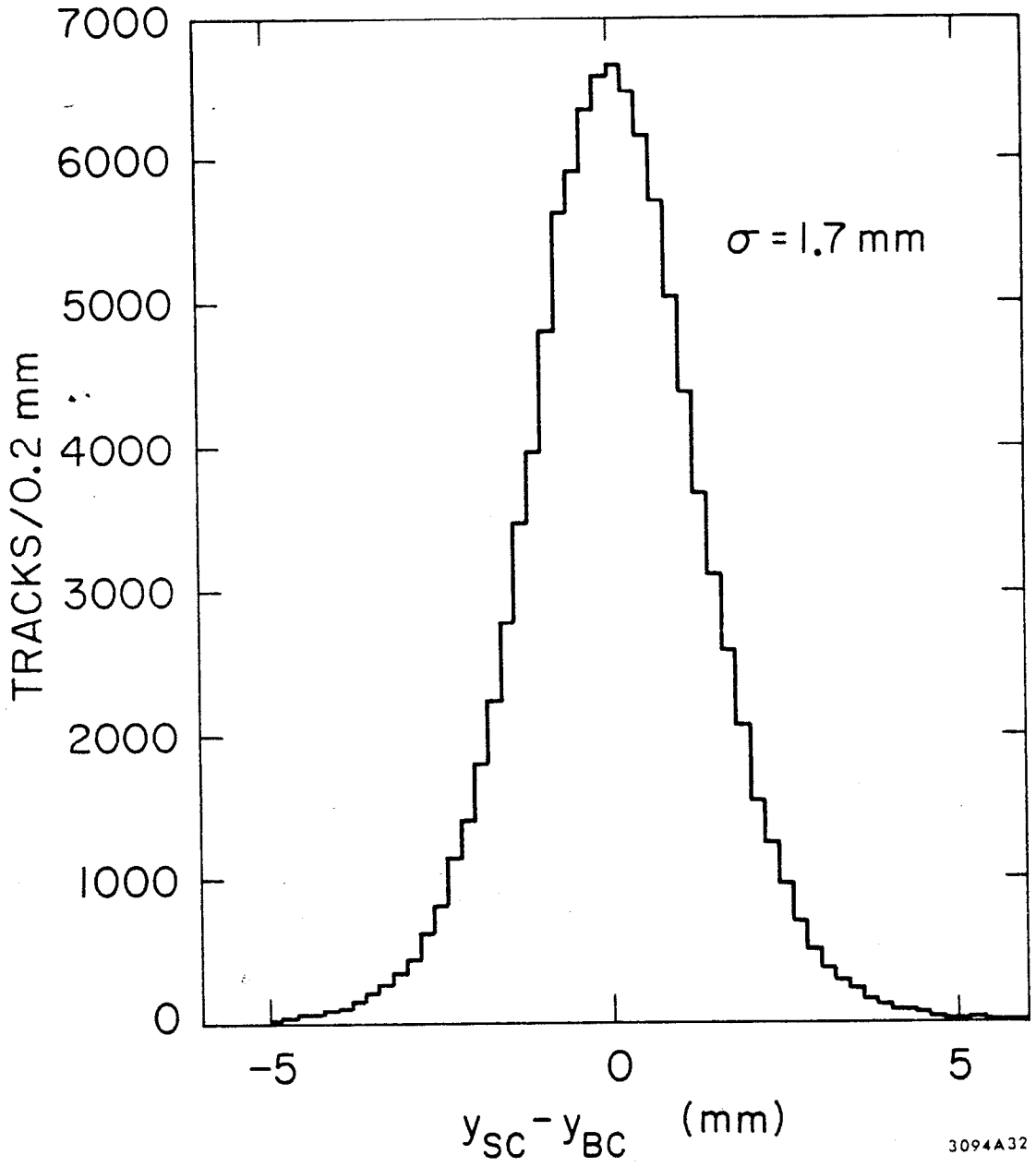
7000
6000
5000
4000
3000
2000
1000
0
TRACKS/0.2 mm
σ = 1.7 mm
-5
0
5
$y_{SC} - y_{BC}$ (mm)
3094A32

Fig 29

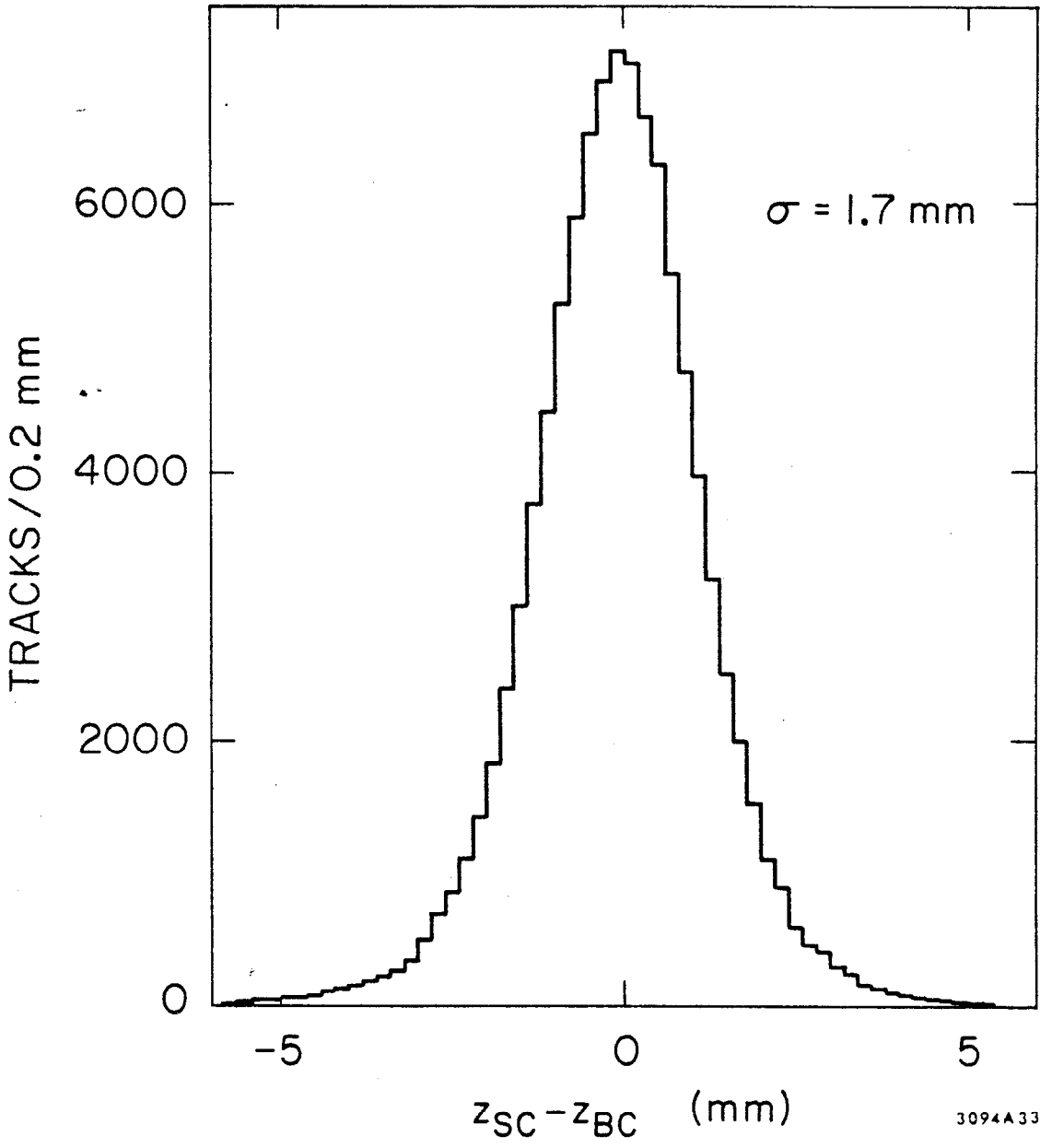

Fig 30

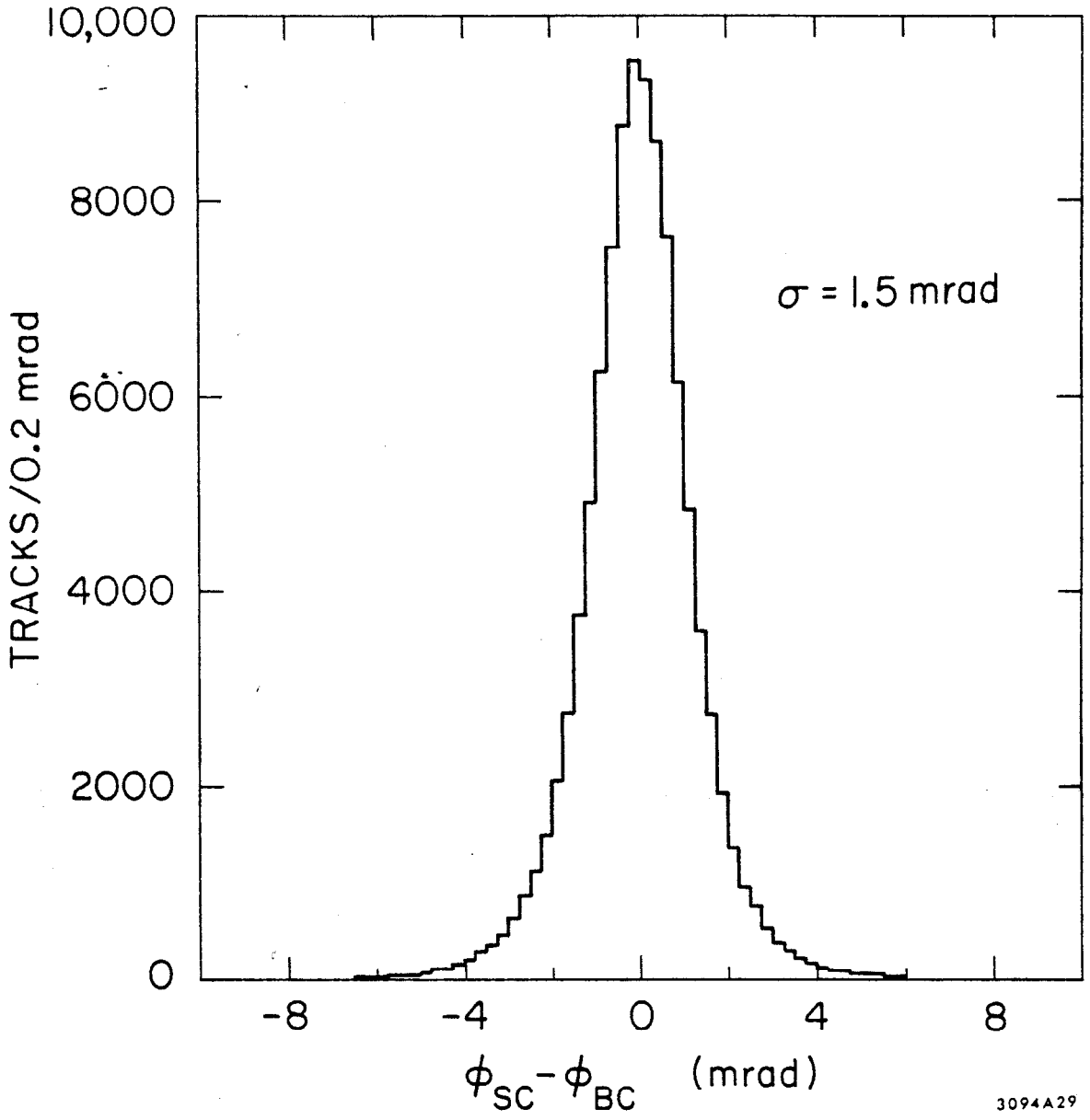
10,000
8000
6000
4000
2000
0
TRACKS/0.2 mrad
σ = 1.5 mrad
-8
-4
0
4
8
$\phi_{SC} - \phi_{BC}$ (mrad)
3094A29

Fig. 31

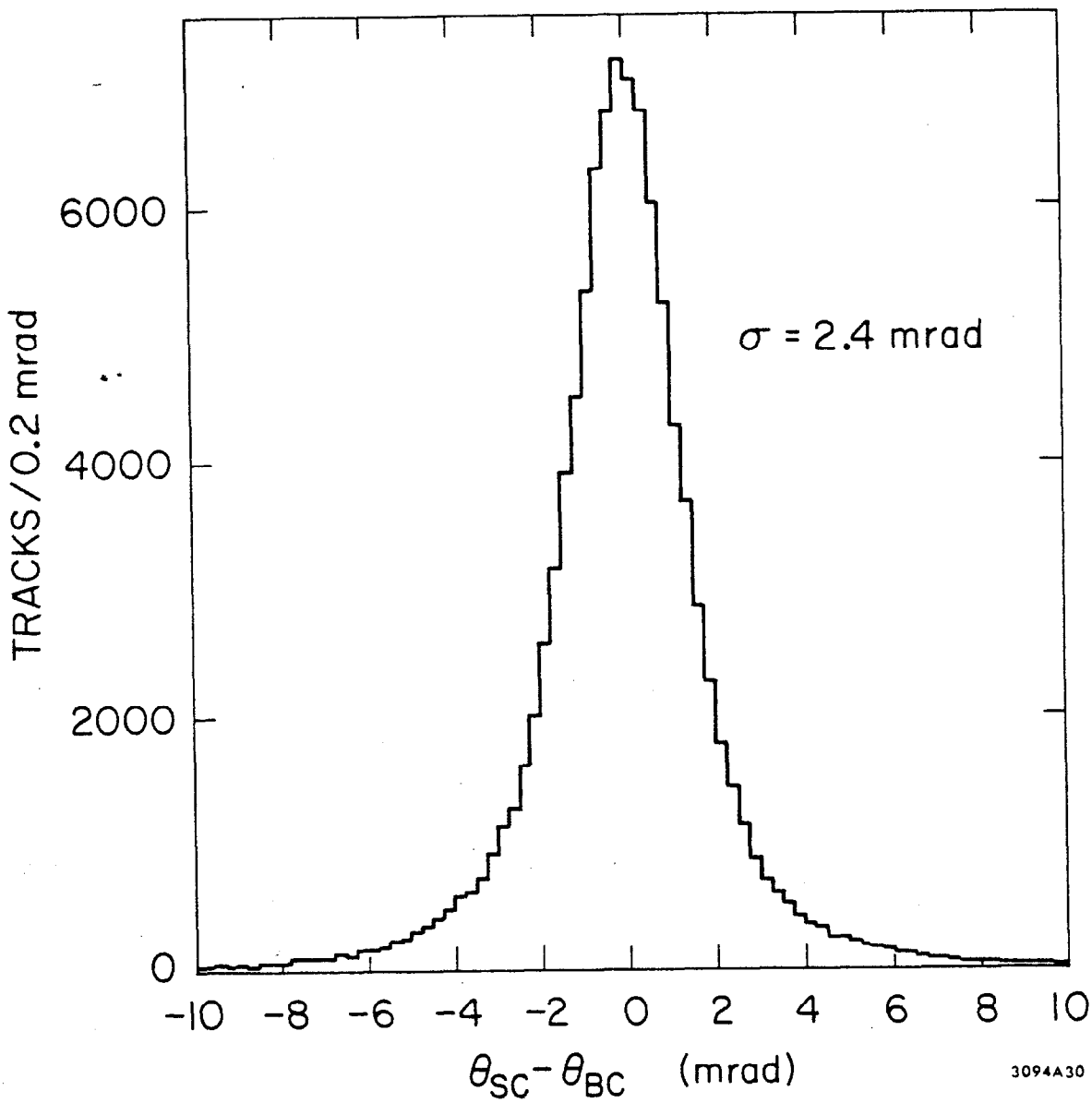
6000
4000
2000
0
TRACKS/0.2 mrad
σ = 2.4 mrad
-10 -8 -6 -4 -2 0 2 4 6 8 10
θSC - θBC (mrad)
3094A30

Fig. 32

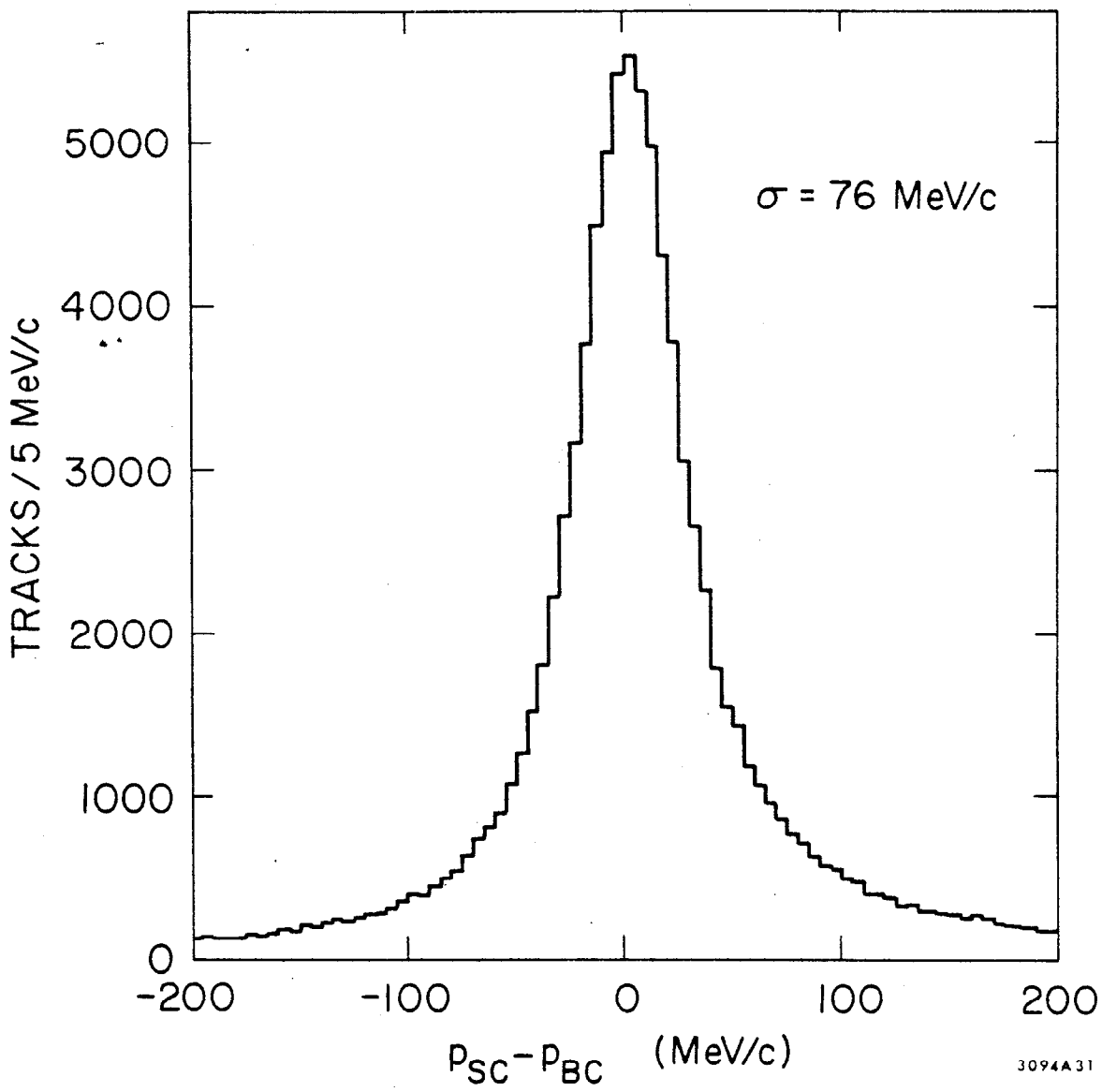
5000
4000
3000
2000
1000
0
TRACKS / 5 MeV/c
σ = 76 MeV/c
-200
-100
0
100
200
$p_{SC} - p_{BC}$ (MeV/c)
3094A31

Fig. 33

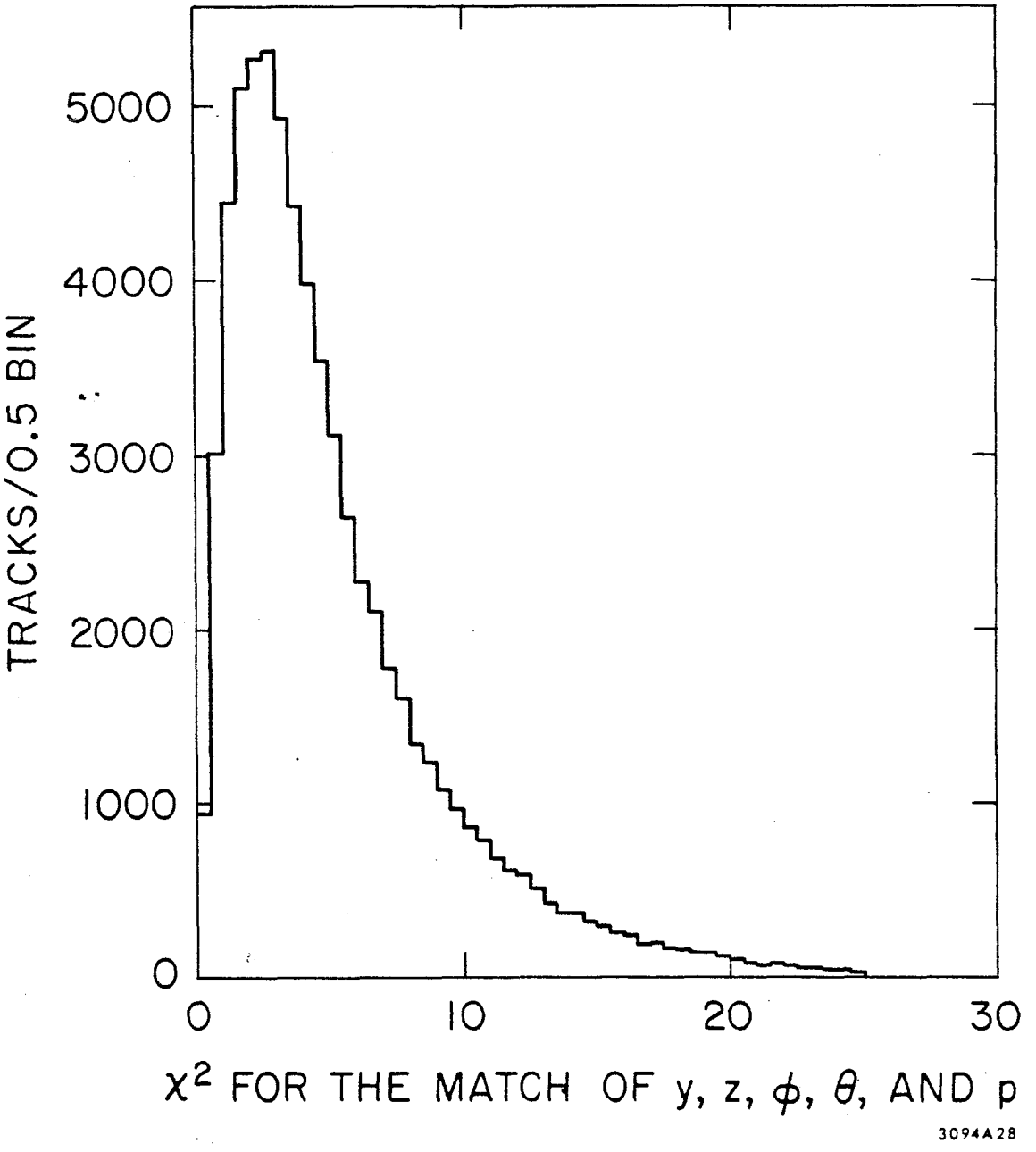
5000
4000
3000
2000
1000
0
TRACKS/0.5 BIN
0
10
20
30
χ^2 FOR THE MATCH OF y, z, ϕ, θ, AND p
3094A28

Fig. 34

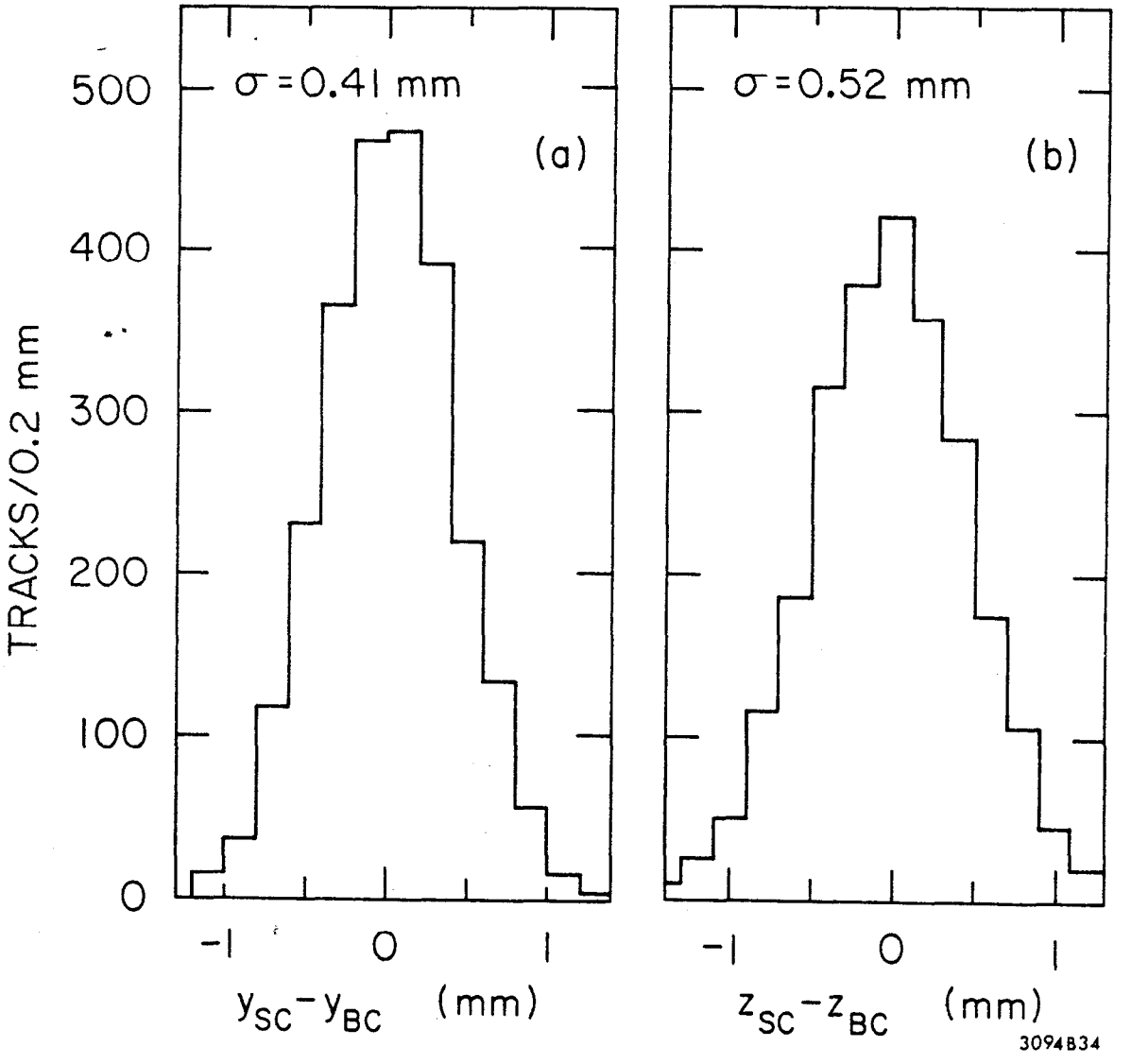
σ = 0.41 mm
(a)
σ = 0.52 mm
(b)
TRACKS/0.2 mm
500
400
300
200
100
0
-1
0
1
$y_{SC} - y_{BC}$ (mm)
$z_{SC} - z_{BC}$ (mm)
3094B34

Fig. 35

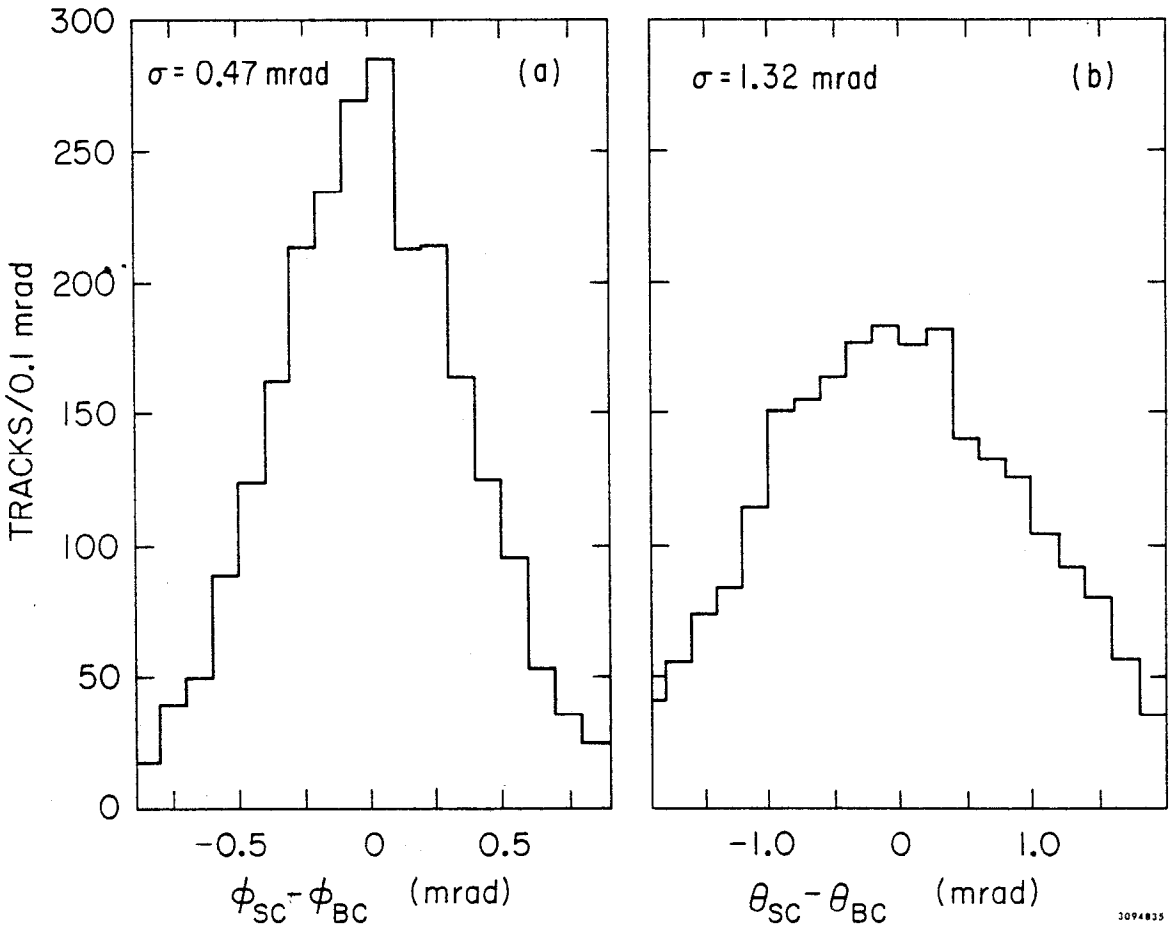
300
250
200
150
100
50
0
TRACKS/0.1 mrad
σ = 0.47 mrad
(a)
σ = 1.32 mrad
(b)
-0.5
0
0.5
-1.0
0
1.0
$\phi_{SC}-\phi_{BC}$ (mrad)
$\theta_{SC}-\theta_{BC}$ (mrad)
3094835

Fig. 36

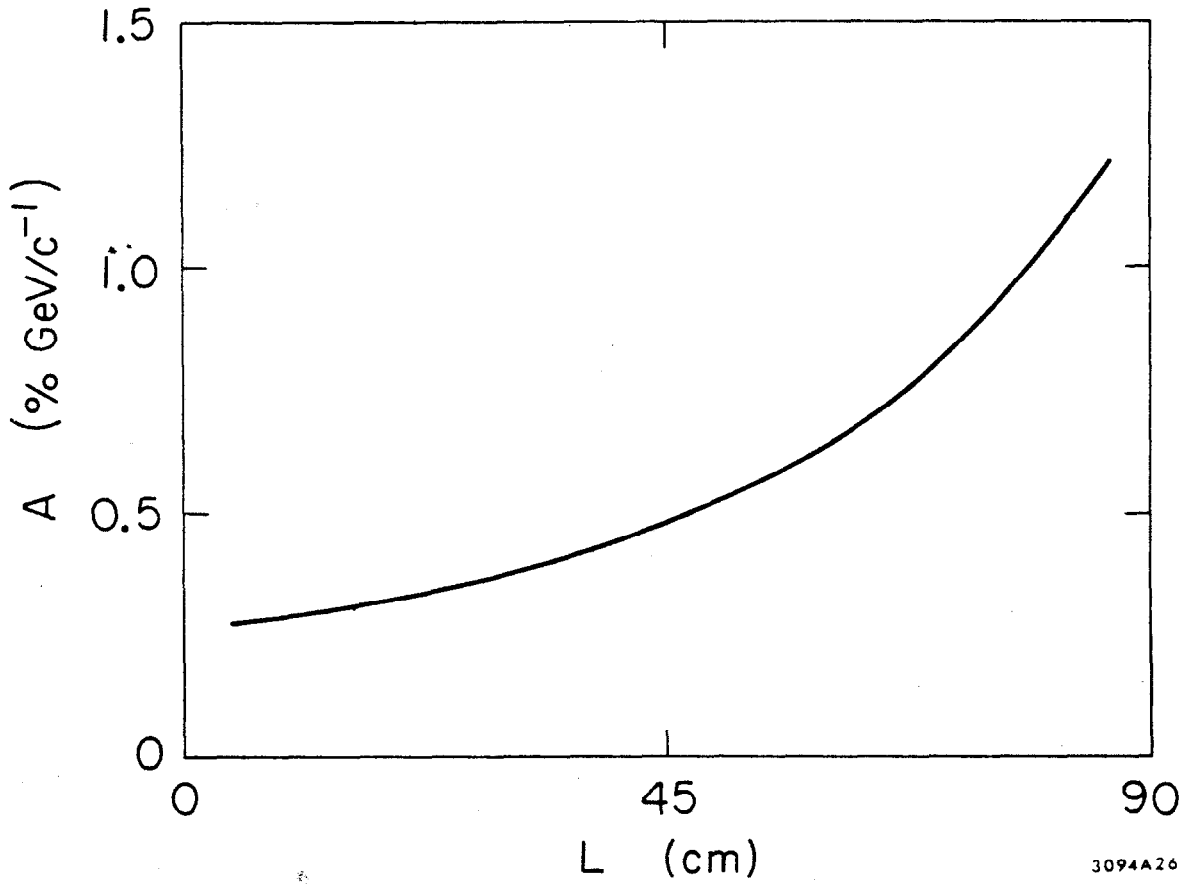

Fig. 37

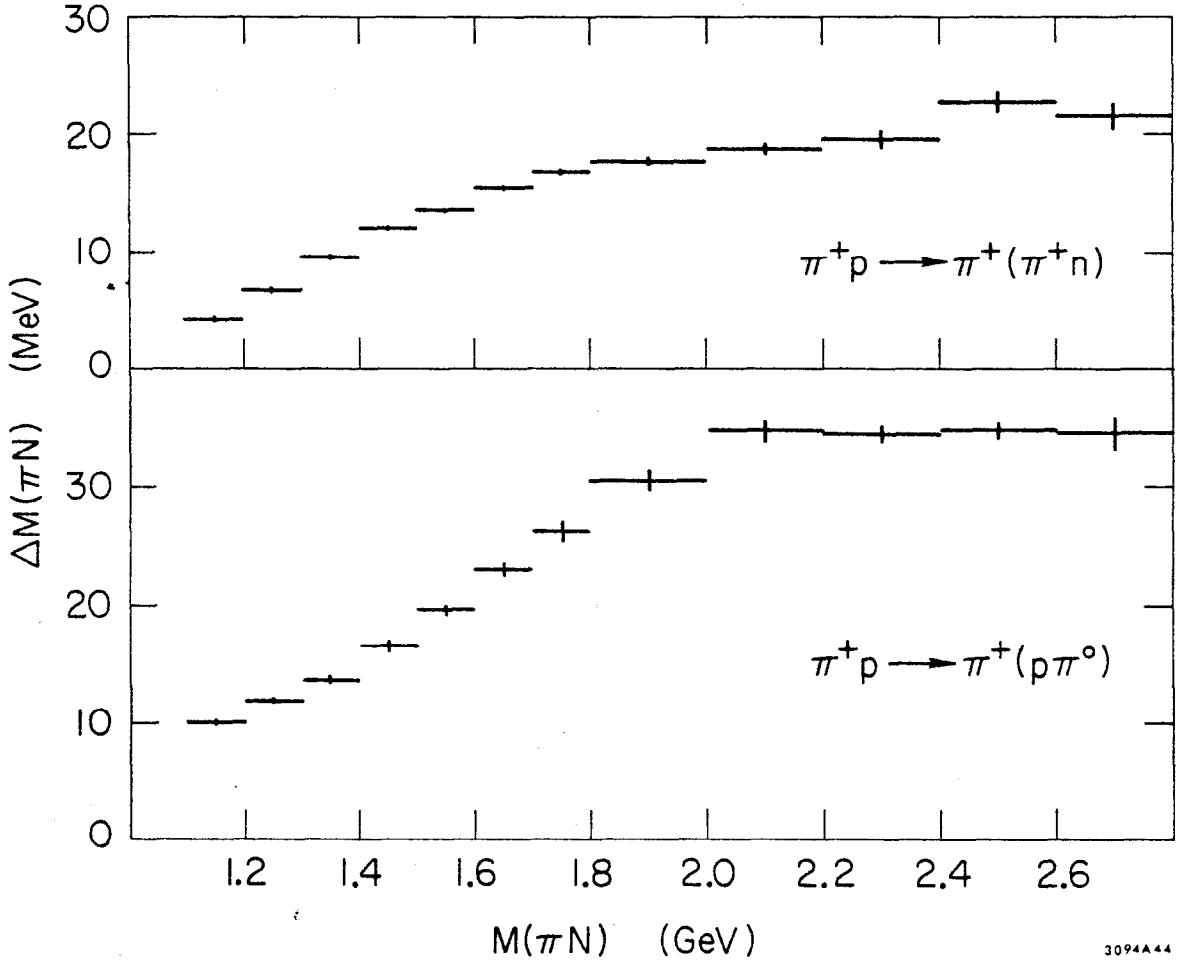
30
20
10
0
30
20
10
0
ΔM(πN) (MeV)
π⁺p → π⁺(π⁺n)
π⁺p → π⁺(pπ°)
1.2
1.4
1.6
1.8
2.0
2.2
2.4
2.6
M(πN) (GeV)
3094A44

Fig. 38

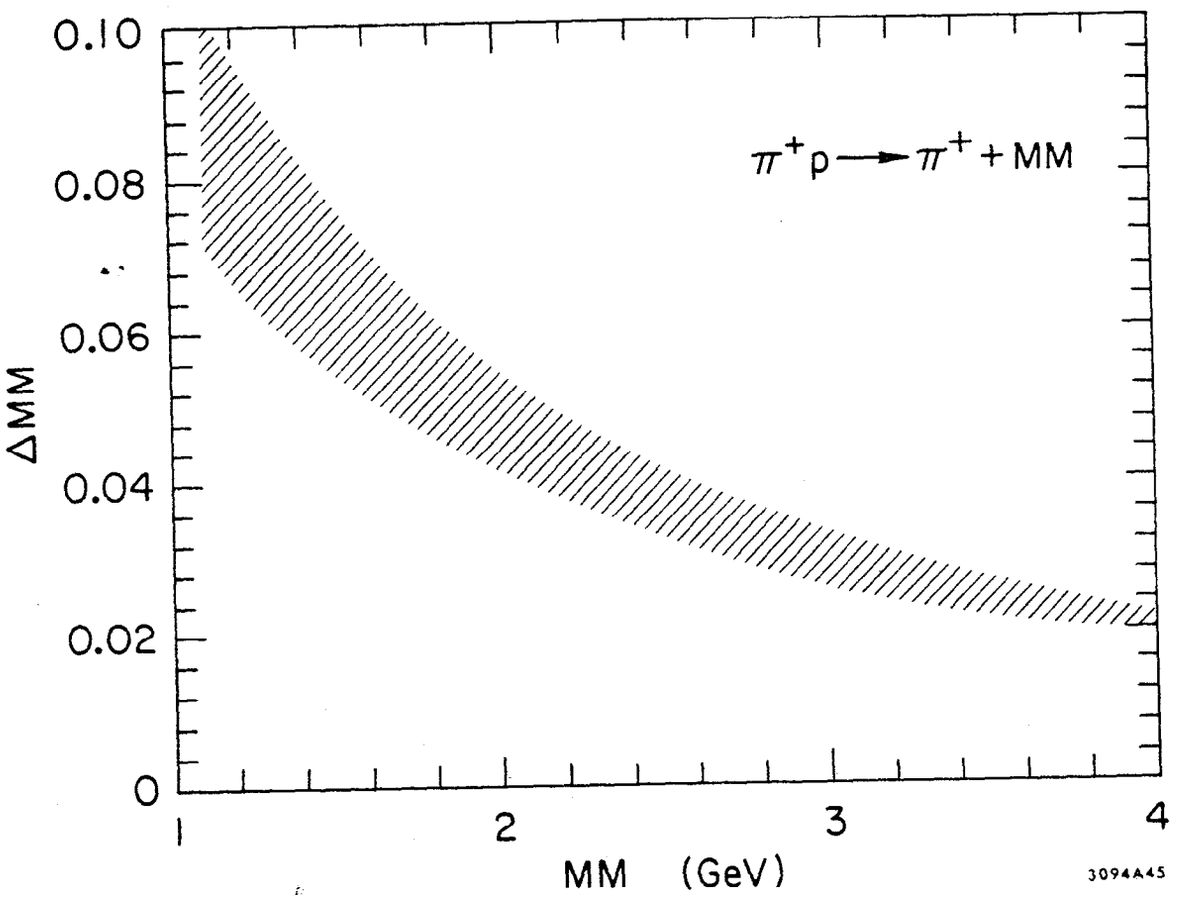
0.10
0.08
0.06
0.04
0.02
0
ΔMM
$\pi^+ p \longrightarrow \pi^+ + MM$
1
2
3
4
MM (GeV)
3094A45

Fig. 39

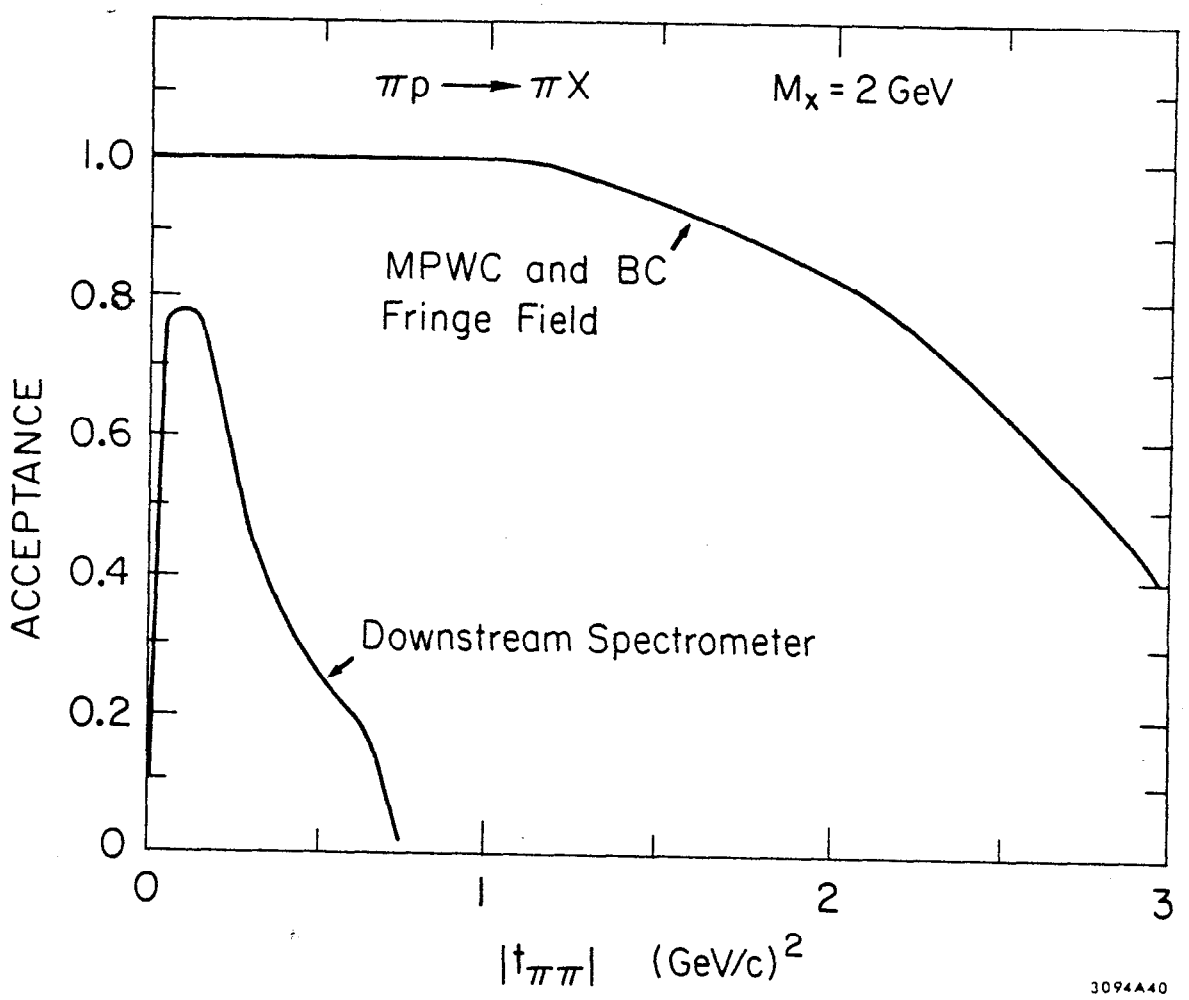
πp → πX
M_x = 2 GeV
MPWC and BC
Fringe Field
Downstream Spectrometer
ACCEPTANCE
1.0
0.8
0.6
0.4
0.2
0
0
1
2
3
$|t_{\pi\pi}|$ (GeV/c)^2
3094A40

Fig. 40

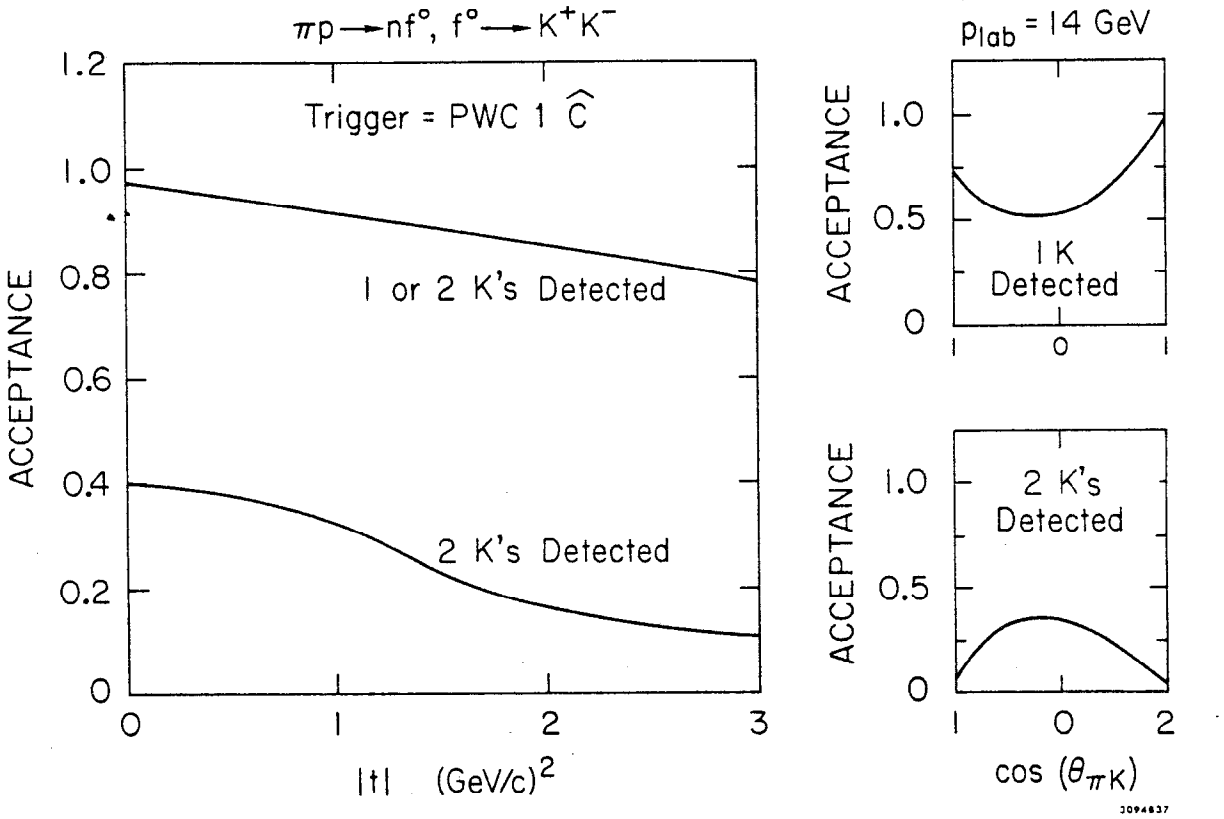
πp → nf°, f° → K⁺K⁻
Trigger = PWC 1 Ĉ
1 or 2 K's Detected
2 K's Detected
ACCEPTANCE
|t| (GeV/c)²
p_lab = 14 GeV
1 K Detected
2 K's Detected
cos (θ_πK)
3094837

Fig. 41

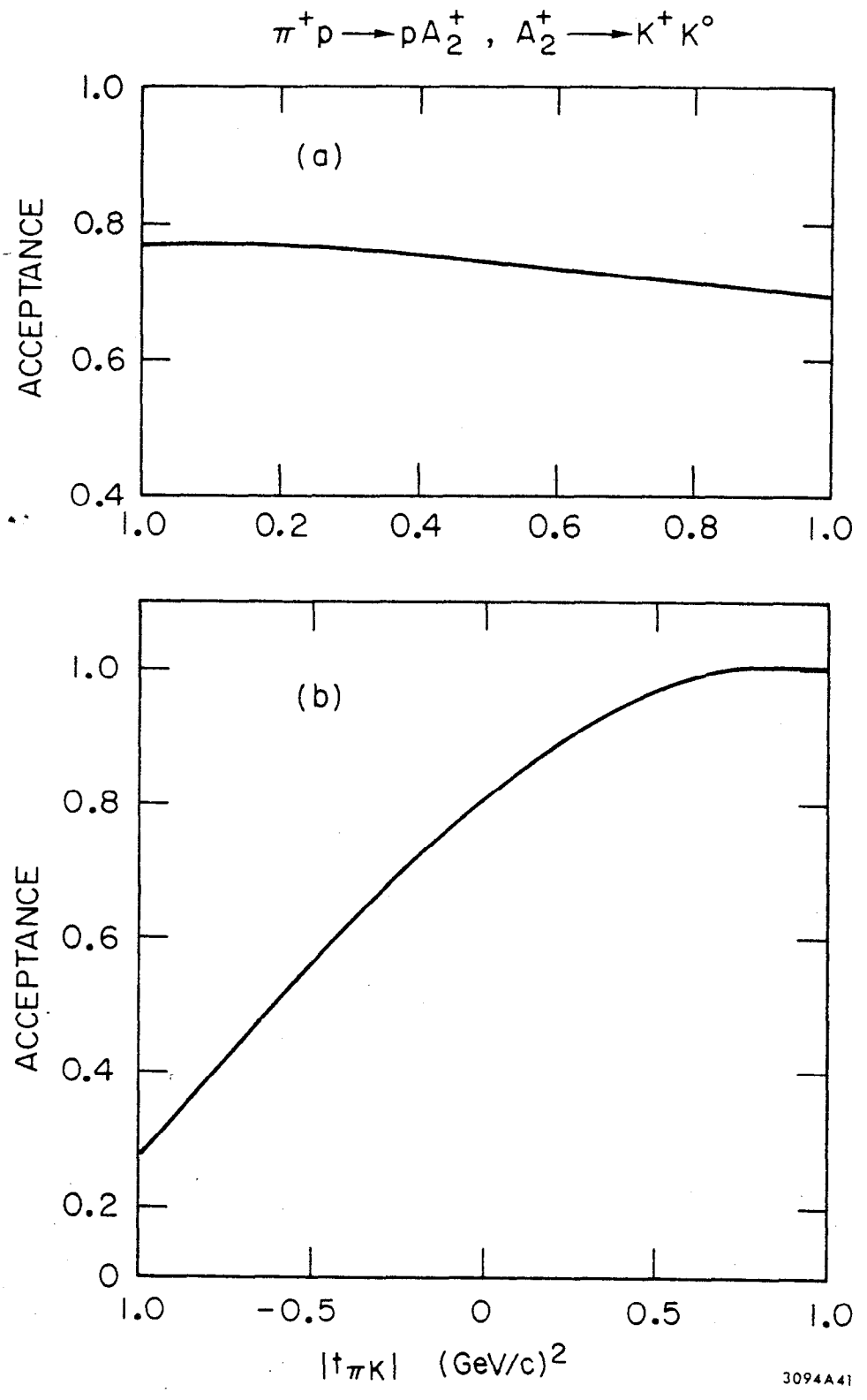
$\pi^+ p \rightarrow p A_2^+$, $A_2^+ \rightarrow K^+ K^\circ$
(a)
ACCEPTANCE
1.0
0.8
0.6
0.4
1.0
0.2
0.4
0.6
0.8
1.0
(b)
ACCEPTANCE
1.0
0.8
0.6
0.4
0.2
0
1.0
-0.5
0
0.5
1.0
$|t_{\pi K}|$ $(GeV/c)^2$
3094A41

Fig. 42

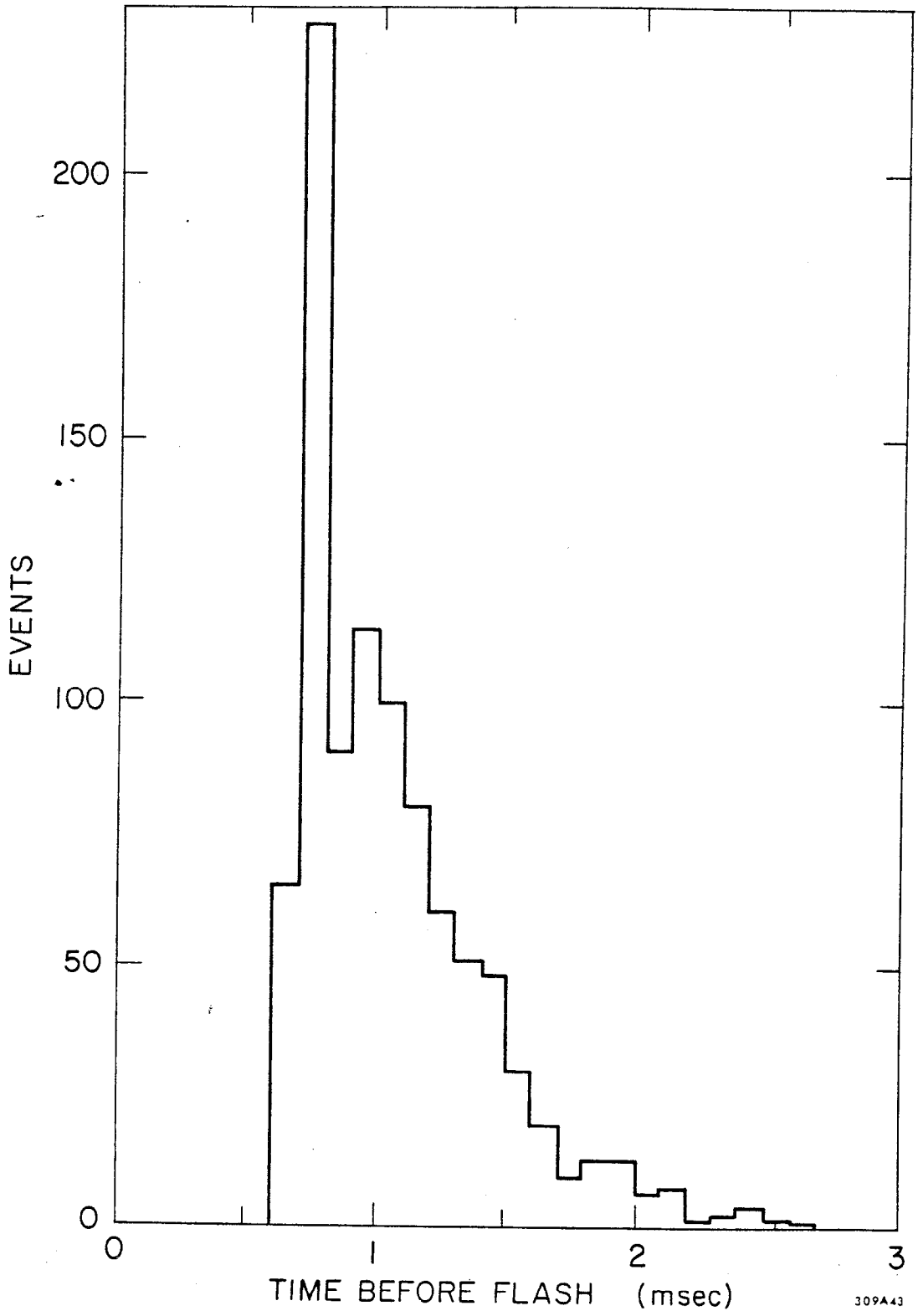

Fig. 43

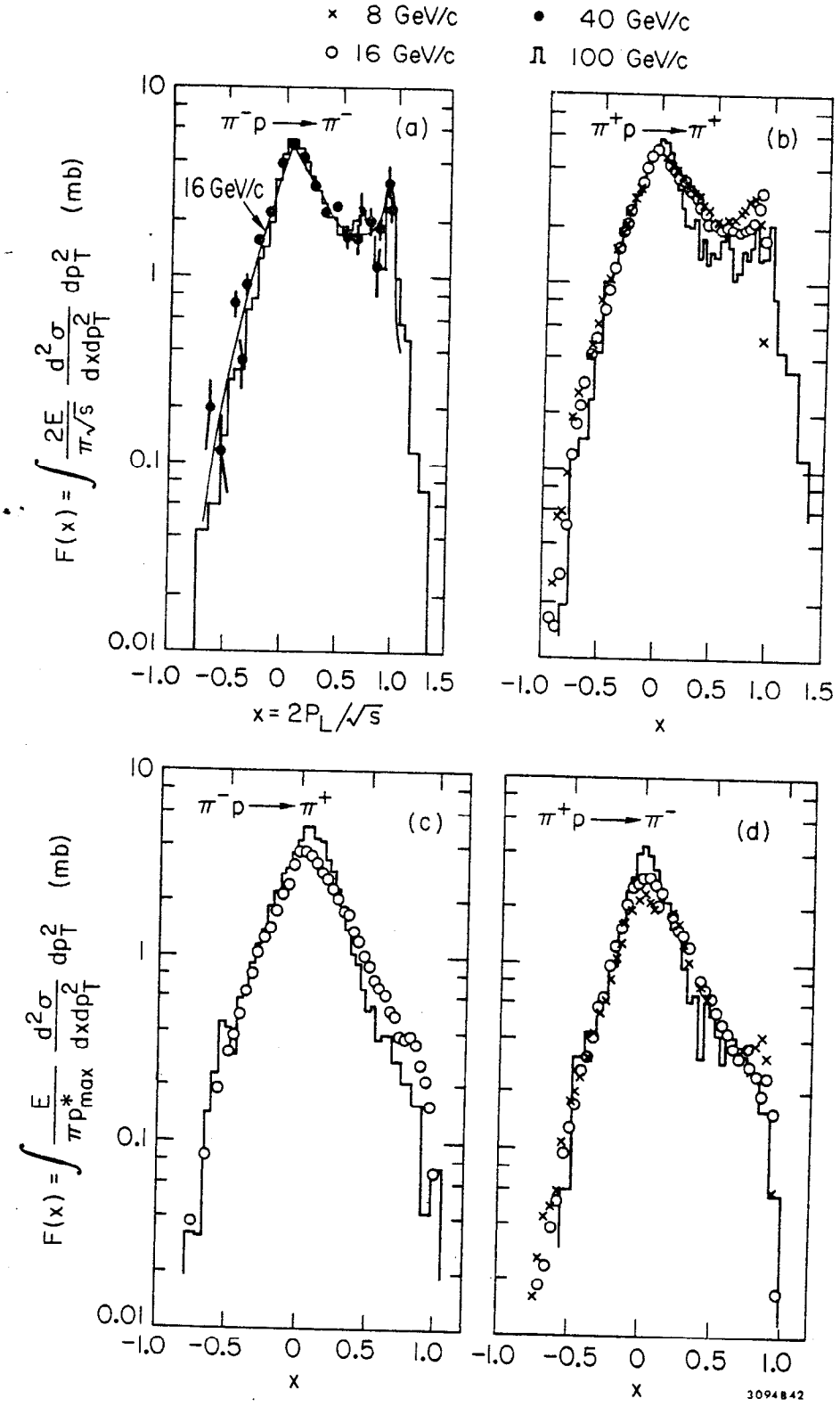
× 8 GeV/c
○ 16 GeV/c
• 40 GeV/c
Л 100 GeV/c
$\pi^- p \to \pi^-$ (a)
16 GeV/c
$\pi^+ p \to \pi^+$ (b)
$\pi^- p \to \pi^+$ (c)
$\pi^+ p \to \pi^-$ (d)
$F(x) = \int \frac{2E}{\pi\sqrt{s}} \frac{d^2\sigma}{dx dp_T^2} dp_T^2$ (mb)
$F(x) = \int \frac{E}{\pi p^*_{max}} \frac{d^2\sigma}{dx dp_T^2} dp_T^2$ (mb)
$x = 2P_L/\sqrt{s}$
x
10
1
0.1
0.01
-1.0 -0.5 0 0.5 1.0 1.5
3094842

Fig. 44

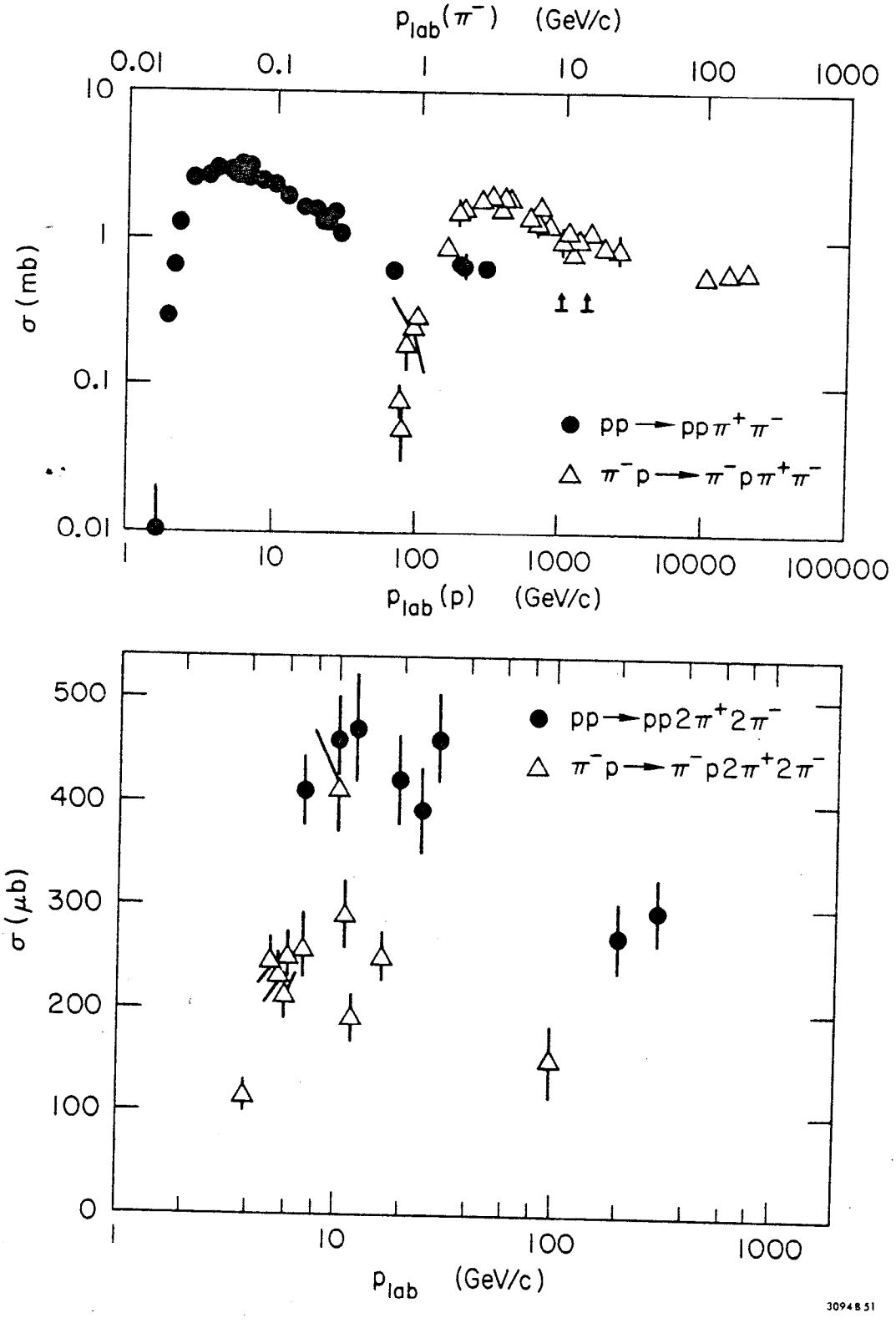
$p_{lab}(\pi^-)$ (GeV/c)
0.01
0.1
1
10
100
1000
σ (mb)
10
1
0.1
0.01
$pp \rightarrow pp\pi^+\pi^-$
$\pi^- p \rightarrow \pi^- p\pi^+\pi^-$
1
10
100
1000
10000
100000
$p_{lab}(p)$ (GeV/c)
σ (μb)
500
400
300
200
100
0
$pp \rightarrow pp2\pi^+2\pi^-$
$\pi^- p \rightarrow \pi^- p2\pi^+2\pi^-$
1
10
100
1000
p_{lab} (GeV/c)
3094B51

Fig. 45

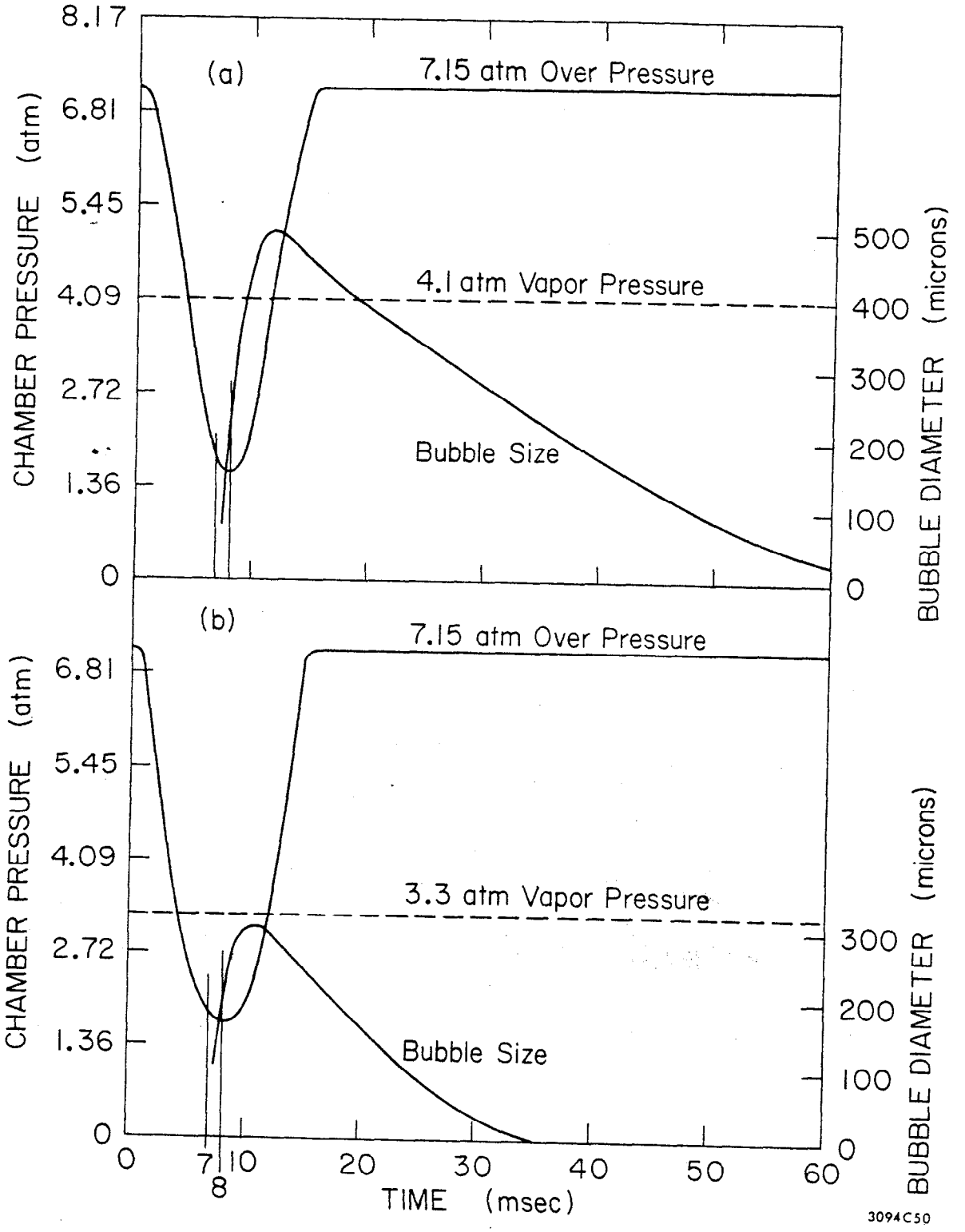
8.17
6.81
5.45
4.09
2.72
1.36
0
(a)
7.15 atm Over Pressure
4.1 atm Vapor Pressure
Bubble Size
CHAMBER PRESSURE (atm)
500
400
300
200
100
0
BUBBLE DIAMETER (microns)
(b)
7.15 atm Over Pressure
3.3 atm Vapor Pressure
Bubble Size
0
7
8
10
20
30
40
50
60
TIME (msec)
3094C50

Fig. 46

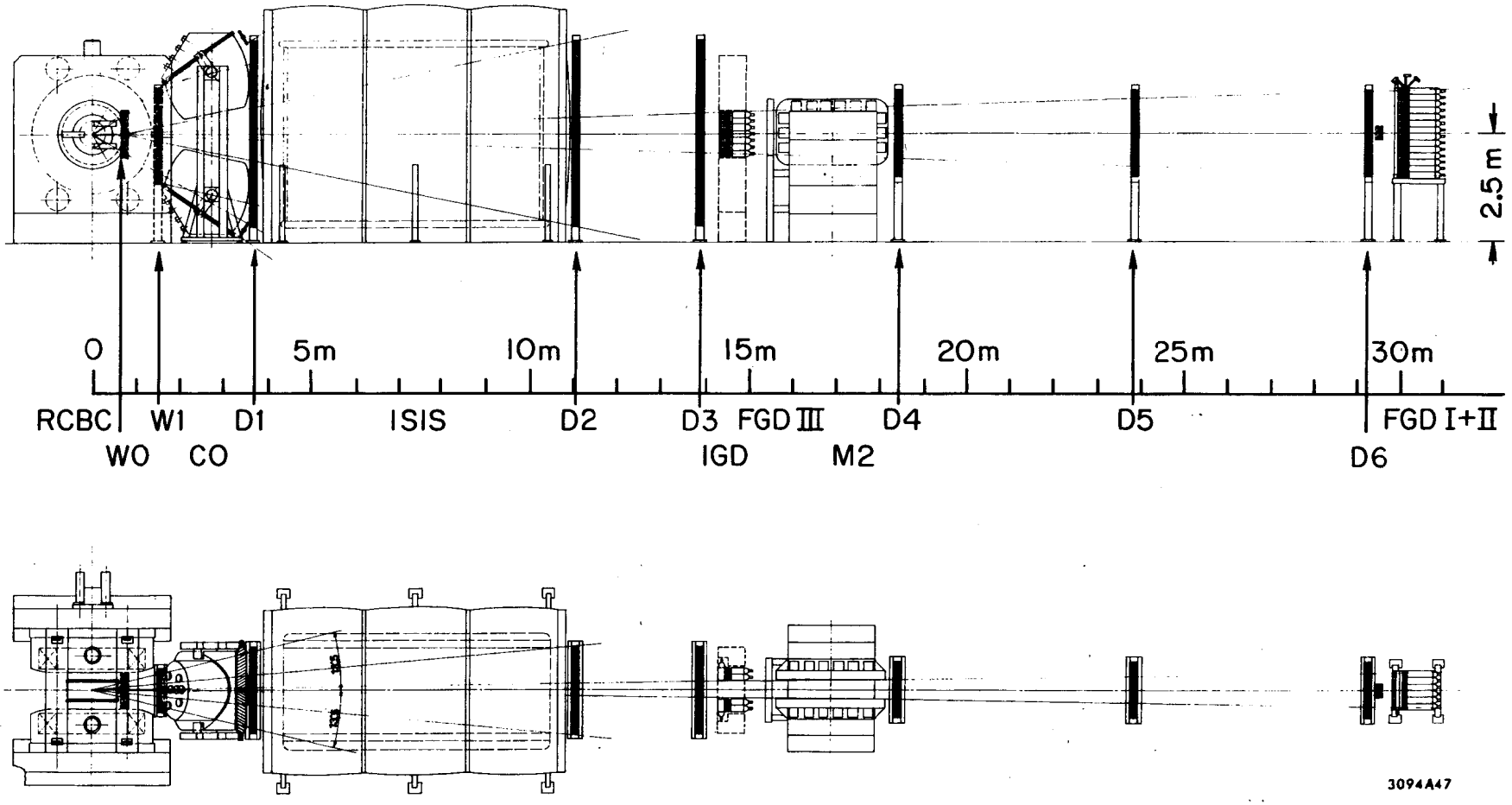
2.5 m
0
5m
10m
15m
20m
25m
30m
RCBC
W1
D1
ISIS
D2
D3
FGD III
D4
D5
FGD I+II
W0
C0
IGD
M2
D6
3094A47

Fig. 47

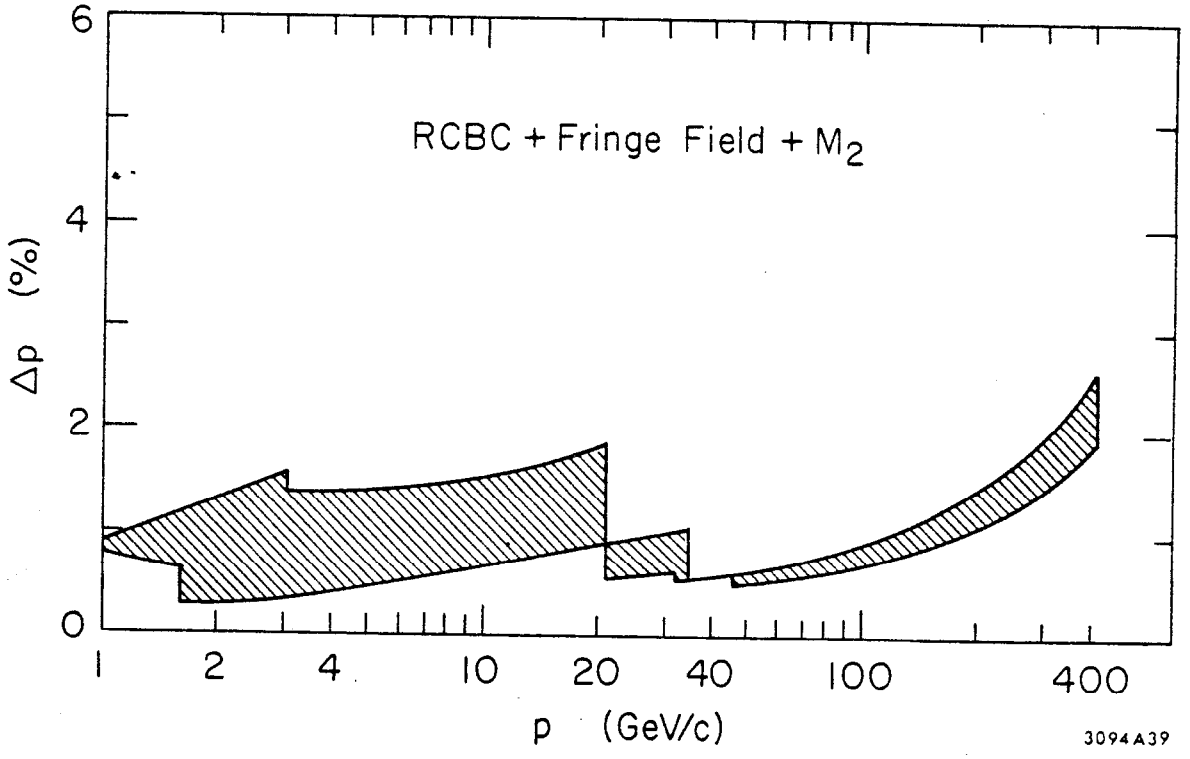
RCBC + Fringe Field + M_2
Δp (%)
6
4
2
0
1
2
4
10
20
40
100
400
p (GeV/c)
3094A39

Fig. 48

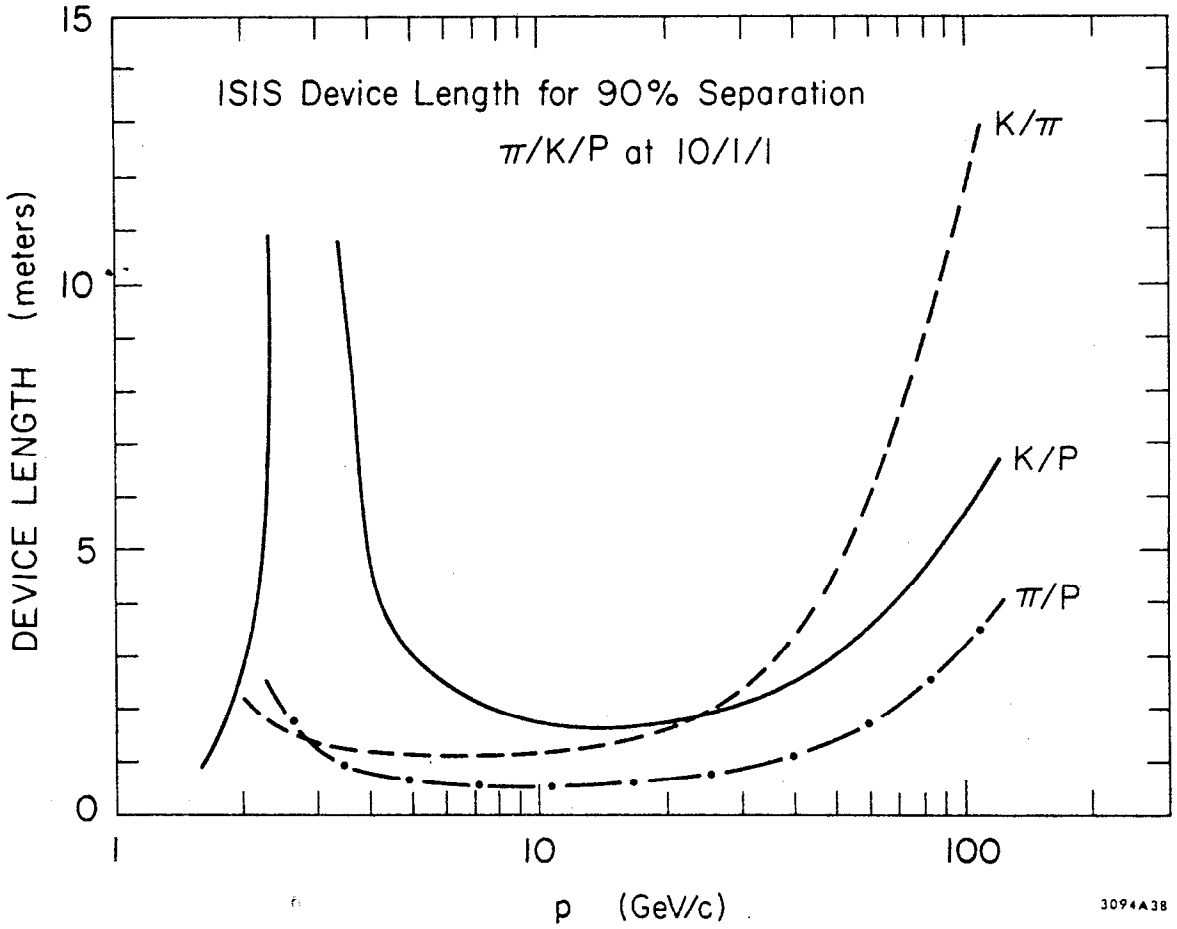
ISIS Device Length for 90% Separation
π/K/P at 10/1/1
K/π
K/P
π/P
DEVICE LENGTH (meters)
15
10
5
0
1
10
100
p (GeV/c)
3094A38

Fig. 49

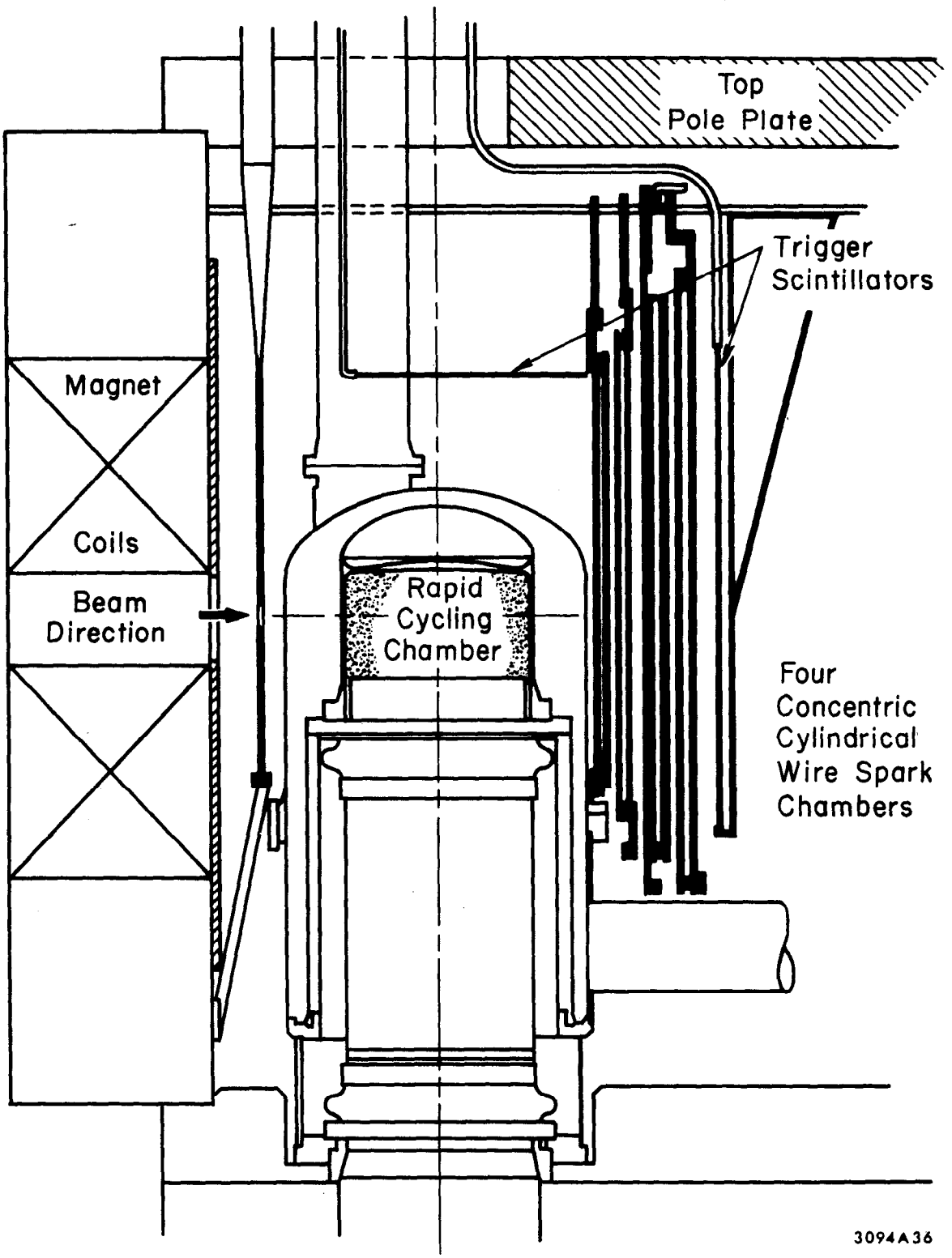
Top
Pole Plate
Trigger
Scintillators
Magnet
Coils
Beam
Direction
Rapid
Cycling
Chamber
Four
Concentric
Cylindrical
Wire Spark
Chambers
3094A36

Fig. 50